Mon. Not. R. Astron. Soc. **345,** 447–479 (2003)

A homogeneous sample of sub-damped Lyman α systems – I. Construction of the sample and chemical abundance measurements

M. Dessauges-Zavadsky,[1,3⋆] C. Péroux,[2,4] T.-S. Kim,[3,4] S. D'Odorico[3] and R. G. McMahon[4]

[1]*Observatoire de Genève, 1290 Sauverny, Switzerland*
[2]*Osservatorio Astronomico di Trieste, Via G. B. Tiepolo 11, 34131 Trieste, Italy*
[3]*European Southern Observatory, Karl-Schwarzchild-Str. 2, 85748 Garching bei München, Germany*
[4]*Institute of Astronomy, Madingley Road, Cambridge CB3 0HA*

Accepted 2003 June 26. Received 2003 May 13; in original form 2002 December 9

ABSTRACT

In this first paper of a series, we report on the use of quasar spectra obtained with the high-resolution Ultraviolet–Visual Echelle Spectrograph (UVES) and available through the European Southern Observatory (ESO) Very Large Telescope (VLT) archive to build the first homogeneous and unbiased sample of sub-damped Lyman α (sub-DLA) systems, absorbers with H I column densities $>10^{19}$ cm^{-2} but lower than the classical definition of damped Lyman α systems (2×10^{20} cm^{-2}). A systematic investigation of the properties of these systems and a comparison with those of the DLAs (Paper II of this series) is expected to provide new clues on the association of high column density absorbers with galaxies and on the overall evolution of the neutral hydrogen gas mass and metal content in the Universe. In the spectra of 22 quasars which were found suitable for a sub-DLA search, we identified 12 sub-DLAs and one borderline case between the DLA and sub-DLA systems in the redshift interval $z = 1.8$–4.3. We measured the column densities of H I and of up to 16 additional ions of low, intermediate and high ionization: O I, C II, C IV, Si II, Si IV, N I, S II, Mg I, Mg II, Al II, Al III, Fe II, Fe III, Ni II, Zn II and Cr II. We further investigated the significance of the ionization corrections in the determination of the chemical abundances from the low-ionization ions in the sub-DLA H I column density range. Using the predictions of different ion ratios as a function of the ionization parameter computed using the CLOUDY software package, we have estimated that with the exception of one case, the ionization corrections to the abundances of nine systems for which we were able to constrain the ionization parameter are lower than 0.2 dex for all of the elements except Al II and Zn II down to H I column densities of $\log N(\mathrm{H\,I})=19.3$ cm^{-2}. Finally, we present the first sub-DLA chemical abundance data base, which contains the abundance measurements of 11 different elements (O, C, Si, N, S, Mg, Al, Fe, Ni, Zn and Cr). We took advantage of the lower H I column densities in sub-DLAs to measure, in particular, the O and C abundances using lines that are normally saturated in DLAs.

Key words: galaxies: abundances – galaxies: high-redshift – quasars: absorption lines – quasars: general.

1 INTRODUCTION

Galaxy formation and evolution remain important issues in our understanding of the early epoch of the Universe. Fundamental steps towards these issues would be the reconstruction of the chemical histories of galaxies and the metal census of the Universe. They are investigated both via the traditional approach of observing the galaxy starlight, and via the absorption-line systems detected along the quasar lines of sight independent of their distance, luminosity and morphology. The absorption-line systems, in particular, provide a very accurate observational method to measure the neutral gas and metal content of the Universe up to very high redshifts, $z > 4$ (e.g. Lu et al. 1996a; Dessauges-Zavadsky et al. 2001a; Prochaska, Gawiser & Wolfe 2001a; Songaila & Cowie 2002).

The quasar absorption-line systems are divided into three classes according to their neutral hydrogen column density: the Lyα forest

⋆E-mail: miroslava.dessauges@obs.unige.ch

with N(H I) ranging from $\sim 10^{12}$ to 1.6×10^{17} cm^{-2}, the Lyman-limit systems (LLs) with N(H I) $>1.6 \times 10^{17}$ cm^{-2} and the damped Lyman α systems (DLAs) with N(H I) $> 2.0 \times 10^{20}$ cm^{-2} (Wolfe et al. 1986). They thus probe different media from voids to haloes and discs of both dwarf and normal (proto)galaxies (Matteucci, Molaro & Vladilo 1997; Haehnelt, Steinmetz & Rauch 1998; Ledoux et al. 1998; Prochaska & Wolfe 1998; Jimenez, Bowen & Matteucci 1999; Calura, Matteucci & Vladilo 2003). The DLAs, in particular, are a cosmologically important population, since they dominate the neutral hydrogen content of the Universe (e.g. Wolfe et al. 1995; Storrie-Lombardi & Wolfe 2000) and are believed to be the progenitors of present-day galaxies.

A recent study by Péroux et al. (2003a) has, however, suggested that the relative importance of lower H I column density systems, the so-called 'sub-DLA systems' with H I column densities between 10^{19} and 2×10^{20} cm^{-2}, increases with redshift. Indeed, this until now poorly studied class of absorbers should contain approximately 45 per cent of the neutral hydrogen mass at $z > 3.5$, and may thus play an important role at high redshift in the study of the redshift evolution of both the total amount of neutral gas and the metal content in the Universe. The sub-DLAs, similarly to the DLAs, present the advantage that the H I column density of these systems can accurately be estimated thanks to the presence of damping wings in their Lyα lines, observed down to H I column densities of 10^{19} cm^{-2}.

At the present time only the chemical abundances of DLAs have been used to trace the metal content in the Universe, but this has shown unexpected results. Contrary to the cosmic chemical evolution model predictions (e.g. Pei & Fall 1995; Cen & Ostriker 1999; Pei, Fall & Hauser 1999; Cen et al. 2003), the most recent observations indicate only a mild evolution of the metal content with redshift (Pettini et al. 1999; Prochaska & Wolfe 2000; Vladilo et al. 2000; Dessauges-Zavadsky et al. 2001b; Prochaska & Wolfe 2002). Only Savaglio (2000), who focused on lower H I column density DLA systems, claims evidence for redshift evolution. If the Péroux et al. (2003a) predictions are confirmed, the sub-DLA metallicities should be taken into account in order to obtain a complete picture of the redshift evolution of the metal content of the Universe. Indeed, the current metallicity studies which focused only on the higher column density absorption-line systems, may have provided a biased and/or incomplete view of the global metal evolution in the Universe at $z > 3.5$. The observational confirmation of the impact of the sub-DLA systems at high redshift is thus crucial. In addition, the investigations of the chemical, kinematic and clustering properties of the sub-DLAs to see whether we are dealing with a different class of objects with a lower H I content/mass relative to the DLAs are further motivation for studying these absorbers. If sub-DLAs are the basic building blocks of the hierarchical growth of galactic structures as suggested by Péroux et al. (2003a), their abundance analysis may provide an insight into the very early stages of the chemical enrichment of galaxies.

The work presented in this paper therefore aims at constructing the first homogeneous sample of sub-DLA systems. For this purpose, we have used all of the high-resolution quasar spectra available to us in 2001 July in the ESO Ultraviolet-Visual Echelle Spectrograph-VLT (UVES-VLT) archives. Section 2 explains how the quasar spectra were selected and how the sub-DLA systems were identified. We provide a detailed chemical analysis for each sub-DLA system in Section 3, and we address the issues of the photoionization effects in Section 4. Finally, in Section 5, we summarize all the ionic column density and the absolute abundance measurements. In Paper II of this series (Péroux et al. 2003b), we use the data base presented here in combination with the data on DLAs and other sub-DLAs from the literature to discuss the overall properties of these objects.

2 CONSTRUCTION OF A HOMOGENEOUS SUB-DLA SAMPLE

All the observations presented in this paper were acquired with the Ultraviolet-Visual Echelle Spectrograph (UVES; see D'Odorico et al. 2000) on the VLT 8.2-m ESO telescope at Paranal, Chile, between the commissioning and the science verification time of the instrument at the end of 1999 and beginning of 2000, respectively, and 2000 July. All of these data reached the end of their 1 year long propriety period in 2001 July and could be retrieved from the ESO archives. A total of 35 high-resolution, high signal-to-noise (S/N) ratio quasar spectra were available, illustrating the success of both the instrument and the data distribution policy of the ESO archives.

2.1 Quasar selection

The goal of our study being well defined, we have selected from the 35 quasars available in the ESO UVES archives only the quasars suitable for the sub-DLA search. First, we took the conservative approach of excluding all quasars exhibiting broad absorption lines (BALs), since the nature of these objects and their characteristic features are not fully understood yet, rendering the distinction between true intervening absorption systems and other quasar spectral features difficult. However, we have not excluded the quasars selected for the study of associated systems, $z_{\rm abs} \simeq z_{\rm em}$, since the quasars considered in the ESO programme 65.P-0038 (see Table 1) do not exhibit BALs, which are often confused with associated absorbers. Secondly, we have excluded the quasars that were observed for the sole purpose of studying the Lyα forest (e.g. for the analysis of voids, low column density distribution). Indeed, these quasars have been pre-selected for having no high column density systems in their spectrum, precisely the type of systems we are looking for in the present study. In one case, however, a sub-DLA has been found in the later sample of quasars, the quasar Q1101−264 at $z_{\rm em} = 2.12$ observed during the UVES Science Verification. This absorber is included in the present abundance analysis, but for reasons of consistency it will be excluded from the study of the sub-DLA statistical properties (see Paper II).

The above selection process resulted in a sample of 22 quasars. A large majority of these quasars were observed with UVES because of their intervening DLA systems. There is a priori no reason why this should create a bias in our sample. We assume that the sub-DLA systems are not preferentially found close to the DLA systems. An analysis of the clustering properties of the sub-DLA systems identified in our sample is presented in Paper II.

Table 1 summarizes the observing programme details (i.e. the ESO programme number, the exposure time, the settings), the wavelength coverages, the redshifts of the 22 selected quasars and the redshifts of their intervening DLA systems. The sample of the selected quasars should result in the construction of an unbiased and homogeneous sample of sub-DLA systems.

2.2 Data reduction

The constructed sample of 22 quasars has benefited from a homogeneous data reduction. All of the quasar spectra were reduced using the ESO data reduction package MIDAS and the UVES pipeline in

Table 1. Observational properties of the selected quasar spectra from the ESO UVES archives and their intervening DLAs and sub-DLAs.

Quasar name	z_{em}	ESO prog. no	Settings	Wavelength coverage* (Å)	Exposure (s)	z_{DLA}	$z_{sub-DLA}$ +(Ref.)
Q0000−2620	4.11	Commissioning	B437+R860	3770–5000, 6700–10 500	19 700	3.390	...
APM BR J0307−4945	4.75	Commissioning	R600, R760, R800	5000–9900	26 300	4.466	?[a]
Q0347−3819	3.23	Commissioning	B427+R860	3655–4888, 6722–10 000	9500	3.025	...
Q0841+129	2.50	65.O-0063	B412+R860	3550–4740, 6710–10 000	5400	2.375	...
...	...	...	...	...	...	2.476	...
HE 0940−1050	3.05	65.O-0474	B346+R580	3600–3870, 4780–6809	3600	...	...
Q1038−272	2.32	65.O-0063	B437+R860	3765–4998, 6707–10 000	5400	...	...
Q1101−264[b]	2.14	Science Verification	B346+R580, B437+R860	3050–8530	45 000	...	1.838[b] (1)
HE 1104−1805[c]	2.31	Commissioning	B360, R670	3184–4024, 5698–7714	10 880	1.662	...
Q1151+068	2.76	65.O-0158	B346+R580, B437+R860	3100–10 000	21 600	1.774	...
PKS 1157+014	1.99	65.O-0063	B346+R550	3050–3870, 4500–6500	7200	1.944	...
Q1223+1753	2.94	65.P-0038, 65.O-0158	B390+R564, B437+R860	3300–10 000	18 000	2.466	2.557
PKS 1232+0815	2.57	65.P-0038	B390+R564	3300–6650	10 800	2.338	...
Q1409+095	2.86	65.O-0158	B437+R860	3769–4998, 6707–10 000	18 000	2.456	2.668 (2,3,4)
Q1444+014	2.21	65.O-0158	B390+R564	3294–6650	18 000	...	2.087 (3,5)
Q1451+123	3.25	65.O-0063	B424+R750	3640–4855, 5900–9400	7200	2.469	2.255[d] (2)
...	...	...	...	...	...	...	3.171[e] (1, 2)
Q1511+090	2.88	65.P-0038	B390+R564, B437+R860	3300–10 000	32 400	...	2.088
Q2059−360	3.09	65.O-0063	B480+R740	4200–5340, 5900–9300	10 800	3.083	2.507
Q2116−358	2.34	65.O-0158	B390+R564	3294–6650	7200	...	1.996 (6, 7, 8)
Q2132−433	2.42	65.O-0158	B390+R564	3294–6650	3600	1.914	...
PSS J2155+1358	4.26	65.O-0296	R565, R800	4633–9800	11 600	3.316	3.142
...	...	...	...	...	...	...	3.565
...	...	...	...	...	...	...	4.212
Q2206−199	2.56	65.O-0158	B390+R564, B437+R860	3294–10 000	25 200	1.920	...
...	...	...	...	...	...	2.076	...
PSS J2344+0342	4.24	65.O-0296	R565, R800	4633–9800	13 500	3.220	3.882

*With some gaps in the wavelength coverage.

[a]The detection of sub-DLAs is uncertain (see Section 3.1).

[b]This quasar has been observed for the study of the Lyα forest. Nevertheless, an analysis of the spectra revealed the presence of a sub-DLA. For consistency reasons, this system will not be included in the study of the sub-DLA statistical properties presented in Paper II.

[c]This quasar is gravitationally lensed. Only the brightest line of sight was included in our study.

[d] This absorption-line system is a borderline case between the DLA and sub-DLA systems with a H I column density of $\log N(\mathrm{H\,I}) = 20.30 \pm 0.15$. It is not included in the sub-DLA sample.

[e]The spectra do *not* cover the Lyα absorption line at $\lambda_{obs} \sim 5070$ Å of this sub-DLA. It has been identified thanks to the H I column density measurement reported by Petitjean et al. (2000).

References to the sub-DLAs already reported in the literature.

(1) Petitjean et al. (2000); (2) Lanzetta et al. (1991); (3) Pettini et al. (2002); (4) Lu et al. (1993); (5) Wolfe et al. (1995); (6) Lanzetta et al. (1987); (7) Wampler et al. (1993); (8) Møller et al. (1994).

Observing programmes.

65.P-0038: 'Probing the nuclear regions of QSOs with $z_{abs} \simeq z_{em}$ associated systems' (Srianand, Petitjean & Aracil).

65.O-0063: 'Molecular hydrogen at high redshift' (Ledoux, Petitjean, Srianand & Rauch).

65.O-0158: 'Abundance ratios in damped Lyα systems: clues to the nucleosynthesis of N and Mn' (Pettini, Bergeron & Petitjean).

65.O-0296: 'A study of the IGM–galaxy connection at $z = 3$ using the UVES high-quality absorption spectra' (D'Odorico, Cristiani, Fontana, Giallongo & Savaglio).

65.O-0474: 'Deuterium abundance in the high-redshift QSO absorption system towards HE 0940−1050' (Molaro, Centurión & Bonifacio).

an interactive mode available as a MIDAS context. A detailed description of the pipeline can be found in Ballester et al. (2000). To optimize the results we made a systematic check of each step of the pipeline reduction. Once reduced, the wavelengths of the one-dimensional spectra were converted to a vacuum-heliocentric scale, the individual spectra were co-added using their S/N ratio as weights to obtain the maximum signal-to-noise ratio, and the various settings were combined to obtain the maximum wavelength spectral coverage. An average resolution of 5–7 km s^{-1} FWHM was achieved in the spectra, and an average S/N ratio per pixel of between 10 and 150 is observed from spectrum to spectrum according to the exposure time and the magnitude of the quasar.

The final step was the normalization of the resulting spectra obtained by dividing them by a spline function fitted to smoothly connect the regions free from absorption features. The continuum in the Lyα forest was fitted by using small regions deemed to be free of absorptions and by interpolating between these regions with a spline. The higher the redshift of the quasar, the more difficult is the normalization in the Lyα forest due to the higher density of absorption lines (e.g. Kim, Cristiani & D'Odorico 2001). The procedure we applied for the normalization is the same as the one we used for two high-redshift and four intermediate-redshift quasars we have previously analysed for a detailed chemical abundance study of their intervening DLA systems (Dessauges-Zavadsky et al. 2001a; Dessauges-Zavadsky, Prochaska & D'Odorico 2002;

Levshakov et al. 2002). This procedure has proven to lead to an accuracy of the normalization level of approximately 5–10 per cent in the Lyα forest and better than 5 per cent redwards of the Lyα emission of the quasar (according to the signal-to-noise ratio of the spectra). For each quasar we tested the derived normalization first by selecting different regions in the continuum and by varying the number of these regions used for the fit of the continuum with a spline. In the Lyα forest, in particular, some regions are key regions in the continuum definition, when omitted, the shape and level of the continuum are drastically modified. We tried to qualitatively and quantitatively estimate these modifications. Secondly, we checked whether the adopted continuum fit is within the 1σ error of the spectra along the whole wavelength range sampled, and we estimated the normalization accuracy by determining the mean deviation of the adopted continuum fit from the observed continuum within its 1σ error and the maximum variation of this fit tolerated within the 1σ error of the spectra.

2.3 Sub-DLA identification

With the sample of quasars to be analysed being defined and their high-resolution spectra being reduced, we used these spectra to identify their intervening sub-DLA systems. In order to select all the sub-DLAs, we have used a detection algorithm equivalent to that applied by Péroux et al. (2001) to detect the DLAs in medium-resolution spectra ($\sim$2 Å pixel^{-1}), and which was previously used by Lanzetta et al. (1991), Wolfe et al. (1995) and Storrie-Lombardi & Wolfe (2000). This technique consists in building an equivalent width spectrum over 500 pixel wide boxes for each quasar. The analysis was performed 3000 km s^{-1} bluewards from the Lyα emission of the quasar in order to avoid possible contaminations from systems associated with the quasar itself, and it ended where the S/N ratio was too low to detect absorption features at the sub-DLA threshold, i.e. $EW_{rest} = 2.5$ Å.

Fig. 1 displays an example of the output of the sub-DLA search algorithm in the case of the quasar Q2116−358. The solid line is the equivalent width spectrum and the dotted line is the error array. The straight dashed line corresponds to the threshold above which the sub-DLA systems are detected. In this example, the sub-DLA system at $\sim$3640 Å ($z_{abs} = 1.996$) is clearly identified.

We then supplemented the sub-DLA candidates found by the algorithm with a visual identification. Indeed, since the algorithm selects any region with the required equivalent width regardless of the shape of the absorption feature and whether or not the absorption goes to zero, an additional check of the candidates is necessary to distinguish the true sub-DLAs from blends of several Lyα clouds. Three main visual criteria were used to identify a sub-DLA system: (i) the saturation of the absorption feature identified as the Lyα absorption line of the sub-DLA candidate; (ii) the presence of damping wings in the Lyα absorption lines which are clearly observed in the sub-DLA H I column density regime between 10^{19} and 2×10^{20} cm^{-2} as illustrated in Fig. 2; and (iii) the detection of lines of higher members of the Lyman series with the same H I column density as that measured from the Lyα line when the wavelength coverage is available. An additional visual criterion, though not necessary, was the identification of associated metal lines that are very likely to occur in absorbers with H I column densities greater than 10^{19} cm^{-2}. On the basis of these visual criteria and to impartially select the sub-DLAs, three of us (MD-Z, CP and T-SK) looked

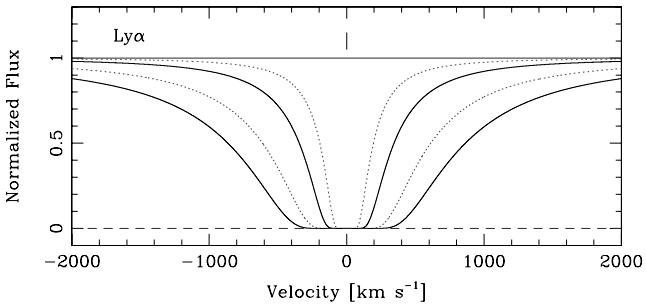

Figure 2. Lyα absorption-line profiles for four different H I column densities in the sub-DLA range: from left to right, log N(H I)=20.3 (solid line), 20.0 (dotted line), 19.5 (solid line) and 19.0 (dotted line) with the Doppler parameter b fixed at 20 km s^{-1}. This illustrates that in the sub-DLA range, $10^{19} < N(\mathrm{H\,I}) < 2 \times 10^{20}$ cm^{-2}, the damping wings are clearly observed.

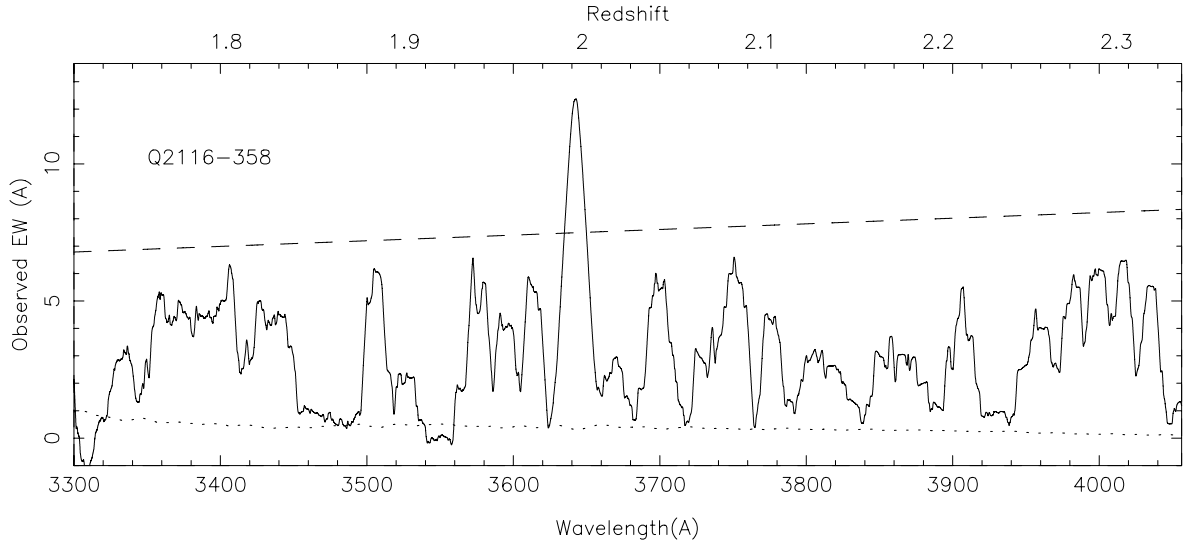

Figure 1. Output of the automated sub-DLA search algorithm for the quasar Q2116−358. The solid line corresponds to the equivalent-width spectrum and the dotted line to the error array. The straight dashed line represents the threshold above which the sub-DLA systems are detected. In this case a sub-DLA at $\sim$3640 Å ($z_{abs} = 1.996$) is clearly identified.

independently at the sub-DLA candidates found by the algorithm and closely inspected the original spectra to determine whether or not these absorption features correspond to sub-DLAs.

We reached a good agreement in all but one case, the quasar APM BR J0307−4945 at $z_{em} = 4.78$. Given the high redshift of this quasar the Lyα forest is very dense, and thus at three different redshifts the presence of sub-DLA systems is ambiguous (see Section 3.1). The absence of lines of higher members of the Lyman series for two of them does not allow us to draw a conclusion on the true H I column density of these systems, leading us to not include them in the sub-DLA sample. In the third candidate, the Lyman lines are heavily blended and prevent us from obtaining an accurate H I column density measurement, thus this candidate is also not analysed and not included in our sub-DLA sample. Moreover, the sub-DLA system at $z_{abs} = 3.171$ towards Q1451+123 has been identified thanks to the H I column density measurement reported by Petitjean, Srianand & Ledoux (2000), the spectra we had at our disposal do not cover the Lyα line of this system. With the lines of higher members of the Lyman series – Lyβ, Lyγ and Ly8 – we confirm the reported H I column density measurement of this absorption system (see Section 3.6.2). This system is included in the abundance analysis, but it is excluded from the study of the sub-DLA statistical properties (see Paper II), similarly to the sub-DLA system towards Q1101−264 (see the explanation in Section 2.1). Finally, the identified absorption-line system at $z_{abs} = 2.255$ towards Q1451+123 is a borderline case between the DLA and sub-DLA systems with a H I column density of log N(H I)=20.3 ± 0.15 (see Section 3.6.1). We provide a detailed abundance analysis of this system, but we do not consider it as a sub-DLA system, and thus we do not include it in the sub-DLA sample used for the different studies undertaken in Paper II.

In Table 1 we give the redshifts and the references of the 12 sub-DLAs and one borderline case between the DLA and sub-DLA systems detected towards the 22 selected quasars, and in Fig. 3 we show their H I column density distribution. The detected systems span a range of H I column densities from $10^{19.3}$ to $10^{20.3}$ cm^{-2}. No particular trend can be confirmed with this small number of objects yet. The sample of the 10 sub-DLAs, when excluding the sub-DLA towards Q1101−264 and towards Q1451+123, constitutes an unbiased and homogeneous sample of sub-DLAs, ideal for a statistical analysis (see Paper II).

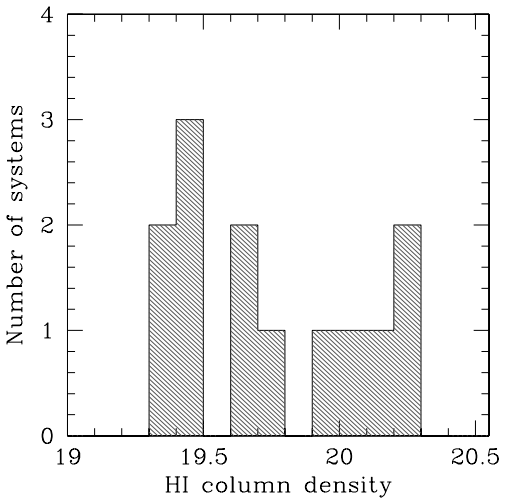

Figure 3. H I column density distribution of the 12 sub-DLA systems and one borderline case between the DLA and sub-DLA systems detected towards the 22 selected quasars.

3 IONIC COLUMN DENSITIES

In this section we present the ionic column density measurements of the 12 detected sub-DLA systems and one borderline case between the DLA and sub-DLA systems. All of the column densities of the metal species were derived with the Voigt profile fitting technique. This technique consists in fitting theoretical Voigt profiles to the observed absorption metal lines well described as a complex of components, each defined by a redshift z, a Doppler parameter b, a column density N and the corresponding errors. The fits were performed using a χ^2 minimization routine FITLYMAN in MIDAS (Fontana & Ballester 1995).

We assumed that all of the metal species with *similar ionization potentials* can be fitted using identical component fitting parameters, i.e. the same b (which means that macroturbulent motions dominate over thermal broadening) and the same z in the same component, and allowing for variations from metal species to metal species in N only. We distinguish three categories of metal species with similar ionization potentials: the low-ion transitions (i.e. the neutral and singly ionized species), the intermediate-ion transitions (e.g. Fe III, Al III) and the high-ion transitions (e.g. C IV, Si IV). By using relatively strong lines (but not saturated) to fix the component fitting parameters (the b and z values for each component), we then obtain excellent fitting results even for weak metal lines and for metal lines in the Lyα forest where the probability of blending is high, by allowing only the column density to vary. For all of the analysed systems exhibiting multicomponent velocity structures, we had a sufficient number of relatively strong metal lines to constrain the fitting parameters well.

Tables 2–14 present the results of the component per component ionic column density measurements for the fitting model solutions of the low-, intermediate- and high-ion transitions for all of the analysed systems. The reported errors are the 1σ errors computed using FITLYMAN. These errors do not take into account the uncertainties on the continuum level determination. For the saturated components, the column densities are listed as lower limits. The values reported as upper limits correspond to cases contaminated by significant line blendings due to H I clouds in the Lyα forest or telluric lines. Figs 5–29 (odd numbers) show the best-fitting solutions of the low-, intermediate- and high-ion transitions for all of the analysed systems. In these velocity plots, $v = 0$ corresponds to an arbitrary component, and all of the identified components are marked by small vertical bars. The thin solid line represents the best-fitting solution. We point out that the high-ion transitions in the bulk of sub-DLA systems present very different profiles from the low-ion transitions, whereas the intermediate-ion transitions show relatively similar profiles with small differences in the model fitting parameters. This will be discussed individually for each system in the following subsections.

The neutral hydrogen column densities were measured from the fits of the Lyα damping line profiles. The b-value was usually fixed at 20 km s^{-1} or left as a free parameter (similarly to the DLA systems the fit of the damped Lyα line of sub-DLA systems is independent of the b-value) and the redshift z was fixed at the redshift of one of the strongest components of the low-ion metal line profiles or also left as a free parameter depending on the sub-DLA system (see the comments in the following subsections). When other lines of higher members of the Lyman series were covered in the spectra, we used them to check the H I column density obtained from the fit

of the Lyα line. Figs 4–28 (even numbers) show the results of the H I fitting solutions for all of the analysed systems. The small vertical bar corresponds to the redshift used in the best-fitting solution and the thin solid line represents the best-fitting solution. In one case, the sub-DLA at $z_{\rm abs} = 3.171$ towards Q1451+123, the Lyα line is not covered in the available spectra, thus the H I column density measurement was performed using the Lyβ, Lyγ and Ly8 lines, the other members of the Lyman series being heavily blended.

Throughout the analysis we have adopted the list of atomic data (laboratory wavelengths and oscillator strengths) compiled by J. X. Prochaska and collaborators, and presented on the web site 'The HIRES Damped Lyα Abundance Data base'.[1] The most recent measurements of the λ and f-values of the metal ions that impact the abundances of high-redshift absorption systems and their references are reported there.

We now comment on the individual sub-DLA systems.

3.1 APM BR J0307−4945

The spectra of this quasar (Storrie-Lombardi et al. 2001) and the chemical abundances of one of the highest redshifted damped Lyα system discovered by Péroux et al. (2001) have been analysed in detail by Dessauges-Zavadsky et al. (2001a). Given the high redshift of this quasar ($z_{\rm em} = 4.75$) several intervening sub-DLA systems are expected. Three candidates at $z_{\rm abs} = 3.356$, 3.589 and 4.214 have been detected. However, the high density of absorption lines in the Lyα forest of such distant objects makes the blends of several absorption clouds very likely to occur. The lines of higher members of the Lyman series are necessary to distinguish blends of clouds from high H I column density absorbers. As discussed below, none of the three sub-DLA candidates can be confirmed in the considered spectra and they probably never will be. They thus are not included in any of our further analysis (this paper and Paper II).

For the two candidates at lower redshifts, $z_{\rm abs} = 3.356$ and 3.589, we do not have any information on the higher members of the Lyman series, these lines being beyond the quasar flux cut-off. Moreover, for the system at $z_{\rm abs} = 3.356$ no associated metal lines are observed. Thus, since the Lyα absorption lines of these two candidates do not show clearly any damping wing and since they can be fitted with a single system with N(H I) $> 10^{19}$ cm^{-2} and with several clouds of lower H I column densities, the identification of these sub-DLA candidates is doubtful, and we choose to consider these two detected absorption-line systems as unlikely sub-DLAs.

Several metal lines (C II, C III, C IV, Si II, Si III, Si IV, N III, Al III) and the hydrogen lines Lyα, Lyβ and Lyγ have been identified in the candidate at $z_{\rm abs} = 4.214$. From the metal line profiles two main subsystems can be clearly distinguished, separated by $\simeq$400 km s^{-1}. These two subsystems have already been carefully analysed by Levshakov et al. (2003). From their Monte Carlo Inversion analysis they determined the H I column densities of 1.4×10^{17} and 2.3×10^{17} cm^{-2} in the bluest and reddest subsystems, respectively, corresponding to values characterizing the class of the Lyman-limit absorbers. Although these recovered values are self-consistent, they are not necessarily a unique solution. Indeed, the N(H I) measurement in the reddest system is well constrained by the three observed hydrogen lines. However, all of the three hydrogen lines in the bluest system are highly blended, hence the real N(H I) value may be higher and can possibly be above the sub-DLA N(H I) definition threshold. Given this uncertainty, we prefer again to consider this absorption-line system only as a sub-DLA candidate.

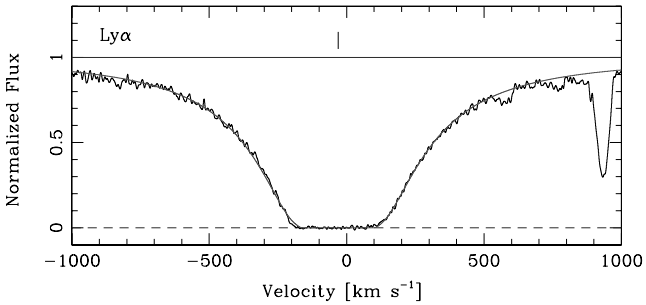

Figure 4. Normalized UVES spectrum of Q1101−264, showing the sub-DLA Lyα profile with the Voigt profile fit. The zero velocity is fixed at $z = 1.838\,902$. The vertical bar corresponds to the velocity centroid used for the best fit, $z = 1.838\,608$. The measured H I column density is $\log N(\mathrm{H\,I}) = 19.50 \pm 0.05$.

3.2 Q1101−264, $z_{\rm sub-DLA} = 1.838$

This quasar has been observed as part of the UVES Science Verification programme for the study of the Lyα forest (see Kim, Cristiani & D'Odorico 2002). It has previously been observed and analysed at lower resolution, and the absorption-line system at $z_{\rm abs} = 1.838$ we are interested in has already been identified (e.g. Carswell et al. 1984). Thanks to the large amount of UVES observing time devoted to this quasar, the spectra show an extremely high S/N ratio. The quality of the data allowed us to measure with high accuracy the column densities of 11 ions and seven elements (Si, O, S, C, Al, Fe, Mg) in the sub-DLA system at $z_{\rm abs} = 1.838$ observed in this line of sight. 4σ upper limits on the column densities of Zn II and Cr II have been provided, since these lines are not detected in the spectra. Only the hydrogen line, Lyα, is observed in the available spectral coverage, but the absence of contamination and the presence of well-defined damping wings lead to a very reliable N(H I) measurement of 19.50 ± 0.05 obtained by leaving the redshift and the b-value as free parameters (see Fig. 4). This absorber has already been studied by Petitjean et al. (2000) with regard to its molecular content. We confirm their H I column density measurement and their [Fe/H][2] and [S/H] abundance measurements.

The component structure of this absorber is presented in Table 2 for the low-, intermediate- and high-ion transitions. The low-ion profiles are described with a relatively complex structure of 11 components extended over $\sim$210 km s^{-1}, while the high-ion transitions are well fitted with only six components (see Fig. 5). This difference in the line profiles suggests that the low- and high-ion lines are not emitted from the same physical region, which is a commonly observed situation in DLAs. Nevertheless, in this particular case, surprisingly the lines of C^{3+} and Si^{3+}, two ions with the same ionization degree, do not show the same line profiles and require slightly different fitting parameters (z, b and N). In addition, the Al III lines better resemble the high-ion transition profiles than the low-ion ones, contrary to what is usually observed in DLA studies where the intermediate-ion line profiles are very similar to the low-ion line profiles, indicating they are emitted from the same physical region. Unfortunately, no other intermediate-ion is detected in this sub-DLA system to confirm these observations.

[1] http://kingpin.ucsd.edu/~hiresdla/

[2] $[\mathrm{X/H}] \equiv \log [N(\mathrm{X})/N(\mathrm{H})]_{\rm DLA} - \log [N(\mathrm{X})/N(\mathrm{H})]_{\odot}$.

Table 2. Component structure of the $z_{abs} = 1.838$ sub-DLA system towards Q1101−264.

No	z_{abs}	v^*_{rel} (km s^{-1})	$b(\sigma_b)$ (km s^{-1})	Ion	log $N(\sigma_{\log N})$ (cm^{-2})	No	z_{abs}	v^*_{rel} (km s^{-1})	$b(\sigma_b)$ (km s^{-1})	Ion	log $N(\sigma_{\log N})$ (cm^{-2})
Low-ion transitions											
1	1.837 407	−158	3.0$_{(0.9)}$	C II	12.30$_{(0.03)}$	8	1.838 902	0	5.3$_{(0.1)}$	Si II	13.61$_{(0.01)}$
				Mg II	11.45$_{(0.04)}$					O I	14.10$_{(0.15)}$
2	1.837 507	−147	4.3$_{(0.5)}$	C II	12.65$_{(0.01)}$					S II	13.23$_{(0.08)}$
				Mg II	11.70$_{(0.04)}$					C II	14.70$_{(0.08)}$
3	1.837 711	−126	6.9$_{(0.1)}$	Si II	12.23$_{(0.05)}$					Al II	12.26$_{(0.05)}$
				C II	13.29$_{(0.02)}$					Fe II	13.14$_{(0.01)}$
				Al II	11.50$_{(0.05)}$					Mg II	13.69$_{(0.02)}$
				Fe II	11.48$_{(0.04)}$					Mg I	11.49$_{(0.01)}$
				Mg II	12.40$_{(0.02)}$	9	1.839 144	+26	8.4$_{(0.3)}$	Si II	12.86$_{(0.02)}$
4	1.838 201	−74	7.8$_{(0.2)}$	Si II	12.55$_{(0.03)}$					O I	13.80$_{(0.11)}$
				C II	13.44$_{(0.08)}$					C II	13.55$_{(0.05)}$
				Al II	11.70$_{(0.02)}$					Al II	11.61$_{(0.04)}$
				Fe II	11.82$_{(0.02)}$					Fe II	12.58$_{(0.04)}$
				Mg II	12.59$_{(0.01)}$					Mg II	12.64$_{(0.04)}$
5	1.838 326	−61	5.9$_{(0.2)}$	Si II	12.49$_{(0.03)}$					Mg I	11.01$_{(0.02)}$
				C II	13.24$_{(0.05)}$	10	1.839 249	+37	2.0$_{(0.3)}$	Si II	12.46$_{(0.03)}$
				Al II	11.46$_{(0.03)}$					O I	13.34$_{(0.11)}$
				Fe II	11.67$_{(0.02)}$					C II	13.12$_{(0.04)}$
				Mg II	12.30$_{(0.02)}$					Al II	11.20$_{(0.03)}$
6	1.838 542	−38	6.0$_{(0.1)}$	Si II	13.37$_{(0.01)}$					Fe II	12.20$_{(0.04)}$
				O I	13.77$_{(0.02)}$					Mg II	12.36$_{(0.04)}$
				S II	13.13$_{(0.10)}$					Mg I	10.88$_{(0.03)}$
				C II	14.60$_{(0.08)}$	11	1.839 334	+46	5.2$_{(0.1)}$	Si II	12.48$_{(0.03)}$
				Al II	12.29$_{(0.08)}$					O I	13.30$_{(0.10)}$
				Fe II	12.83$_{(0.01)}$					C II	13.29$_{(0.03)}$
				Mg II	13.58$_{(0.06)}$					Al II	11.50$_{(0.02)}$
				Mg I	11.29$_{(0.02)}$					Fe II	11.97$_{(0.02)}$
7	1.838 712	−20	8.0$_{(0.3)}$	Si II	13.19$_{(0.01)}$					Mg II	12.40$_{(0.01)}$
				O I	13.83$_{(0.02)}$						
				S II	13.19$_{(0.15)}$						
				C II	13.99$_{(0.06)}$						
				Al II	12.10$_{(0.08)}$						
				Fe II	12.64$_{(0.01)}$						
				Mg II	13.08$_{(0.02)}$						
				Mg I	10.97$_{(0.02)}$						
Intermediate-ion transitions											
1	1.838 240	−70	13.0$_{(1.4)}$	Al III	11.75$_{(0.04)}$	3	1.838 865	−4	14.5$_{(1.2)}$	Al III	11.82$_{(0.04)}$
2	1.838 574	−35	14.9$_{(1.3)}$	Al III	11.99$_{(0.03)}$						
High-ion transitions											
1	1.837 500	−148	10.5$_{(0.4)}$	Si IV	12.59$_{(0.02)}$	4	1.838 591	−33	14.5$_{(0.2)}$	Si IV	13.34$_{(0.03)}$
	1.837 485	−150	9.2$_{(0.2)}$	C IV	12.86$_{(0.03)}$		1.838 570	−35	16.0$_{(0.2)}$	C IV	13.45$_{(0.02)}$
2	1.837 715	−125	8.5$_{(0.1)}$	Si IV	13.02$_{(0.02)}$	5	1.838 942	+4	15.6$_{(0.2)}$	Si IV	13.13$_{(0.04)}$
	1.837 718	−125	12.1$_{(0.1)}$	C IV	13.41$_{(0.02)}$		1.838 970	+7	14.7$_{(0.1)}$	C IV	13.76$_{(0.03)}$
3	1.838 210	−73	15.5$_{(0.2)}$	Si IV	13.22$_{(0.12)}$	6	1.839 337	+46	9.2$_{(0.4)}$	Si IV	12.40$_{(0.02)}$
	1.838 176	−77	20.7$_{(0.2)}$	C IV	13.62$_{(0.08)}$		1.839 365	+49	17.6$_{(0.8)}$	C IV	12.67$_{(0.03)}$

*Velocity relative to $z = 1.838\,902$.

3.3 Q1223+1753, $z_{\mathbf{sub-DLA}} = 2.557$

This quasar, also called LBQS 1223+1753, was discovered by Foltz et al. (1987) and it has been observed on many occasions for the study of its intervening DLA system at $z_{abs} = 2.466$. The large H I column density of this absorber allows the analysis of a great number of transitions (over 20) and of the H_2 molecule (e.g. Pettini et al. 1994; Centurión et al. 2000; Petitjean et al. 2000; Ellison, Ryan & Prochaska 2001; Prochaska et al. 2001b). In addition to this DLA, we identified a sub-DLA system at $z_{abs} = 2.557$ with a log N(H I) value of 19.32 ± 0.15, and we present here for the first time its chemical analysis.

This sub-DLA system was identified thanks to its Lyα absorption line, the only hydrogen line observed in the available spectra. This line shows a well-defined blue damping wing, but the red damping wing is partially blended with H I clouds (see Fig. 6). The H I column density measurement was hampered by an additional difficulty, the location of the sub-DLA Lyα line in the red wing of the DLA Lyα line. Therefore, we first had to locally renormalize the quasar spectrum with the fit of the DLA Lyα damping wing profile, before measuring the N(H I) of the sub-DLA by fixing the redshift at the position of the strongest component of the metal line profiles (component 6). The error on the derived hydrogen column density was estimated by varying the continuum level by 5 per cent.

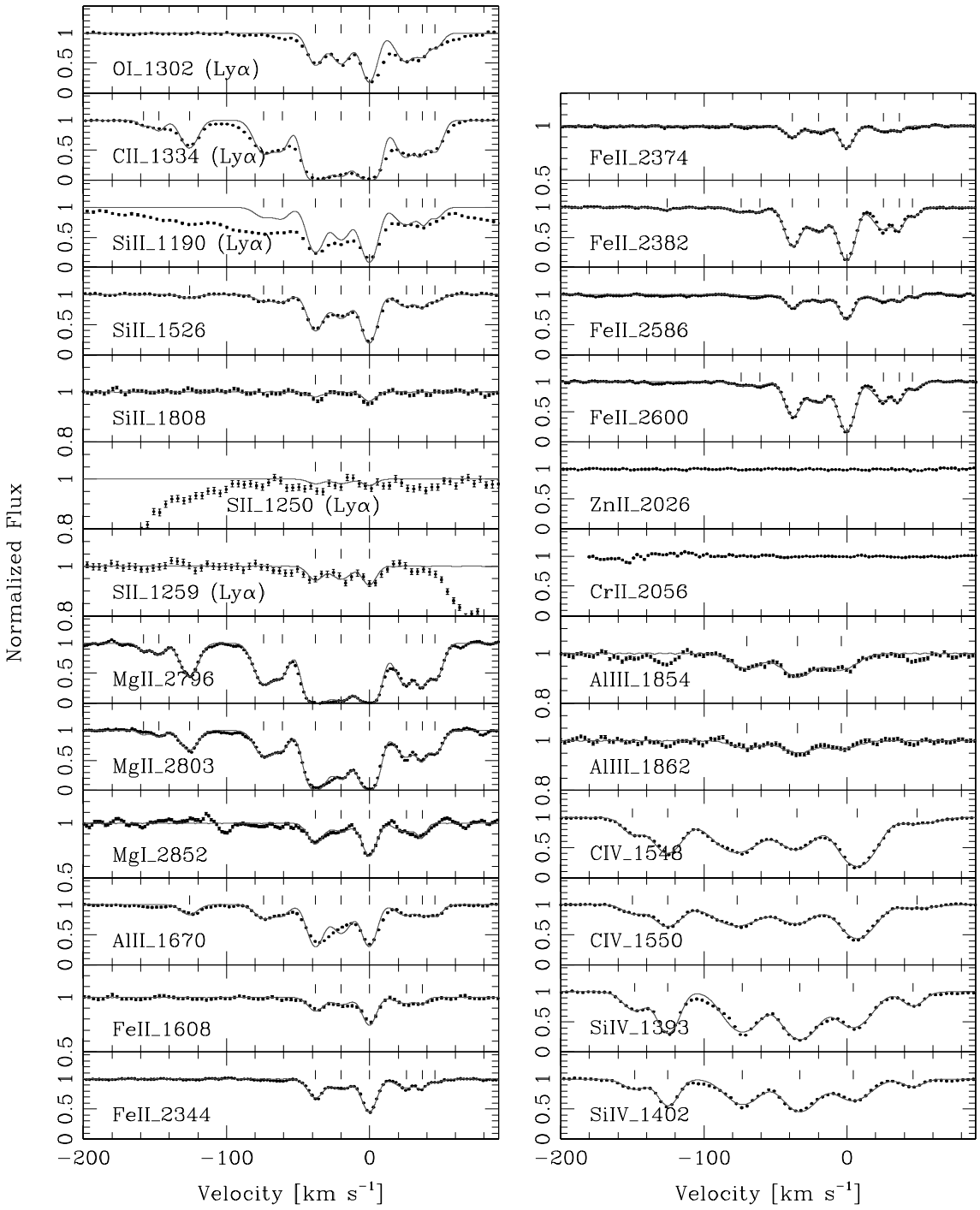

Figure 5. Velocity plots of the low-, intermediate- and high-ion transitions (normalized intensities shown by dots with 1σ error bars) for the sub-DLA towards Q1101−264. The zero velocity is fixed at $z = 1.838\,902$. The vertical bars mark the positions of the fitted velocity components (see Table 2). For this and all the following figures, the notation '(Lyα)' near the name of a transition means that the line is located in the Lyα forest, and the symbols $\oplus$ correspond to telluric lines.

As shown in Fig. 7 the low-ion transitions of the sub-DLA system present a complex velocity structure composed of 11 components spread over $\sim$210 km s^{-1} (see Table 3). The numerous Fe^{+} lines identified in the system (Fe II $\lambda\lambda$1608,2382,2586,2600) allowed one to obtain a very accurate N(Fe II) measurement. We also provide measurements of the Si II and Al II column densities. To be conservative, we prefer to consider the measured N(O I) obtained from the O I $\lambda\lambda$1039,1302 lines located in the Lyα forest as an upper limit. The Zn II and Cr II lines are not detected in the spectra, we provide 4σ upper limits. The C II lines are highly saturated.

In addition, we observe the C IV and Si IV high-ion transitions showing in this case very similar line profiles to the low-ion transitions. The C IV λ1550 and Si IV λ1402 lines are blended with the metal lines of other absorbers (see Fig. 7). We also detect the Al III

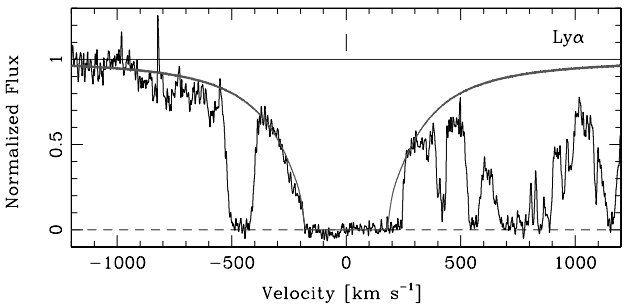

Figure 6. Normalized UVES spectrum of Q1223+1753, showing the sub-DLA Lyα profile with the Voigt profile fit. The zero velocity is fixed at $z = 2.557\,640$. The vertical bar corresponds to the velocity centroid of the strongest component of the low-ion transition lines used for the best fit, component 6 at $z = 2.557\,640$. The measured H I column density is $\log N(\mathrm{H\,I})=19.32 \pm 0.15$.

and Fe III intermediate-ion transitions. The intermediate-ion column density determination, in particular that of Fe^{2+}, is crucial for the estimation of the ionization corrections, which may not be negligible in this low H I column density system (see Section 4). Since the Al III lines are weak and the Fe III line is in the Lyα forest where blends with H I clouds are possible, we cannot determine with high accuracy whether the intermediate-ion profiles present differences with respect to the low-ion profiles in this sub-DLA system. Thus, as the Al III lines show a single velocity component located exactly at the redshift of the strongest component of the low-ion line profiles, component 6, we assume that we can adopt the same fitting parameters for the intermediate-ion transitions as those defined for the low-ion transitions.

3.4 Q1409+095, $z_{\mathrm{sub-DLA}} = 2.668$

Discovered by Hazard et al. (1986), this quasar was first studied at low resolution by Lanzetta et al. (1991) and then by Lu et al. (1993), for example. They reported the identification of a DLA system at $z_{\mathrm{abs}} = 2.456$ and another absorption-line system at $z_{\mathrm{abs}} = 2.668$ with a H I column density below the DLA definition corresponding to a sub-DLA system. Pettini et al. (2002) studied these two systems at high resolution and obtained the abundance measurements of O, Si, N and Fe. We identified the sub-DLA system in the UVES spectra thanks to the Lyα absorption line with clearly visible damping wings (see Fig. 8), and derived a H I column density of $\log N(\mathrm{H\,I})= 19.75 \pm 0.10$ in agreement with the measurement of Pettini et al.

Our determinations of the O I, Si II and Fe II column densities and of the N I upper limit are also consistent with their findings, although we obtained ∼0.1 dex higher Si II and Fe II column

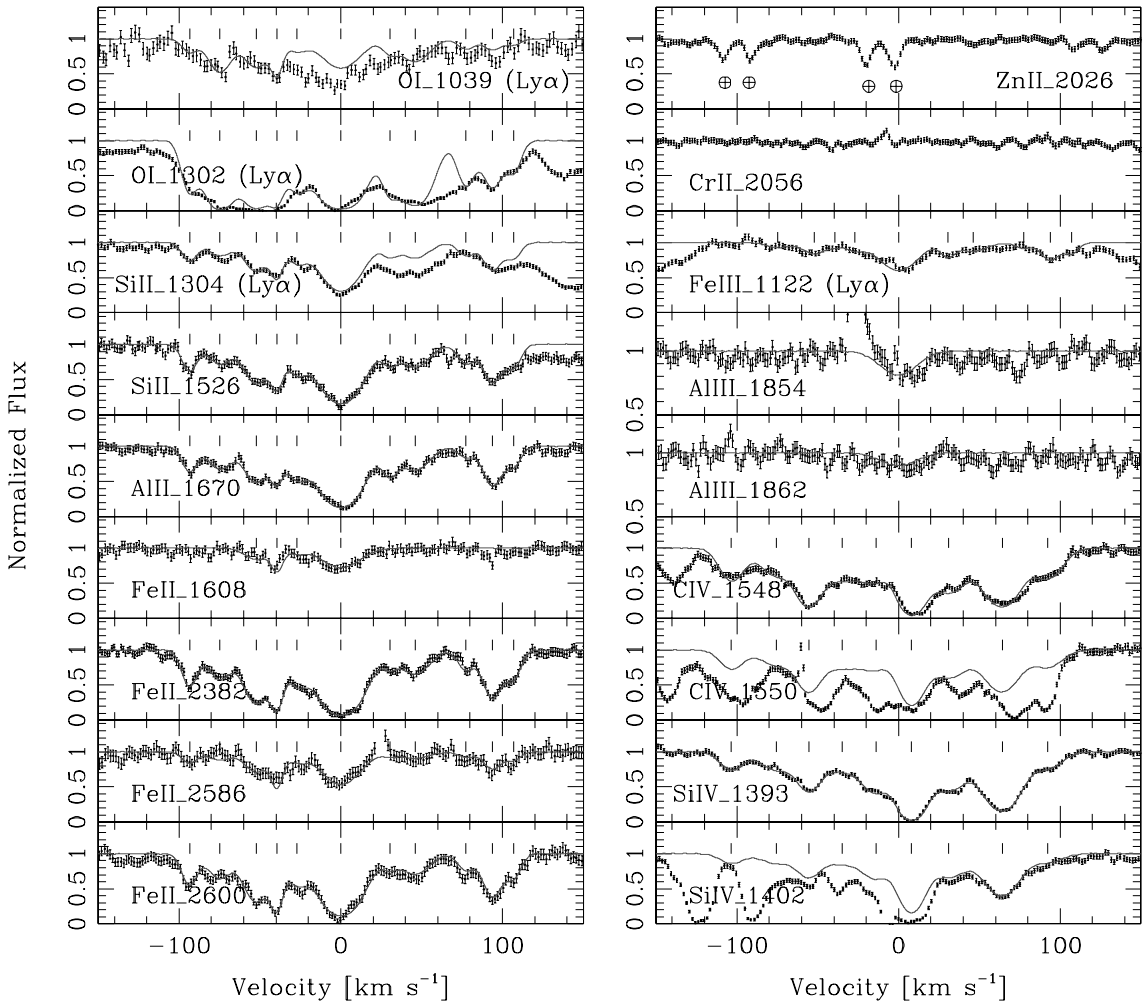

Figure 7. Same as in Fig. 5 for the sub-DLA towards Q1223+1753. The zero velocity is fixed at $z = 2.557\,640$. The vertical bars mark the positions of the fitted velocity components (see Table 3).

Table 3. Component structure of the $z_{abs} = 2.557$ sub-DLA system towards Q1223+1753.

No	z_{abs}	v^*_{rel} (km s^{-1})	$b(\sigma_b)$ (km s^{-1})	Ion	log $N(\sigma_{\log N})$ (cm^{-2})	No	z_{abs}	v^*_{rel} (km s^{-1})	$b(\sigma_b)$ (km s^{-1})	Ion	log $N(\sigma_{\log N})$ (cm^{-2})
Low- and intermediate-ion transitions											
1	2.556 532	−93	$4.8_{(0.5)}$	Si II	$13.03_{(0.04)}$	7	2.558 001	+30	$4.6_{(0.7)}$	Si II	$12.79_{(0.03)}$
				O I	<13.98					O I	<13.93
				Al II	$11.80_{(0.03)}$					Al II	$11.83_{(0.05)}$
				Fe II	$12.62_{(0.02)}$					Fe II	$12.09_{(0.10)}$
2	2.556 755	−75	$8.3_{(0.5)}$	Si II	$13.02_{(0.04)}$					Fe III	$13.16_{(0.15)}$
				O I	<14.62	8	2.558 186	+46	$11.1_{(1.1)}$	Si II	$13.21_{(0.03)}$
				Al II	$11.90_{(0.03)}$					O I	<14.51
				Fe II	$12.64_{(0.02)}$					Al II	$12.04_{(0.04)}$
				Fe III	$12.89_{(0.14)}$					Fe II	$12.65_{(0.03)}$
3	2.557 023	−52	$8.8_{(0.8)}$	Si II	$13.45_{(0.01)}$					Fe III	$13.24_{(0.13)}$
				O I	<14.55	9	2.558 559	+77	$5.6_{(2.0)}$	Si II	$12.91_{(0.04)}$
				Al II	$12.19_{(0.02)}$					O I	<13.90
				Fe II	$13.09_{(0.03)}$					Al II	$11.44_{(0.12)}$
				Fe III	$13.28_{(0.13)}$					Fe II	$12.32_{(0.08)}$
4	2.557 174	−39	$2.6_{(0.3)}$	Si II	$13.27_{(0.02)}$					Fe III	$12.83_{(0.14)}$
				O I	<14.31	10	2.558 752	+94	$6.1_{(1.0)}$	Si II	$13.32_{(0.02)}$
				Al II	$11.89_{(0.04)}$					O I	<13.95
				Fe II	$13.16_{(0.05)}$					Al II	$12.15_{(0.05)}$
				Fe III	$12.40_{(0.07)}$					Fe II	$12.90_{(0.04)}$
5	2.557 317	−27	$7.2_{(0.9)}$	Si II	$13.17_{(0.02)}$					Fe III	$13.39_{(0.14)}$
				O I	<14.04	11	2.558 908	+107	$4.5_{(1.2)}$	Si II	$12.93_{(0.05)}$
				Al II	$12.04_{(0.02)}$					O I	<13.60
				Fe II	$12.67_{(0.04)}$					Al II	$11.67_{(0.11)}$
				Fe III	$13.03_{(0.14)}$					Fe II	$12.46_{(0.09)}$
6	2.557 640	0	$14.8_{(0.3)}$	Si II	$14.00_{(0.01)}$					Fe III	$13.08_{(0.15)}$
				O I	<14.76						
				Al II	$12.85_{(0.01)}$						
				Fe II	$13.56_{(0.01)}$						
				Fe III	$13.94_{(0.12)}$						
				Al III	$12.32_{(0.13)}$						
High-ion transitions											
1	2.556 414	−103	$8.8_{(1.0)}$	Si IV	$12.43_{(0.03)}$	6	2.557 734	+8	$8.9_{(0.2)}$	Si IV	$13.53_{(0.01)}$
				C IV	$13.15_{(0.12)}$					C IV	$13.84_{(0.02)}$
2	2.556 744	−75	$12.5_{(1.1)}$	Si IV	$12.57_{(0.03)}$	7	2.558 007	+31	$13.7_{(0.9)}$	Si IV	$13.04_{(0.03)}$
				C IV	$13.18_{(0.12)}$					C IV	$13.52_{(0.03)}$
3	2.556 981	−56	$8.6_{(0.6)}$	Si IV	$12.83_{(0.05)}$	8	2.558 402	+64	$13.0_{(0.2)}$	Si IV	$13.37_{(0.01)}$
				C IV	$13.56_{(0.04)}$					C IV	$13.75_{(0.01)}$
4	2.557 225	−35	$16.1_{(2.9)}$	Si IV	$12.70_{(0.08)}$	9	2.558 732	+92	$11.2_{(1.1)}$	Si IV	$12.48_{(0.03)}$
				C IV	$13.37_{(0.08)}$					C IV	$13.18_{(0.02)}$
5	2.557 476	−14	$10.2_{(0.5)}$	Si IV	$12.92_{(0.03)}$						
				C IV	$13.14_{(0.07)}$						

*Velocity relative to $z = 2.557\,640$.

densities. This discrepancy may be explained by the fact that we used a two-component fitting model for the low-ion transitions (see Table 4), while these authors used a one-component fitting model. Indeed, weak metal lines, such as the N I, S II lines and some Fe II lines with low oscillator strengths, are well fitted with a single component. However, as shown in Fig. 9, the strong Fe II λλ2382,2586,2600, O I λ1302, Si II λ1190 and C II λλ1036,1334 line profiles clearly indicate the presence of a second weaker component at ∼11 km s^{-1} bluewards of the main component. In addition to the O^0, Si^+, Fe^+ column densities and the N(N I) upper limit – the N^0 triplet being blended with the Lyα forest absorptions – we obtained the column density measurements of S^+ from the S II λλ1250,1259 lines and Cr^+. The Zn II lines are not detected, thus we provide a 4σ upper limit. We also report a lower limit on N(C II), since the feature is saturated.

We detect the Al^{2+} and Fe^{2+} intermediate-ion transitions in this sub-DLA system. A single component is observed in the Al III λ1854 and λ1862 line profiles, and it is reasonably well fitted with the low-ion transition fitting parameters (see Fig. 9). Although the fit of the Al III λ1854 component does not look optimal and could be shifted by a few km s^{-1} bluewards, when fitting simultaneously the two Al III lines at $\lambda_{rest} = 1854$ and 1862 Å the best-fitting solution is very similar to the low-ion transition fitting parameters. Thus, given the weak intensity of the Al III and Fe III absorption lines and the low S/N ratio in the spectral regions covering these lines, we preferred to adopt the same fitting parameters as those derived for the low-ion transition lines, and we obtained Al III and marginal Fe III column density measurements. No high-ion transition line is observed, all of them being outside the available wavelength coverage.

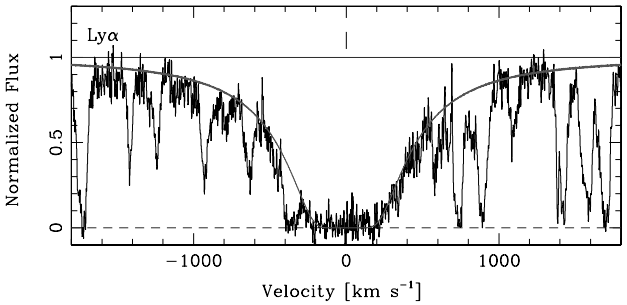

Figure 8. Normalized UVES spectrum of Q1409+095 showing the sub-DLA Lyα profile with the Voigt profile fit. The zero velocity is fixed at $z = 2.668\,227$. The vertical bar corresponds to the velocity centroid of the strongest component of the low-ion transition lines used for the best fit, component 2 at $z = 2.668\,227$. The measured H I column density is $\log N(\mathrm{H\,I}) = 19.75 \pm 0.10$.

Table 4. Component structure of the $z_{\rm abs} = 2.668$ sub-DLA system towards Q1409+095.

No	$z_{\rm abs}$	$v^*_{\rm rel}$ (km s^{-1})	$b(\sigma_b)$ (km s^{-1})	Ion	$\log N(\sigma_{\log N})$ (cm^{-2})
Low- and intermediate-ion transitions					
1	2.668 092	−11	$2.1_{(0.9)}$	Si II	$13.32_{(0.04)}$
				O I	$14.24_{(0.15)}$
				C II	>16.00
				Fe II	$13.63_{(0.24)}$
2	2.668 227	0	$4.8_{(0.4)}$	Si II	$14.06_{(0.03)}$
				O I	$15.27_{(0.11)}$
				C II	>15.37
				S II	$13.54_{(0.06)}$
				N I	<13.49
				Cr II	$12.49_{(0.15)}$
				Fe II	$13.79_{(0.05)}$
				Fe III	$13.17_{(0.12)}$
				Al III	$11.89_{(0.05)}$

*Velocity relative to $z = 2.668\,227$.

3.5 Q1444+014, $z_{\rm sub-DLA} = 2.087$

The quasar Q1444+014 is found more commonly under the name LBQS 1444+0126 and was discovered by Hewett et al. (1991). Its intervening absorption system at $z_{\rm abs} = 2.087$ was first reported by Wolfe et al. (1995). Pettini et al. (2002) analysed the H I, O I, Si II, N I and Fe II lines of this absorber, loosely referring to it as a DLA system. We derived the H I column density by fitting the weakly contaminated Lyα absorption line, showing well-defined damping wings (the redshift was left as a free parameter; see Fig. 10), and we classified the system as a sub-DLA with $\log N(\mathrm{H\,I}) = 20.18 \pm 0.10$, in agreement with the measurement of Pettini et al.

The low-ion transition profiles of this sub-DLA system exhibit a very complex velocity structure with 14 components extended over ∼350 km s^{-1} (see Table 5 and Fig. 11). We obtained column density measurements of Si II, Al II and Fe II. Only the strongest components are observed in the Fe II λλ1144,1608 line profiles. Unfortunately, several components between $v \simeq 0$ and −150 km s^{-1} of the O I λ1302 and C II λ1334 lines are saturated, thus we could only provide lower limits on the column densities of these two metal transitions. No intermediate-ion line was detected. We therefore give only the 4σ upper limits on N(Al III) and N(Fe III) – the Fe III λ1122 line is located in the Lyα forest, but the spectral region where the strongest components of the Fe III line should be detected is free from important H I blendings, and thus we can derive a reliable 4σ upper limit on N(Fe III). A very surprising particularity observed in this system is the behaviour of the high-ion transition lines, C IV and Si IV. They are characterized by only two relatively weak components and are extended over a much narrower velocity range of ∼40 km s^{-1} than the low-ion profiles (see Table 5 and Fig. 11). Most of the DLA systems show the opposite situation with the high-ion line profiles spread over a larger velocity range than the low-ion line profiles.

3.6 Q1451+123

The absorption-line systems towards this quasar discovered by Hazard et al. (1986) have first been studied by Wolfe et al. (1986). Lanzetta et al. (1991) identified in their low-resolution spectra a DLA system at $z_{\rm abs} = 2.469$ and two other absorption systems at $z_{\rm abs} = 2.255$ and 3.171. Petitjean et al. (2000) studied the intervening DLA and sub-DLA at $z_{\rm abs} = 3.171$ for their molecular content and report some of their elemental abundances. Here we present, for the first time, the abundance analysis of the additional system at $z_{\rm abs} = 2.255$ which is a borderline case between the DLA and sub-DLA systems.

3.6.1 $z_{\rm DLA/sub-DLA} = 2.255$

This absorption metal-line system was identified thanks to the Lyα absorption line observed only ∼100 Å away from the blue edge of the quasar spectrum (the quasar flux cut-off is at ∼3835 Å). The normalization is very difficult in this region, but the limited number of Lyα forest absorptions leads to a clear high H I column density system detection, the damping wings being well observed (see Fig. 12). We obtained a hydrogen column density measurement of $\log N(\mathrm{H\,I}) = 20.30 \pm 0.15$, which shows that this absorber is a borderline case between the DLA and sub-DLA systems. A large error bar on N(H I) was adopted to take into account the uncertainty in the continuum level. This absorption-line system, although analysed in this paper, is not considered as a sub-DLA and is not included in the sub-DLA sample used for the different studies undertaken in Paper II.

Table 6 and Fig. 13 present the velocity structure of the low-ion transitions in this absorber. It is characterized by five components spread over ∼130 km s^{-1}. We obtained the column density measurements of Zn^+, Cr^+ and Fe^+ from the Fe II λλ2374,2382,2600 lines. Only the strongest components, components 1–3, are observed in the weak Zn II and Cr II lines detected thanks to the relatively high H I column density of the system. Several interesting metal lines are unfortunately located in the spectral wavelength gap between 4855 and 5900 Å. The only observed Si^+ line in the available spectra is the saturated Si II λ1304 line which is, in addition, blended with the damping red wing of the Lyα line of the DLA system at $z_{\rm abs} = 2.469$. To obtain a correct lower limit we first had to renormalize the portion of the quasar spectrum around the Si II line with the fit of the DLA Lyα damping wing profile. The Ni II λλ1317,1370 lines located in the Lyα forest are detected at the noise level and at the uncertainty level of the continuum placement. We therefore considered the measured Ni^+ column density as an upper limit. The O I λ1302, C II λ1334 and the Mg II doublet lines are also detected, but these lines are so highly saturated that no useful lower limit can be deduced.

From the higher ionization transitions, only the Al^{2+} intermediate-ion lines and the Si^{3+} high-ion lines are covered in

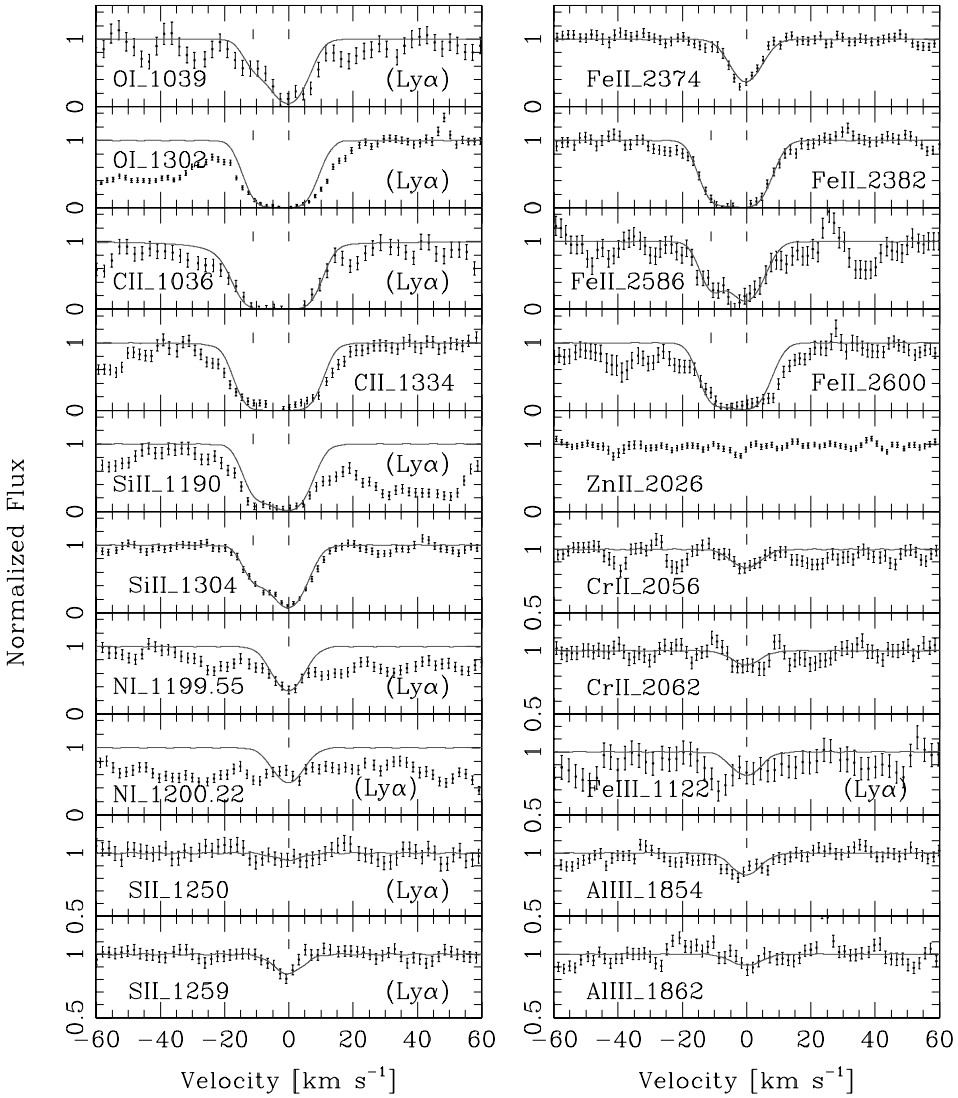

Figure 9. Same as in Fig. 5 for the sub-DLA towards Q1409+095. The zero velocity is fixed at $z = 2.668\,227$. The vertical bars mark the positions of the fitted velocity components (see Table 4).

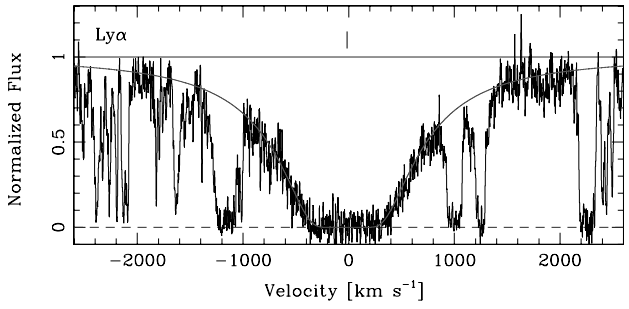

Figure 10. Normalized UVES spectrum of Q1444+014 showing the sub-DLA Lyα profile with the Voigt profile fit. The zero velocity is fixed at $z = 2.086\,808$. The vertical bar corresponds to the velocity centroid used for the best fit, $z = 2.086\,643$. The measured H I column density is $\log N(\mathrm{H\,I})=20.18 \pm 0.10$.

the available spectra. The Al III lines clearly show slightly different profiles from the low-ion profiles, but with a very similar trend (see Fig. 13). We provide an Al^{2+} column density measurement obtained with the fitting parameters given in Table 6. No column density measurement can be obtained from the Si IV doublet, since it is heavily blended with Lyα forest absorptions.

3.6.2 $z_{\mathrm{sub-DLA}} = 3.171$

The Lyα absorption line of this sub-DLA system is outside the available spectral coverage. We identified this sub-DLA system thanks to the H I column density measurement reported by Petitjean et al. (2000). They estimated the hydrogen column density of this system from the equivalent width measurement by Bechtold (1994) and give $\log N(\mathrm{H\,I}) \simeq 19.70$. We confirm this value with the measurements obtained from the fits of the Lyβ, Lyγ and Ly8 lines (the redshift and the b-value were left as free parameters; see Fig. 14). The other members of the Lyman series were not taken into account, being heavily blended with Lyα forest absorptions.

This sub-DLA system shows a very simple velocity structure. The low-ion transition profiles are well fitted with two components (see Table 7 and Fig. 15). We obtained the column density measurements of Si^+, C^+, Al^+ and Fe^+, and confirm the Petitjean et al. (2000) [Fe/H] and [Si/H] abundance measurements. The C II column density was deduced from the C II λ1036 line located in the

Table 5. Component structure of the $z_{\rm abs} = 2.087$ sub-DLA system towards Q1444+014.

No	$z_{\rm abs}$	$v^*_{\rm rel}$ (km s^{-1})	$b(\sigma_b)$ (km s^{-1})	Ion	log $N(\sigma_{\log N})$ (cm^{-2})	No	$z_{\rm abs}$	$v^*_{\rm rel}$ (km s^{-1})	$b(\sigma_b)$ (km s^{-1})	Ion	log $N(\sigma_{\log N})$ (cm^{-2})
Low-ion transitions											
1	2.085 060	−170	$10.9_{(1.0)}$	Si II	$12.98_{(0.06)}$	8	2.086 808	0	$13.3_{(0.2)}$	Si II	$14.37_{(0.01)}$
				O I	$13.75_{(0.04)}$					O I	>15.81
				C II	$13.44_{(0.03)}$					C II	>15.64
2	2.085 297	−147	$5.2_{(0.6)}$	Si II	$13.27_{(0.05)}$					Al II	$12.66_{(0.01)}$
				O I	>14.69					Fe II	$13.91_{(0.02)}$
				C II	>13.70	9	2.087 482	+65	$7.1_{(0.2)}$	Si II	$13.54_{(0.02)}$
				Al II	$11.88_{(0.08)}$					O I	$14.38_{(0.02)}$
				Fe II	$12.81_{(0.08)}$					C II	$14.57_{(0.03)}$
3	2.085 481	−129	$10.4_{(0.5)}$	Si II	$14.02_{(0.02)}$					Al II	$12.27_{(0.02)}$
				O I	>14.99					Fe II	$13.26_{(0.04)}$
				C II	>16.07	10	2.087 682	+85	$6.3_{(0.8)}$	Si II	$12.73_{(0.08)}$
				Al II	$12.81_{(0.02)}$					O I	$13.75_{(0.03)}$
				Fe II	$13.66_{(0.02)}$					C II	$13.65_{(0.02)}$
4	2.085 711	−107	$6.1_{(0.4)}$	Si II	$13.53_{(0.02)}$					Al II	$11.07_{(0.19)}$
				O I	$14.59_{(0.25)}$	11	2.087 973	+113	$5.6_{(0.4)}$	Si II	$12.92_{(0.05)}$
				C II	>14.26					O I	$13.86_{(0.04)}$
				Al II	$12.06_{(0.05)}$					C II	$13.82_{(0.03)}$
				Fe II	$13.28_{(0.03)}$					Al II	$11.61_{(0.07)}$
5	2.085 857	−92	$8.5_{(3.2)}$	Si II	$13.16_{(0.12)}$	12	2.088 111	+127	$6.1_{(0.4)}$	Si II	$13.30_{(0.03)}$
				O I	$14.20_{(0.12)}$					O I	$14.24_{(0.02)}$
				C II	>13.95					C II	$14.32_{(0.21)}$
				Al II	$11.75_{(0.12)}$					Al II	$12.01_{(0.04)}$
6	2.086 125	−66	$10.2_{(0.4)}$	Si II	$14.09_{(0.03)}$					Fe II	$13.13_{(0.05)}$
				O I	>15.36	13	2.088 333	+148	$13.8_{(2.0)}$	Si II	$12.97_{(0.06)}$
				C II	>15.24					O I	$13.75_{(0.05)}$
				Al II	$12.75_{(0.02)}$					C II	$14.03_{(0.10)}$
				Fe II	$13.67_{(0.02)}$					Al II	$11.75_{(0.07)}$
7	2.086 501	−30	$6.0_{(1.3)}$	Si II	$12.81_{(0.07)}$	14	2.088 617	+176	$6.0_{(0.2)}$	Si II	$13.66_{(0.02)}$
				O I	$13.85_{(0.22)}$					O I	$14.69_{(0.04)}$
				C II	$13.33_{(0.18)}$					C II	>14.95
				Al II	$11.36_{(0.11)}$					Al II	$12.48_{(0.02)}$
										Fe II	$13.40_{(0.02)}$
High-ion transitions											
1	2.088 197	+135	$17.5_{(1.8)}$	Si IV	$12.69_{(0.04)}$	2	2.088 584	+173	$10.4_{(1.1)}$	Si IV	$12.58_{(0.04)}$
				C IV	$13.05_{(0.04)}$					C IV	$12.72_{(0.07)}$

*Velocity relative to $z = 2.086\,808$.

Lyα forest. We adopted a relatively large error on N(C II) to take into account possible H I contaminations. We observe eight O I lines in the available spectra, but the bulk of them are heavily blended with Lyα forest absorptions. Only the O I $\lambda\lambda$988,1039 lines allowed us to obtain a significant upper limit on N(O I). The Zn II and Cr II lines are not detected in the spectra, thus we provide only 4σ upper limits. No column density measurement of intermediate-ion transitions was obtained. The Fe III λ1122 line is heavily blended in the Lyα forest, and the Al III lines are not detected, hence only a 4σ upper limit was derived.

Similarly to the sub-DLA system at $z_{\rm abs} = 2.087$ towards Q1444+014, the C IV high-ion transition lines observed in this sub-DLA show a peculiar behaviour. They are shifted by $\sim$80 km s^{-1} redwards of the low-ion transition lines. Although such a velocity difference between low- and high-ion lines is also observed in some DLA absorbers (Ledoux et al. 1998), in this particular case, the low- and the high-ion profiles do *not* overlap at all in velocity space (see Table 7 and Fig. 15). This could suggest that the C IV lines are not associated with the studied sub-DLA system. Under this assumption, it may mean that another metal-line system at $\sim$+80 km s^{-1} is blended with the absorber associated with the low-ion transitions. However, this situation seems unlikely, since we should then observe the absorption lines of higher members of the Lyman series breaking into two components. A weak emission feature is observed at $\sim$40 km s^{-1} in the Ly8 line (see Fig. 14) and it may cast some doubt on the previous statement. However, given the low quality of the data, it is difficult to determine with confidence whether this feature is real or just noise. Indeed, the feature is detected at less than 2σ in the Ly8 line, which is observed less than 15 Å away from the blue edge of the quasar spectrum (the quasar flux cut-off is at $\sim$3835 Å), where the signal-to-noise ratio is very low (only $\sim$5 FWHM). Therefore, with the available data we assume that the analysis of this absorption-line system presented here is correct. However, we advise the reader that higher S/N ratio spectra in the blue are required to determine whether the observed emission feature in the Ly8 line is real or not, since it will then imply a revision of the H I column density measurement in this absorber. If in the end this system is not a sub-DLA, it has no impact on our unbiased sample of sub-DLAs and on the statistical work presented in Paper II, since due to the non-observation of the Lyα line in this system, it was excluded from the sample of sub-DLAs used for the statistical work (see Section 2.3).

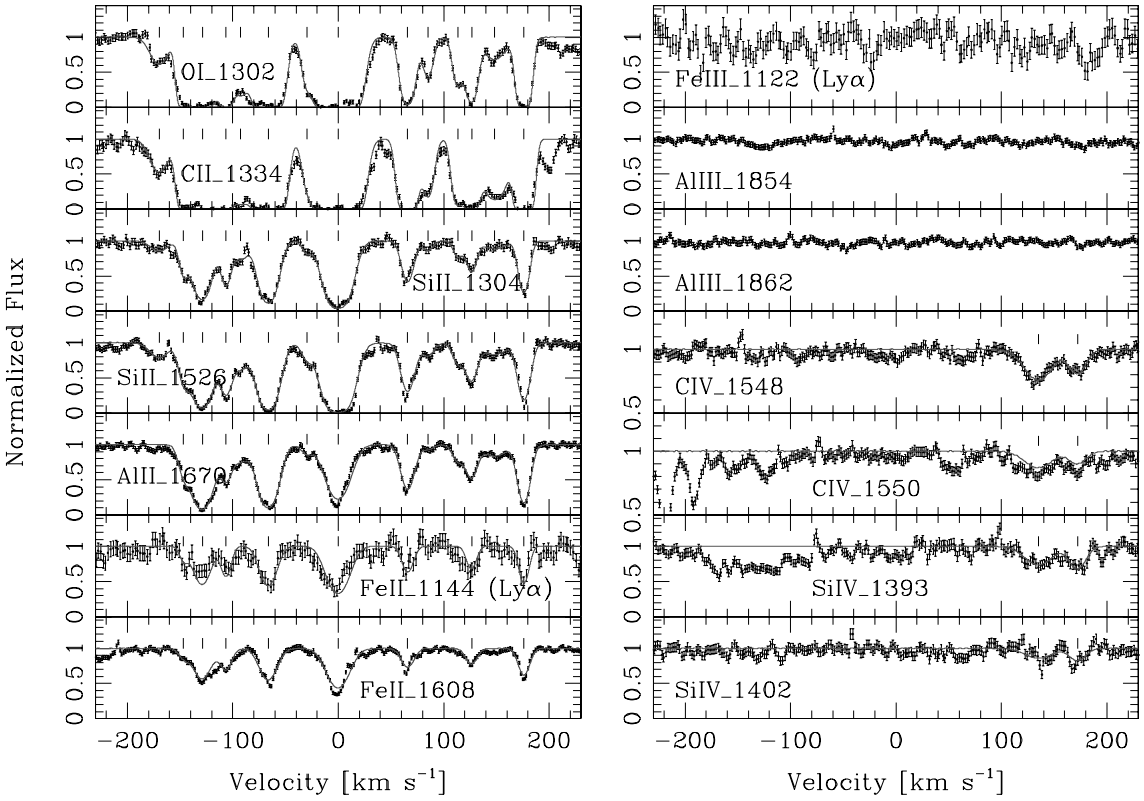

Figure 11. Same as in Fig. 5 for the sub-DLA towards Q1444+014. The zero velocity is fixed at $z = 2.086\,808$. The vertical bars mark the positions of the fitted velocity components (see Table 5).

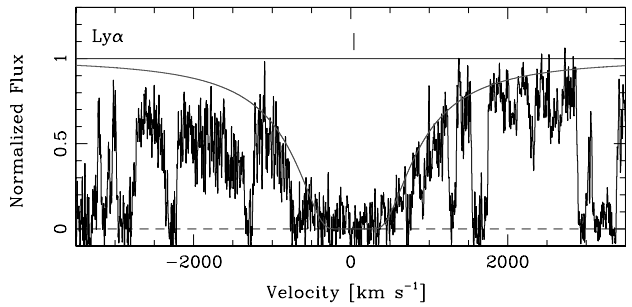

Figure 12. Normalized UVES spectrum of Q1451+123 showing the Lyα profile with the Voigt profile fit of the borderline case between the DLA and sub-DLA systems. The zero velocity is fixed at $z = 2.254\,710$. The vertical bar corresponds to the velocity centroid used for the best fit, $z = 2.255\,151$. The measured H I column density is log N(H I)=20.30 ± 0.15.

3.7 Q1511+090, $z_{\rm sub-DLA} = 2.088$

The absorption-line systems towards this quasar were first analysed by Sargent, Steidel & Boksenberg (1988). However, the sub-DLA system at $z_{\rm abs} = 2.088$ has never been previously studied, nor reported in the literature. It has been identified thanks to the Lyα absorption line, the only hydrogen line observed in the available spectra. The blue damping wing of the Lyα line is blended with other H I clouds, and only the outer parts of the blue wing are visible. The red damping wing is in contrast relatively well constrained and can be used to determine the hydrogen column density of the system (see Fig. 16). By fixing the b-value at 20 km s^{-1} and by leaving the redshift as a free parameter, we obtained a H I column

Table 6. Component structure of the $z_{\rm abs} = 2.255$ borderline case between the DLA and sub-DLA systems towards Q1451+123.

No	$z_{\rm abs}$	$v^*_{\rm rel}$ (km s^{-1})	$b(\sigma_b)$ (km s^{-1})	Ion	log $N(\sigma_{\log N})$ (cm^{-2})
Low-ion transitions					
1	2.254 420	−27	$11.5_{(0.6)}$	Si II	>14.59
				Fe II	$13.68_{(0.02)}$
				Ni II	<13.20
				Cr II	$12.33_{(0.15)}$
2	2.254 584	−12	$5.0_{(2.1)}$	Si II	>14.56
				Fe II	$13.73_{(0.08)}$
				Ni II	<12.77
				Zn II	$11.49_{(0.15)}$
				Cr II	$12.37_{(0.13)}$
3	2.254 710	0	$2.8_{(1.4)}$	Si II	>15.31
				Fe II	$13.84_{(0.12)}$
				Ni II	<13.09
				Zn II	$11.60_{(0.08)}$
				Cr II	$12.48_{(0.15)}$
4	2.255 047	+31	$15.4_{(0.4)}$	Si II	$13.95_{(0.08)}$
				Fe II	$13.56_{(0.01)}$
5	2.255 725	+93	$7.2_{(0.7)}$	Si II	$12.56_{(0.21)}$
				Fe II	$12.86_{(0.03)}$
Intermediate-ion transitions					
1	2.254 395	−29	$18.2_{(3.5)}$	Al III	$12.29_{(0.07)}$
2	2.254 675	−3	$5.1_{(0.6)}$	Al III	$12.48_{(0.03)}$

*Velocity relative to $z = 2.254\,710$.

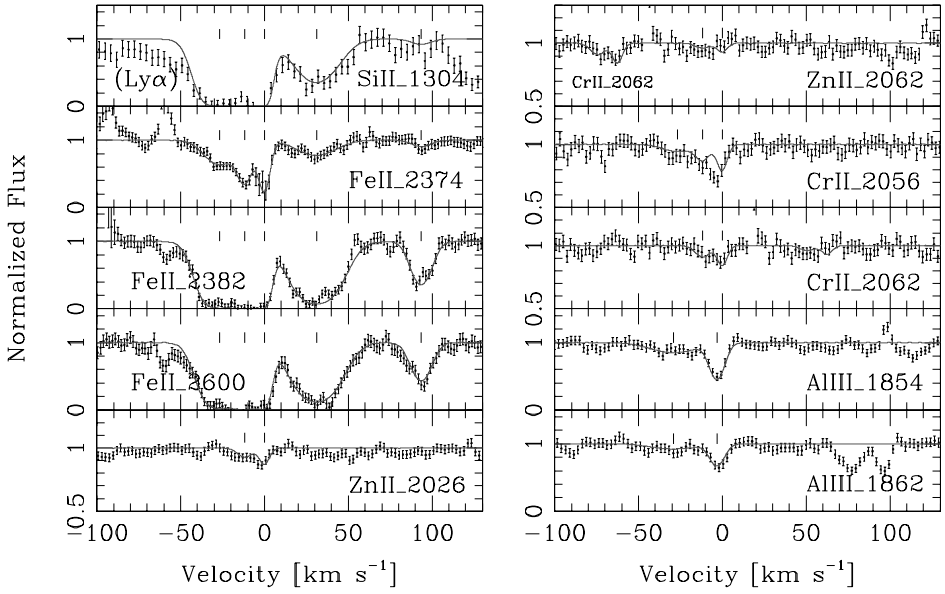

Figure 13. Same as in Fig. 5 for the borderline case between the DLA and sub-DLA systems towards Q1451+123. The zero velocity is fixed at $z = 2.254\,710$. The vertical bars mark the positions of the fitted velocity components (see Table 6).

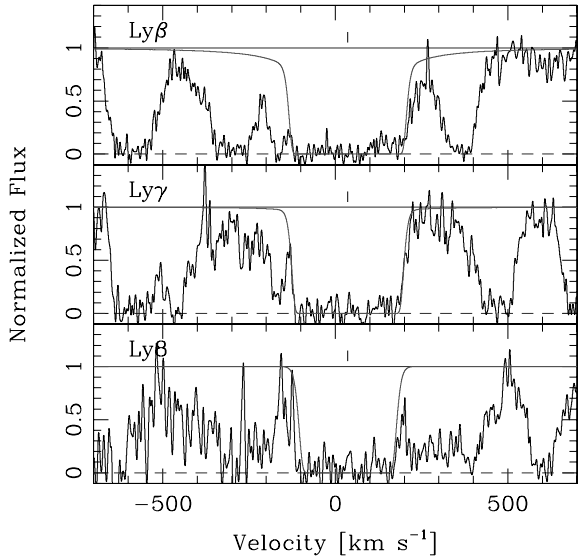

Figure 14. Normalized UVES spectrum of Q1451+123 showing the sub-DLA Lyβ, Lyγ and Ly8 profiles with the Voigt profile fits. The zero velocity is fixed at $z = 3.171\,109$. The vertical bar corresponds to the velocity centroid used for the best fit, $z = 3.171\,606$. The measured H I column density is log N(H I)=19.70 ± 0.15.

Table 7. Component structure of the $z_{\rm abs} = 3.171$ sub-DLA system towards Q1451+123.

No	$z_{\rm abs}$	$v^*_{\rm rel}$ (km s^{-1})	$b(\sigma_b)$ (km s^{-1})	Ion	log $N(\sigma_{\log N})$ (cm^{-2})
Low-ion transitions					
1	3.170 795	−23	$8.9_{(1.3)}$	Si II	$13.29_{(0.04)}$
				O I	<14.46
				C II	$13.96_{(0.18)}$
				Al II	$11.97_{(0.03)}$
				Fe II	$12.99_{(0.07)}$
2	3.171 109	0	$9.2_{(0.9)}$	Si II	$13.38_{(0.03)}$
				O I	<14.53
				C II	$14.04_{(0.21)}$
				Al II	$12.04_{(0.03)}$
				Fe II	$13.06_{(0.06)}$
High-ion transitions					
1	3.172 149	+75	$14.3_{(3.0)}$	C IV	$13.39_{(0.14)}$
2	3.172 427	+95	$12.4_{(2.4)}$	C IV	$12.78_{(0.07)}$

*Velocity relative to $z = 3.171\,109$.

density of log N(H I)=19.47 ± 0.10 as the best-fitting solution for the Lyα line. The derived redshift at $z = 2.08833$ is located between components 4 and 5 of the low-ion transition profiles.

Table 8 and Fig. 17 present the velocity structure of this sub-DLA system. The low-ion transition lines are well described by eight components extended over a large velocity interval of ∼240 km s^{-1}. All the metal lines with rest wavelengths up to $\lambda_{\rm rest} =$ 1527 Å are located in the Lyα forest, thus the column density determinations of a large number of elements have to be done with caution. We obtained the column density measurements of Si II, Al II and Fe II. The access to the strong Fe II λλ2344,2382,2600 transitions allowed us to measure accurately N(Fe II) of this rather low-metallicity system, [Fe/H]=−1.71 ± 0.10. The O I λ1302 line is blended with Lyα forest lines, thus no reliable column density measurement can be determined, and we choose to consider the derived value as an upper limit. The case of the C II λ1334 line is even more difficult. The saturation of the line together with the strong blending, makes the estimation of the column density of C^+ impossible. The Al^{2+} and Fe^{2+} intermediate-ion transition lines are not detected, hence we provide only 4σ upper limits on N(Al III) and N(Fe III) – the Fe III λ1122 line is located in the Lyα forest, but the spectral region where the strongest components of the Fe III line should be detected is free from H I blendings, and thus we can derive a reliable 4σ upper limit on N(Fe III). The observed high-ion transition lines, the C IV and Si IV doublets, are all heavily blended with Lyα forest lines preventing us from measuring their column densities.

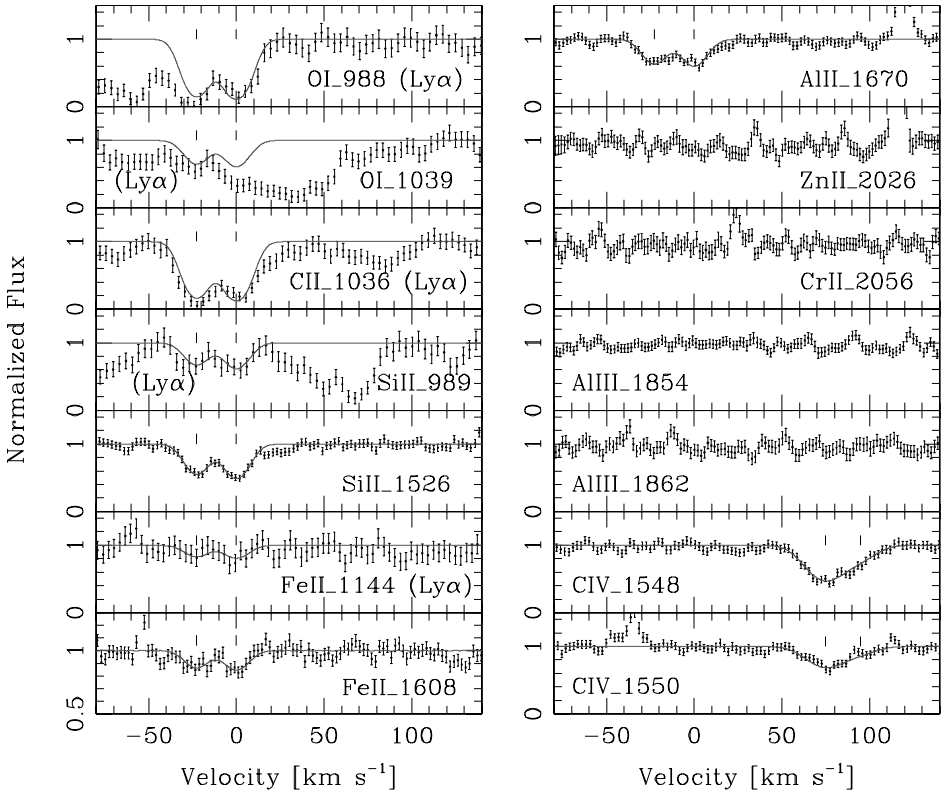

Figure 15. Same as in Fig. 5 for the sub-DLA towards Q1451+123. The zero velocity is fixed at $z = 3.171\,109$. The vertical bars mark the positions of the fitted velocity components (see Table 7).

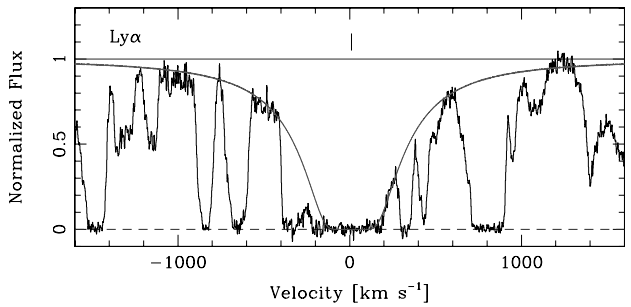

Figure 16. Normalized UVES spectrum of Q1511+090 showing the sub-DLA Lyα profile with the Voigt profile fit. The zero velocity is fixed at $z = 2.088\,223$. The vertical bar corresponds to the velocity centroid used for the best fit, $z = 2.088\,330$. The measured H I column density is log N(H I)=19.47 $\pm$ 0.10.

3.8 Q2059−360, $z_{\rm sub-DLA} = 2.507$

The quasar Q2059−360 was discovered by Warren, Hewett & Osmer (1991), and it has been studied for its intervening DLA system at $z_{\rm abs} = 3.083$. The molecular content of this DLA has been analysed by Petitjean et al. (2000). We have found in the spectra of Q2059−360 an additional high hydrogen column density absorption-line system, a sub-DLA at $z_{\rm abs} = 2.507$. It has been identified thanks to the Lyα absorption line which shows well-defined damping wings (see Fig. 18). No other hydrogen line is observed in the available spectra. The fit of the Lyα line was performed by fixing the b-value at 20 km s^{-1} and the redshift at the redshift of the strongest component of the low-ion transition lines, component 1. The derived H I column density is log N(H I)=20.21 $\pm$ 0.10.

The low-ion transition profiles are characterized by a simple velocity structure composed of two components (see Table 9 and Fig. 19). In the weaker lines, only the strongest component at $v = 0$ is observed. We obtained an accurate Fe^+ column density measurement thanks to the numerous observed Fe II lines at $\lambda_{\rm rest}$ = 2344, 2374, 2382, 2586 and 2600 Å, and despite the fact that the reddest parts of the available spectra at $\lambda > 8000$ Å are noisy with a S/N ratio per pixel lower than 10. The observed Si II λ1304, O I λ1302 and C II λ1334 lines are all located in the Lyα forest. Large errors have been adopted on their column density measurements to take into account possible Lyα contaminations. In the case of Si^+, we could constrain the column density of the strongest component with the Si II λ1808 line located outside the Lyα forest. However, the derived O^0 and C^+ column density measurements might be considered as borderline cases between values and limits. We also obtained a column density measurement of N^0 from the N I $\lambda\lambda$1200.223,1200.710 lines, with the N I λ1199.550 line being blended. This measurement is marginal, since the detected N I lines are extremely weak, at the limit of the noise level. The Zn II and Cr II lines are not detected despite the relatively high H I column density of the system, thus we provide 4σ upper limits. We also give the 4σ upper limit on the Al^{2+} intermediate-ion transition column density, the Al III lines not being detected. No high-ion transition column density has been measured, since the Si IV lines are heavily blended with Lyα forest absorptions and the C IV lines are not covered in the available spectra.

Table 8. Component structure of the $z_{\rm abs} = 2.087$ sub-DLA system towards Q1511+090.

No	$z_{\rm abs}$	$v^*_{\rm rel}$ (km s^{-1})	$b(\sigma_b)$ (km s^{-1})	Ion	log $N(\sigma_{\log N})$ (cm^{-2})
Low-ion transitions					
1	2.086 977	−121	$9.1_{(0.3)}$	Si II	$12.84_{(0.01)}$
				O I	$13.14_{(0.03)}$
				Al II	$11.66_{(0.18)}$
				Fe II	$12.14_{(0.02)}$
2	2.087 631	−57	$30.0_{(3.8)}$	Si II	$12.87_{(0.02)}$
				O I	<13.81
				Al II	$12.29_{(0.13)}$
				Fe II	$12.12_{(0.03)}$
3	2.087 833	−38	$11.4_{(1.0)}$	Si II	$12.70_{(0.03)}$
				O I	<13.06
				Al II	$11.81_{(0.14)}$
				Fe II	$12.05_{(0.04)}$
4	2.088 223	0	$13.5_{(0.8)}$	Si II	$12.98_{(0.02)}$
				O I	<13.94
				Al II	$11.78_{(0.14)}$
				Fe II	$12.19_{(0.03)}$
5	2.088 643	+41	$11.1_{(1.0)}$	Si II	$12.80_{(0.01)}$
				O I	<14.23
				Al II	$11.76_{(0.16)}$
				Fe II	$12.12_{(0.03)}$
6	2.088 861	+62	$5.6_{(0.3)}$	Si II	$13.17_{(0.01)}$
				O I	<14.52
				Al II	$11.99_{(0.13)}$
				Fe II	$12.37_{(0.02)}$
7	2.089 054	+81	$9.7_{(0.5)}$	Si II	$13.47_{(0.18)}$
				O I	<14.93
				Al II	$12.24_{(0.13)}$
				Fe II	$12.73_{(0.03)}$
8	2.089 310	+106	$17.6_{(1.4)}$	Si II	$13.50_{(0.15)}$
				O I	<14.68
				Al II	$12.22_{(0.13)}$
				Fe II	$12.58_{(0.04)}$

*Velocity relative to $z = 2.088\,223$.

3.9 Q2116−358, $z_{\rm sub-DLA} = 1.996$

The quasar Q2116−358 was discovered by Adam (1985). Its intervening absorption metal-line system at $z_{\rm abs} = 1.996$ has previously been reported by Lanzetta, Wolfe & Turnshek (1987), Wampler, Bergeron & Petitjean (1993) and Møller, Jakobsen & Perryman (1994), and it has even been targeted in an imaging programme by Warren et al. (2001). In this paper we provide a new complete abundance analysis of this system using the UVES high-resolution spectra.

Only the hydrogen Lyα line is observed in the available data. It shows well-defined damping wings, which allowed an accurate measurement of the H I column density of the system. We obtained a value of log N(H I)=20.06 ± 0.10, lower by ∼0.1 dex than the value reported by Møller et al. (1994), and which indicates that the absorber is a sub-DLA system. Fig. 20 shows the best-fitting solution of the Lyα line. The presence of an asymmetry in the profiles of the blue and red damping wings made it necessary to include, besides the contribution of the sub-DLA system, a second low column density absorption system bluewards of the sub-DLA in order to obtain a good fit of both wings of the Lyα line. During the fitting procedure, the redshift and the b-value of the sub-DLA system were fixed at the redshift of component 6 of the low-ion transition lines and at 20 km s^{-1}, respectively, and the redshift and the b-value of the second absorber were left as free parameters. We obtained the best-fitting solution with the second absorption-line system at $z = 1.992\,317$ shifted by approximately −391 km s^{-1} from the sub-DLA system and with a H I column density of log N(H I)=14.59 ± 0.10.

Metal lines from a wide range of ionization species are present in this sub-DLA system. Fig. 21 shows the low-, intermediate- and high-ion transition line profiles, and their velocity structures are described in Table 10. The low-ion transition lines are characterized by a relatively complex velocity structure of 11 components spread over ∼220 km s^{-1}. Only the strongest components, components 3–6, are observed in the weak metal lines, such as the Ni II, Cr II and Zn II lines. We obtained the column density measurements of Si^+, Ni^+, Cr^+, Zn^+ and Fe^+. Many components of the O I λ1302 and Al II λ1670 lines are strongly saturated, while the weaker components are well matched by the model parameters defined from the Si II and Fe II lines. Since no reliable value of the total column density of O^0 and Al^+ can be deduced, we provide only lower limits. We also detect the S II λλ1250,1259 lines. However, since they are blended with Lyα forest absorptions, we preferred to consider the measured S^+ column density as an upper limit.

Relatively strong Al III lines are observed in this sub-DLA system (see Fig. 21). These intermediate-ion transition lines show profiles that are very similar to the low-ion profiles, but need to be fitted with slightly different model parameters given in Table 10. The Fe III λ1122 intermediate-ion line is also observed. Nevertheless, it is located in the Lyα forest and is blended, therefore we provide only an upper limit on its column density. The observed high-ion transition lines are very strong and show a complex velocity structure composed of 10 components. They extend over a wider velocity range of ∼290 km s^{-1} than the low-ion profiles (see Fig. 21). We obtained the column density measurement of Si IV and a lower limit on N(C IV) − two components of the C IV doublet are heavily saturated.

3.10 PSS J2155+1358

High signal-to-noise ratio, 5- Å resolution (FWHM) spectra of this $z_{\rm em} > 4$ quasar have been obtained by Péroux et al. (2001). They identified a high H I column density DLA system at $z_{\rm abs} = 3.316$. The metallicity of this DLA system was first reported by Dessauges-Zavadsky et al. (2001b). Here we present the chemical analysis of three newly identified sub-DLA systems at $z_{\rm abs} = 3.142$, 3.565 and 4.212 towards this quasar.

3.10.1 $z_{\rm sub-DLA} = 3.142$

This sub-DLA system has been identified thanks to the Lyα absorption line. No other hydrogen lines are observed in this sub-DLA, since they are beyond the quasar flux cut-off. Its H I column density is thus poorly constrained, all the more so since the Lyα line lies in the far blue end of the quasar spectrum. As a result of the high number of H I absorptions present in these spectral regions, the Lyα damping wings are strongly blended and the continuum placement is uncertain. Fig. 22 shows the best-fitting solution obtained by fixing the b-value at 20 km s^{-1} and the redshift at the redshift of the strongest component, component 1, of the low-ion transition lines. We derived a hydrogen column density of log N(H I) = 19.94 ± 0.10.

Few metal lines were detected in this sub-DLA system, mainly because all of the lines with rest wavelengths below 1543 Å are located in the Lyα forest. The velocity structure of the low-ion transition lines was deduced from the Si II, O I, C II, Al II and Fe II lines,

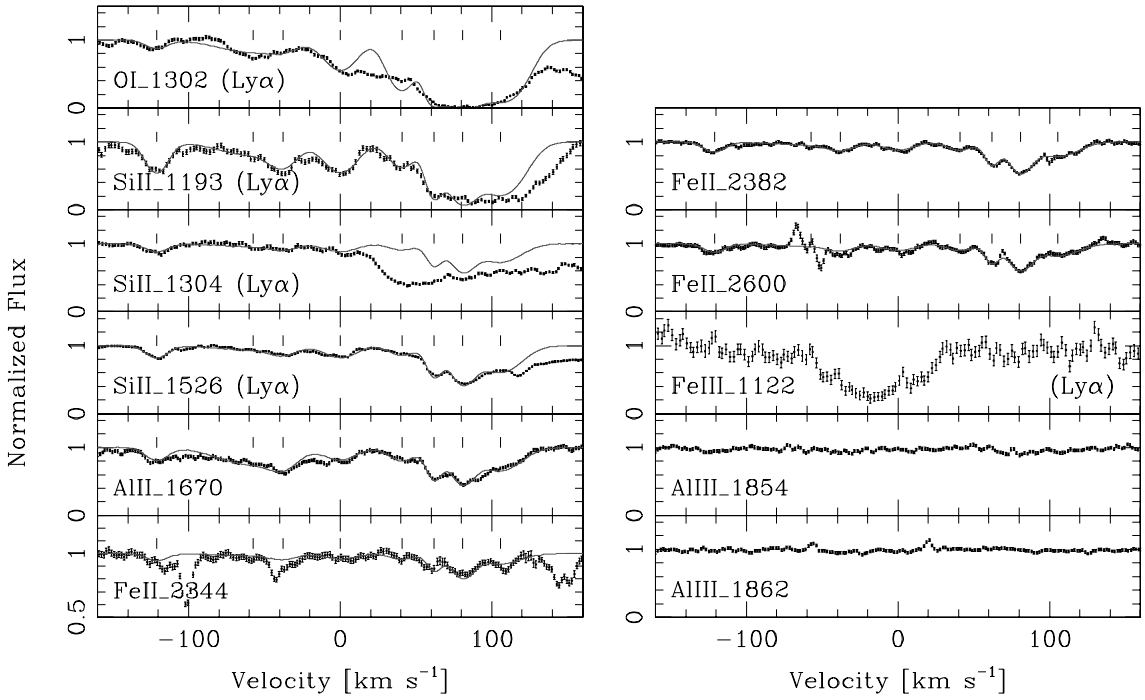

Figure 17. Same as in Fig. 5 for the sub-DLA towards Q1511+090. The zero velocity is fixed at $z = 2.088\,223$. The vertical bars mark the positions of the fitted velocity components (see Table 8).

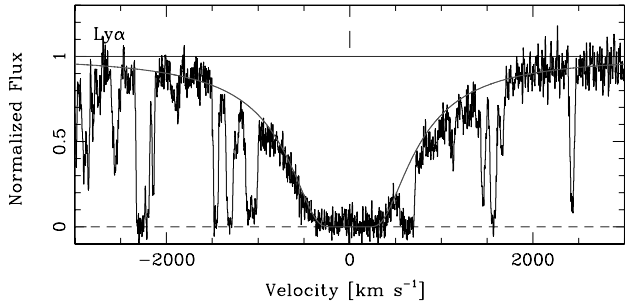

Figure 18. Normalized UVES spectrum of Q2059−360 showing the sub-DLA Lyα profile with the Voigt profile fit. The zero velocity is fixed at $z = 2.507\,341$. The vertical bar corresponds to the velocity centroid of the strongest component of the low-ion transition lines used for the best fit, component 1 at $z = 2.507\,341$. The measured H I column density is log N(H I)=20.21 ± 0.10.

all observed in the Lyα forest apart from the Al II and Fe II lines. It is well described by three components (see Table 11 and Fig. 23). We were able to measure the column density of Si^+ thanks to the detection of three Si II lines at $\lambda_{rest} = 1190$, 1193 and 1304 Å. We obtained the column density measurement of Al^+ from the Al II λ1670 line, the velocity components of which are just not blended with telluric lines, which we identified with the help of the spectrum of a hot, fast rotating star observed on the same night as the quasar. We deduced the Fe^+ column density from the Fe II λ1608 line. The weakness of this Fe II line observed in this case was just above the noise level and is usually almost saturated in the DLA systems, indicating that the metallicity in this sub-DLA is low, [Fe/H]=−2.21 ± 0.21. To be conservative, we preferred to consider the derived O^0 and C^+ column density measurements as upper limits due to the possible blends with Lyα forest lines. No intermediate-ion and high-ion transitions are observed in this sub-DLA system. We provide an upper limit on the Al^{2+} column density obtained from the fit of the very weak feature observed in the Al III λ1854 line at the redshift of the strongest component of the low-ion line profiles.

Table 9. Component structure of the $z_{abs} = 2.507$ sub-DLA system towards Q2059−360.

No	z_{abs}	v^*_{rel} (km s^{-1})	$b(\sigma_b)$ (km s^{-1})	Ion	log $N(\sigma_{\log N})$ (cm^{-2})
Low-ion transitions					
1	2.507 341	0	$4.9_{(0.2)}$	Si II	$13.66_{(0.08)}$
				O I	$15.52_{(0.21)}$
				C II	$14.82_{(0.21)}$
				N I	$12.66_{(0.18)}$
				Fe II	$13.41_{(0.03)}$
2	2.507 535	+17	$5.3_{(0.8)}$	Si II	$12.91_{(0.25)}$
				O I	$14.11_{(0.13)}$
				C II	$13.87_{(0.15)}$
				Fe II	$12.59_{(0.04)}$

*Velocity relative to $z = 2.507\,341$.

3.10.2 $z_{sub-DLA} = 3.565$

This sub-DLA system was also identified thanks to the Lyα absorption line. No other hydrogen line is observed in the available spectra. Given the high redshift of the quasar PSS J2155+1358, the Lyα forest shows many absorptions, and thus it is not surprising that the damping wings of the Lyα line are strongly blended. We made several fitting tests to find the best-fitting solution of the Lyα line. The first test was performed by fixing in the fitting procedure the b-value at 20 km s^{-1} and by leaving the redshift as a free parameter. We obtained a good fit with log N(H I)=19.62 ± 0.15, but it was not a satisfactory solution, since the deduced redshift was shifted by approximately 73 km s^{-1} bluewards of the redshift of the single component observed in the low-ion transition lines. The second and

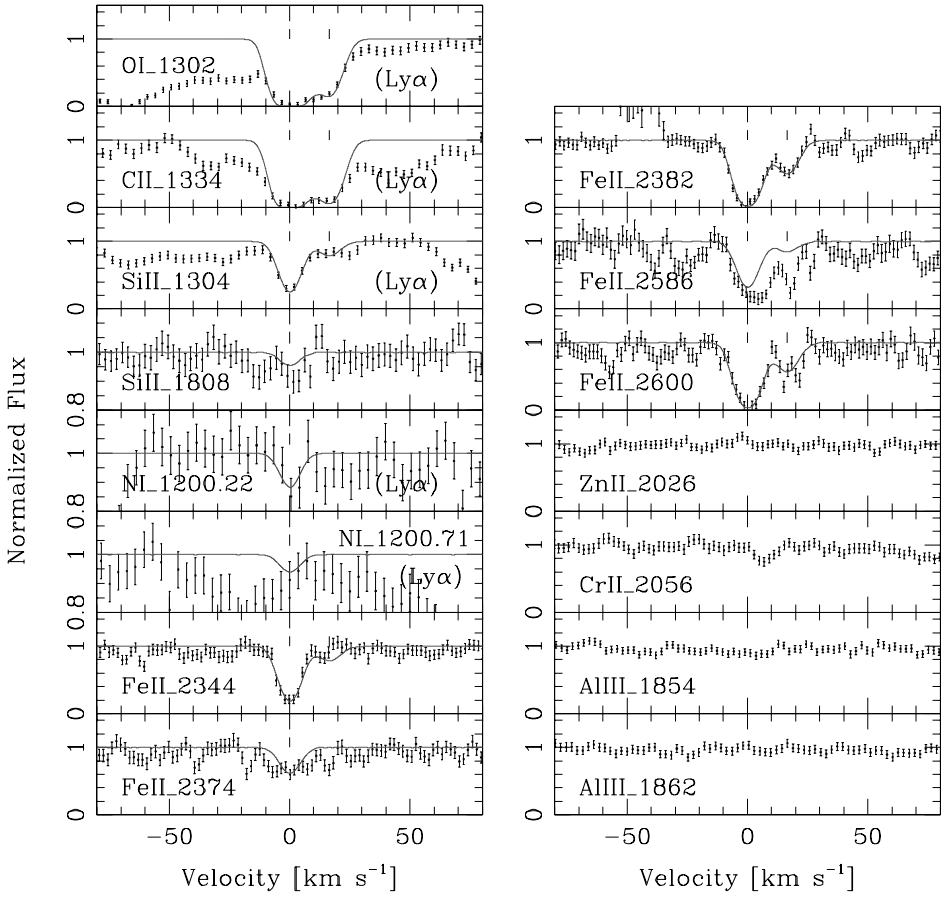

Figure 19. Same as in Fig. 5 for the sub-DLA towards Q2059−360. The zero velocity is fixed at $z = 2.507\,341$. The vertical bars mark the positions of the fitted velocity components (see Table 9).

adopted test was made by fixing both the *b*-value at 20 km s^{-1} and the redshift at the redshift of the single component of the low-ion lines. We obtained the fit shown in Fig. 24. However, in this case, to fill the whole observed Lyα absorption profile, we had to include, besides the sub-DLA contribution, a second low H I column density absorption system bluewards of the sub-DLA system. In the fitting procedure, the *b*-value and the redshift of this second absorber were left as free parameters. We obtained the best-fitting solution with the second absorption-line system located at $z = 3.561\,814$, i.e. shifted by approximately -228 km s^{-1} from the sub-DLA system, and with a H I column density of $\log N(\mathrm{H\,I}) = 16.46 \pm 0.15$. The derived hydrogen column density of the sub-DLA is $\log N(\mathrm{H\,I})$=19.37 $\pm$ 0.15.

As mentioned above, a very simple velocity structure with a single component is observed in the low-ion line profiles (see Fig. 25 and Table 12). We obtained the column density measurements of Si^+, C^+ and Al^+. N(Si II) was deduced from four Si II lines at $\lambda_{\rm rest} = 1190$, 1260, 1304 and 1526 Å. N(C II) is a marginal measurement, since the C II λ1334 line is located in the Lyα forest, where blends are not excluded. Finally, N(Al II) was obtained from the Al II λ1670 line found in a spectral region heavily contaminated by telluric lines. The spectrum of a hot, fast rotating star observed the same night as the quasar allowed us to identify the telluric lines and to show that the Al^+ line is not blended, but the uncertainty relative to the continuum placement in this region remains. We therefore adopted a relatively large error on the measured N(Al II). Only the Fe II λ1608 line is available to measure the Fe^+ column density, and no absorption

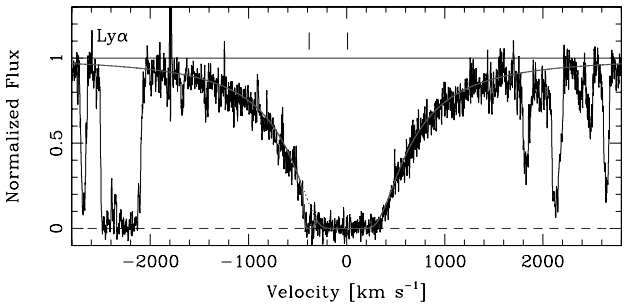

Figure 20. Normalized UVES spectrum of Q2116−358 showing the sub-DLA Lyα profile with the Voigt profile fit. The zero velocity is fixed at $z = 1.996\,119$. The vertical bars correspond from right to left to the velocity centroids of component 6 of the low-ion transition lines at $z = 1.996\,224$ and 1.992 317 used for the best fit, belonging to the sub-DLA system and an additional absorber, respectively. The dotted line corresponds to the fit with the sub-DLA only. The measured H I column density of the sub-DLA is $\log N(\mathrm{H\,I})$=20.06 $\pm$ 0.10.

feature at the redshift of the single component observed in the other low-ion transition lines is detected. We thus provide only a 4σ upper limit on the Fe^+ column density, which indicates that the metallicity is very low in this sub-DLA system, lower than [Fe/H] < -2.31.

The column density measurements of the intermediate-ion transitions are crucial to constraining the ionization parameters in this sub-DLA system, which has among the lowest H I column density

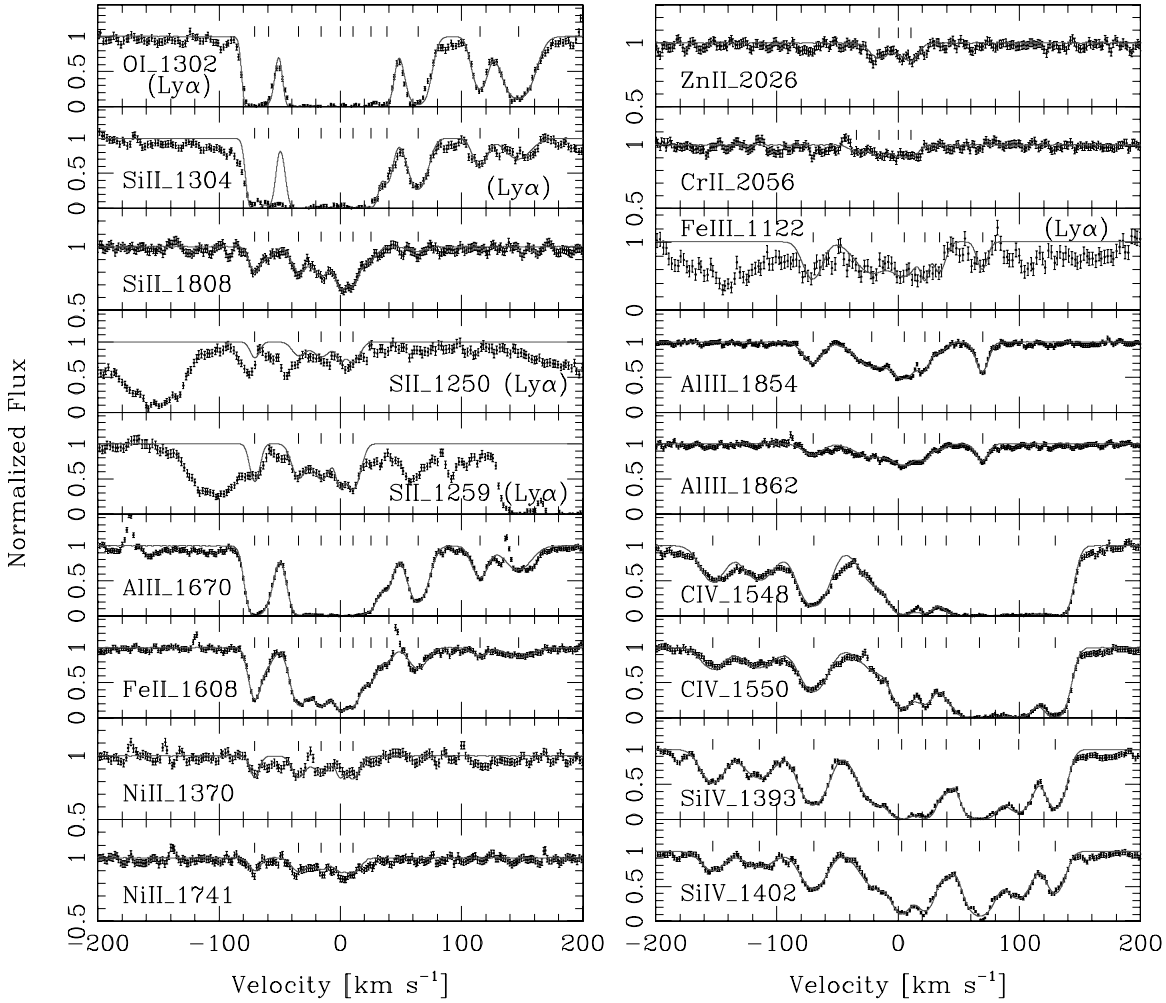

Figure 21. Same as in Fig. 5 for the sub-DLA towards Q2116−358. The zero velocity is fixed at $z = 1.996\,119$. The vertical bars mark the positions of the fitted velocity components (see Table 10).

in our sample. We detect only the Al III λ1862 line. The Al III λ1854 line is blended with emission lines from badly subtracted cosmic rays in the reduction procedure – only two exposures were obtained for this quasar. The observed Al III λ1862 line shows a single component at exactly the redshift of the component of the low-ion transition lines (see Fig. 25). Assuming that this feature is real and is Al^{2+}, we obtained a column density measurement using the same fitting parameters as those deduced for the low-ion lines. We also derived an upper limit on $N(Fe^{2+})$ from the Fe III λ1122 line located in the Lyα forest. In addition, we detect the strong C IV and Si IV high-ion transition lines. They show a much more complex velocity structure, composed of six components and spread over ∼120 km s^{-1} than the low-ion lines (see Fig. 25 and Table 12).

3.10.3 $z_{\rm sub-DLA} = 4.212$

This high-redshift sub-DLA system was easily identified with the Lyα absorption line that shows a very well-defined red damping wing, the blue wing being partially blended with Lyα forest lines. The Lyman series is observed down to Ly13 in this sub-DLA and allowed us to obtain a very accurate H I column density measurement by fitting simultaneously the Lyα line and the unblended Lyϵ and Ly11 lines (see Fig. 26). In the fitting procedure, we left the redshift as a free parameter and we fixed the *b*-value at 23 km s^{-1}. The best-fitting solution was obtained with $z = 4.212\,442$, which fell just between the two components observed in the low-ion transition lines, and with a H I column density of log N(H I)=19.61 ± 0.10. However, it can be seen that the sub-DLA system is not sufficient to fill the whole observed Lyα absorption, so contributions from additional Lyα clouds have to be included.

Given the high signal-to-noise ratio of the available spectra in the regions where we detect the low-ion transition lines and the fact that they show a simple velocity structure composed of two well-separated components (see Fig. 27 and Table 13), we obtained very accurate column density measurements of O^0, C^+, Si^+ and Al^+. Two Fe II lines at $\lambda_{\rm rest} = 1144$ and 1608 Å are observed in the available spectra. A very weak feature is detected in the Fe II λ1144 line at the redshift of component 1. However, the second component is partially blended with an emission line from badly subtracted cosmic rays in the reduction procedure – a single exposure was obtained for this quasar in the blue. No absorption feature is observed in the Fe II λ1608 lines, moreover the second component is blended with a badly subtracted strong sky line. We thus obtained only a marginal measurement of the Fe^+ column density, on which we adopted a large error. The weakness of these Fe II lines indicates

Table 10. Component structure of the $z_{\rm abs} = 1.996$ sub-DLA system towards Q2116−358.

No	$z_{\rm abs}$	$v^*_{\rm rel}$ (km s^{-1})	$b(\sigma_b)$ (km s^{-1})	Ion	log $N(\sigma_{\log N})$ (cm^{-2})	No	$z_{\rm abs}$	$v^*_{\rm rel}$ (km s^{-1})	$b(\sigma_b)$ (km s^{-1})	Ion	log $N(\sigma_{\log N})$ (cm^{-2})
Low-ion transitions											
1	1.995 416	−70	$5.0_{(0.8)}$	Si II	$14.39_{(0.07)}$	6	1.996 224	+10	$7.5_{(2.6)}$	Si II	$14.71_{(0.14)}$
				O I	>15.69					O I	>16.00
				S II	<14.12					S II	<14.42
				Al II	$13.29_{(0.17)}$					Al II	>13.36
				Ni II	$12.79_{(0.07)}$					Ni II	$12.99_{(0.05)}$
				Fe II	$13.83_{(0.03)}$					Fe II	$14.05_{(0.13)}$
2	1.995 528	−59	$4.8_{(1.1)}$	Si II	$13.93_{(0.18)}$					Zn II	$11.94_{(0.08)}$
				O I	$14.11_{(0.16)}$					Cr II	$12.42_{(0.11)}$
				Al II	$12.22_{(0.15)}$	7	1.996 373	+25	$5.5_{(1.8)}$	Si II	$14.07_{(0.13)}$
				Fe II	$13.06_{(0.19)}$					O I	>16.00
3	1.995 777	−34	$7.2_{(1.3)}$	Si II	$14.49_{(0.09)}$					Al II	$12.51_{(0.16)}$
				O I	>15.32					Fe II	$13.48_{(0.07)}$
				S II	<14.20	8	1.996 504	+38	$5.6_{(0.8)}$	Si II	$13.50_{(0.05)}$
				Al II	>12.94					O I	$14.20_{(0.15)}$
				Ni II	$12.93_{(0.06)}$					Al II	$12.17_{(0.03)}$
				Fe II	$14.00_{(0.08)}$					Fe II	$13.03_{(0.07)}$
				Cr II	$12.15_{(0.20)}$	9	1.996 759	+64	$9.2_{(0.3)}$	Si II	$13.82_{(0.03)}$
4	1.995 963	−16	$9.5_{(2.4)}$	Si II	$14.66_{(0.12)}$					O I	$14.53_{(0.10)}$
				O I	>16.00					Al II	$12.56_{(0.01)}$
				S II	<14.35					Fe II	$13.41_{(0.04)}$
				Al II	>13.14	10	1.997 269	+115	$7.6_{(0.6)}$	Si II	$13.34_{(0.06)}$
				Ni II	$12.95_{(0.06)}$					O I	$14.05_{(0.03)}$
				Fe II	$14.13_{(0.11)}$					Al II	$12.06_{(0.03)}$
				Zn II	$11.96_{(0.08)}$					Fe II	$12.89_{(0.11)}$
				Cr II	$12.49_{(0.10)}$	11	1.997 586	+147	$13.7_{(0.5)}$	Si II	$13.42_{(0.10)}$
5	1.996 119	0	$4.0_{(2.3)}$	Si II	$14.46_{(0.16)}$					O I	$14.50_{(0.05)}$
				O I	>16.00					Al II	$12.12_{(0.15)}$
				S II	<14.06					Fe II	$13.18_{(0.12)}$
				Al II	>12.96						
				Ni II	$12.61_{(0.10)}$						
				Fe II	$13.88_{(0.10)}$						
				Zn II	$11.23_{(0.24)}$						
				Cr II	$12.07_{(0.20)}$						
Intermediate-ion transitions											
1	1.995 417	−70	$9.8_{(1.0)}$	Al III	$12.38_{(0.03)}$	4	1.996 339	+22	$3.9_{(1.9)}$	Al III	$12.10_{(0.20)}$
				Fe III	<13.93					Fe III	<13.49
2	1.995 903	−22	$17.1_{(2.9)}$	Al III	$12.67_{(0.10)}$	5	1.996 458	+34	$6.4_{(2.5)}$	Al III	$11.87_{(0.11)}$
				Fe III	<14.06					Fe III	<13.62
3	1.996 172	+5	$13.5_{(3.0)}$	Al III	$12.80_{(0.11)}$	6	1.996 814	+69	$5.5_{(0.6)}$	Al III	$12.40_{(0.02)}$
				Fe III	<13.99					Fe III	<13.51
High-ion transitions											
1	1.994 594	−153	$12.5_{(0.7)}$	Si IV	$12.88_{(0.02)}$	6	1.996 344	+22	$9.7_{(0.8)}$	Si IV	$13.53_{(0.03)}$
				C IV	$13.33_{(0.06)}$					C IV	$13.89_{(0.14)}$
2	1.994 974	−115	$16.3_{(1.1)}$	Si IV	$12.90_{(0.02)}$	7	1.996 517	+40	$6.4_{(0.8)}$	Si IV	$12.65_{(0.05)}$
				C IV	$13.41_{(0.04)}$					C IV	$13.48_{(0.16)}$
3	1.995 426	−69	$13.6_{(0.3)}$	Si IV	$13.29_{(0.01)}$	8	1.996 789	+67	$13.7_{(0.5)}$	Si IV	$13.81_{(0.01)}$
				C IV	$13.80_{(0.02)}$					C IV	>15.03
4	1.995 957	−16	$17.4_{(1.3)}$	Si IV	$13.41_{(0.05)}$	9	1.997 112	+99	$13.2_{(0.5)}$	Si IV	$13.44_{(0.01)}$
				C IV	$13.55_{(0.07)}$					C IV	>14.43
5	1.996 150	+3	$9.1_{(0.6)}$	Si IV	$13.52_{(0.04)}$	10	1.997 414	+130	$9.7_{(0.4)}$	Si IV	$13.22_{(0.02)}$
				C IV	$13.92_{(0.13)}$					C IV	$14.33_{(0.12)}$

*Velocity relative to $z = 1.996\,119$.

that the metallicity in this sub-DLA system is very low, [Fe/H]= -2.17 ± 0.25.

The Al III intermediate-ion transition lines are covered in the available spectra, but the signal-to-noise ratio is so low in this particular region that no Al^{2+} line is detected, and no reliable 4σ upper limit can be derived. In addition, the Fe III λ1122, Si III λ1206 and C III λ977 lines are all blended with Lyα forest absorptions. Consequently, no intermediate-ion column density measurement was obtained in this sub-DLA system. On the other hand, the Si IV high-ion transition lines are observed (the C IV lines are outside the available spectral coverage). Again they show a different velocity structure from the low-ion line profiles, but are in this case extended over a similar velocity range (see Fig. 27 and Table 13).

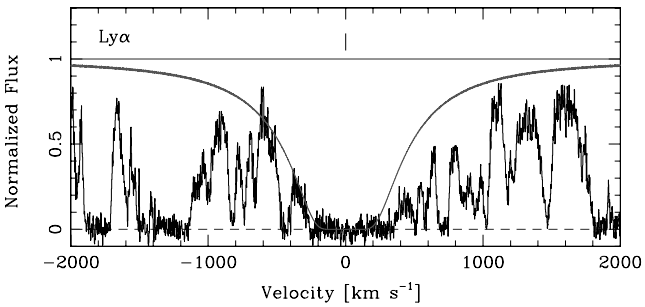

Figure 22. Normalized UVES spectrum of PSS J2155+1358 showing the sub-DLA Lyα profile with the Voigt profile fit. The zero velocity is fixed at $z = 3.141\,998$. The vertical bar corresponds to the velocity centroid of the strongest component of the low-ion transition lines used for the best fit, component 1 at $z = 3.141\,998$. The measured H I column density is log N(H I)=19.94 ± 0.10.

Table 11. Component structure of the $z_{\rm abs} = 3.142$ sub-DLA system towards PSS J2155+1358.

No	$z_{\rm abs}$	$v^*_{\rm rel}$ (km s^{-1})	$b(\sigma_b)$ (km s^{-1})	Ion	log $N(\sigma_{\log N})$ (cm^{-2})
Low- and intermediate-ion transitions					
1	3.141 998	0	$5.7_{(1.0)}$	Si II	$13.36_{(0.06)}$
				O I	<14.22
				C II	$14.05_{(0.20)}$
				Al II	$12.07_{(0.07)}$
				Fe II	$12.77_{(0.20)}$
				Al III	<11.57
2	3.142 313	+23	$14.5_{(2.6)}$	Si II	$12.76_{(0.10)}$
				O I	<13.91
				C II	<13.66
				Al II	$11.50_{(0.18)}$
3	3.142 712	+52	$10.0_{(2.8)}$	Si II	$13.20_{(0.07)}$
				O I	<14.42
				C II	<14.00
				Al II	$11.81_{(0.13)}$
				Fe II	$13.04_{(0.18)}$

*Velocity relative to $z = 3.141\,998$.

3.11 PSS J2344+0342, $z_{\rm sub-DLA} = 3.882$

Péroux et al. (2001) obtained 5-Å resolution (FWHM) spectra of this quasar and identified a DLA system at $z_{\rm abs} = 3.220$. The metallicity of this DLA system was first reported by Dessauges-Zavadsky et al. (2001b). Here we present the chemical analysis of a newly discovered high-redshift sub-DLA system at $z_{\rm abs} = 3.882$. It has been identified thanks to the Lyα absorption line, which shows partially blended damping wings. The Lyβ and Lyγ lines are also observed in this sub-DLA system. The simultaneous fit of both Lyα and Lyβ – the Lyγ line is strongly blended – allowed us to obtain an accurate H I column density measurement.

A first series of fitting tests of the Lyα and Lyβ lines was performed by considering a single absorption-line system. By leaving the redshift and the b-value as free parameters, the best-fitting solution was obtained with a sub-DLA system at $z = 3.884\,697$ – very close to the redshift of the strongest component of the low-ion transition lines, component 9 – and a H I column density of log N(H I)=19.50 ± 0.10. In this solution the red wings of the Lyα and Lyβ lines were well fitted, but the fit clearly shows that another strong absorption-line system is present bluewards of the sub-DLA system (see Fig. 28). We then made a second series of fitting tests by considering this time two absorption-line systems. By leaving in the fitting procedure all the b-values and redshifts as free parameters, we obtained the best-fitting solution with a sub-DLA system characterized by the values described above plus a second strong absorber at $z = 3.881\,604$ shifted by approximately −190 km s^{-1} from the sub-DLA system with a H I column density of log N(H I)=18.94 ± 0.15. This absorption-line system is a borderline case between the Lyman-limit and sub-DLA systems, but we do not include it in the sub-DLA sample.

Table 14 and Fig. 29 present the velocity structure of the sub-DLA system. The low-ion transition lines show a complex velocity structure well described by 11 components. We obtained accurate column density measurements of C^+ and Si^+. The Al II λ1670 line is located in a region strongly contaminated by telluric lines. We identified the telluric lines with the help of the spectrum of a hot, fast rotating star observed on the same night as the quasar, and noted that components 2 and 7 are blended. We adopted a large error on the deduced $N(Al^+)$ to take into account the contributions of these blends. Two Fe^+ lines, Fe II λ1144 and λ1608, are observed. However, the Fe II λ1144 line is partially blended with Lyα forest lines, and none of the 11 components is detected in the Fe II λ1608 line. We thus provide a 4σ upper limit on the Fe^+ column density, which indicates that the metallicity in this sub-DLA system is low, lower than [Fe/H] <−1.98. No intermediate-ion transition line is clearly observed. The Fe III λ1122, C III λ977, N II λ1083 and Si III λ1206 lines are strongly blended with Lyα forest lines, and the Al III lines are not detected. We provide a 4σ upper limit on the Al^{2+} column density.

It should be emphasized that the observed low-ion transition line profiles extend over a very large velocity interval of ∼320 km s^{-1}, from −140 to +180 km s^{-1} in velocity space. It implies that the low-ion transition lines overlap over the two identified clustered absorption-line systems – the sub-DLA and the absorber at $z = 3.881\,604$ shifted by only ∼−190 km s^{-1} from the sub-DLA (see above). It may thus be possible that some of the components of the detected low-ion metal lines are associated with this second absorber and not with the sub-DLA system. Two distinct clumps in the low-ion profiles are not yet observed, but the two high H I column density absorption-line systems are so close that it would not be surprising to find that their metal lines are blended. Moreover, the observed high-ion transition lines, C IV and Si IV, are surprisingly confined to a much narrower velocity interval from +25 to +170 km s^{-1} (see Fig. 29 and Table 14). This may suggest that the detected high-ion lines are associated only with the sub-DLA system. If this is the case, the components of the low-ion transition lines belonging to the sub-DLA could be only those that are located in the same velocity interval as the high-ion lines, i.e. components 7–11. Components 1–6 could then be associated with the second absorption-line system. It is difficult to be categorical on the real situation, therefore it would perhaps be more sensible to speak of an interval of values for the column density measurements in this sub-DLA system.

4 IONIZATION CORRECTION STUDY

In the 12 sub-DLA systems and one borderline case between the DLA and sub-DLA systems studied, we obtained ionic column density measurements of low-ion transitions, O^0, C^+, Si^+, N^0, S^+, Mg^+, Al^+, Fe^+, Ni^+, Zn^+ and Cr^+, intermediate-ion transitions, Al^{2+} and Fe^{2+}, and high-ion transitions, C^{3+} and Si^{3+}. To derive the *intrinsic* abundance measurements of the 11 detected elements, it is necessary to take into account both the ionization and dust depletion effects, since we are measuring gas-phase abundances. Depletion

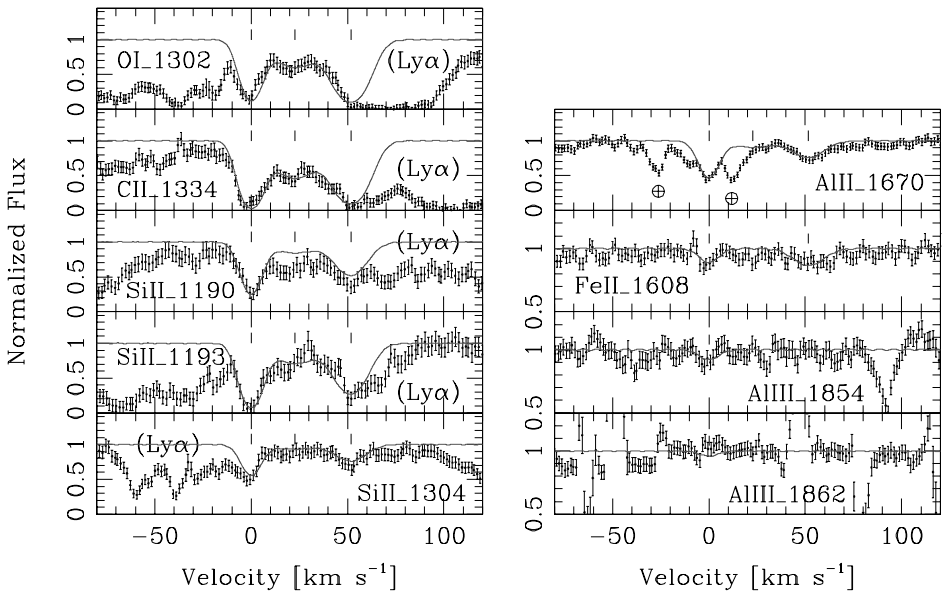

Figure 23. Same as in Fig. 5 for the sub-DLA towards PSS J2155+1358. The zero velocity is fixed at $z = 3.141\,998$. The vertical bars mark the positions of the fitted velocity components (see Table 11).

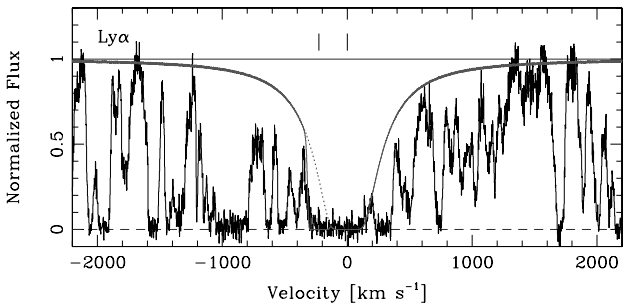

Figure 24. Normalized UVES spectrum of PSS J2155+1358 showing the sub-DLA Lyα profile with the Voigt profile fit. The zero velocity is fixed at $z = 3.565\,272$. The vertical bars correspond from right to left to the velocity centroids of the single component of the low-ion transition lines at $z = 3.56527$ and 3.561 814 used for the best fit, belonging to the sub-DLA system and an additional absorber, respectively. The dotted line corresponds to the fit with the sub-DLA only. The measured H I column density of the sub-DLA is log N(H I)=19.37 ± 0.15.

is discussed in the wider context of Paper II. Here we analyse the ionization status of these systems.

Several authors have investigated the ionization effects in the DLA systems (Viegas 1995; Howk & Sembach 1999; Izotov, Schaerer & Charbonnel 2001; Vladilo et al. 2001; Prochaska et al. 2002). Many of them were motivated by the observations of the intermediate-ion Al^{2+}, a tracer of moderately ionized gas, with the same velocity profiles as the low-ion transitions (Lu et al. 1996b; Prochaska & Wolfe 1999; Prochaska et al. 2001b), which suggest that ionization effects may be present in these systems. Indeed, to explain the similarity of Al III and other low-ionization species line profiles, Howk & Sembach (1999) and Izotov & Thuan (1999) proposed that these lines originate in the same ionized region or in a mix of neutral and ionized clouds, and stressed the importance of abundance corrections for ionization effects. Although the different approaches used to deal with the problem of photoionization in DLAs have led to slightly different conclusions, it is generally accepted that ionization corrections in DLAs are negligible, being below the measurement errors.

In the present study, we are concerned about the ionization corrections for sub-DLAs, i.e. systems with H I column densities lower than those of DLA systems, between $10^{19} < N(\mathrm{H\,I}) < 2 \times 10^{20}$ cm^{-2}. The check of ionization effects in these systems is very important, since their relatively low H I column density implies that some of the gas might be ionized.

4.1 Al^{2+}/Al^{+} as an indicator of the ionization state

In six out of the 12 sub-DLA systems studied we detect the Al III λλ1854,1862 lines, and in four we also detect the Fe III λ1122 line. While neutral and singly ionized species with ionization potential <13.6 eV can be present in the inner parts of H^0 regions, the production of Fe^{2+} and Al^{2+} requires photons with $h\nu > 16.2$ and 18.8 eV, respectively, which cannot so easily penetrate large H I column densities. The analysis of these intermediate-ion transition profiles, however, shows that in all of the sub-DLAs but one at $z_{\rm abs} = 1.838$ towards Q1101−264 (see Section 3.2), their velocity structure is almost indistinguishable from that of low-ion transition profiles, while the high-ion C IV and Si IV transitions have very different velocity profiles. This suggests that the Fe^{2+} and Al^{2+} and regions of neutral H in these systems are physically connected.

The $N(Al^{2+})/N(Al^{+})$ and $N(Fe^{2+})/N(Fe^{+})$ ratios can then be used as indicators of the ionization state. Vladilo et al. (2001) studied the DLA ionization properties from the analysis of the Al^{2+}/Al^{+} ratios in a data sample of 20 DLAs, and found a log $N(Al^{2+})/N(Al^{+})$ versus log $N(H^0)$ anticorrelation. The existence of such an empirical anticorrelation implies that the neutral hydrogen column density is an indirect tracer of the ionization state of the gas. Consequently, if this anticorrelation is further observed in the sub-DLA H I column density range, it would indicate that the sub-DLA systems require higher ionization corrections than absorbers in the DLA H I column density range.

Therefore, we decided to investigate the extension of the different correlations found by Vladilo et al. (2001) in the DLA systems to

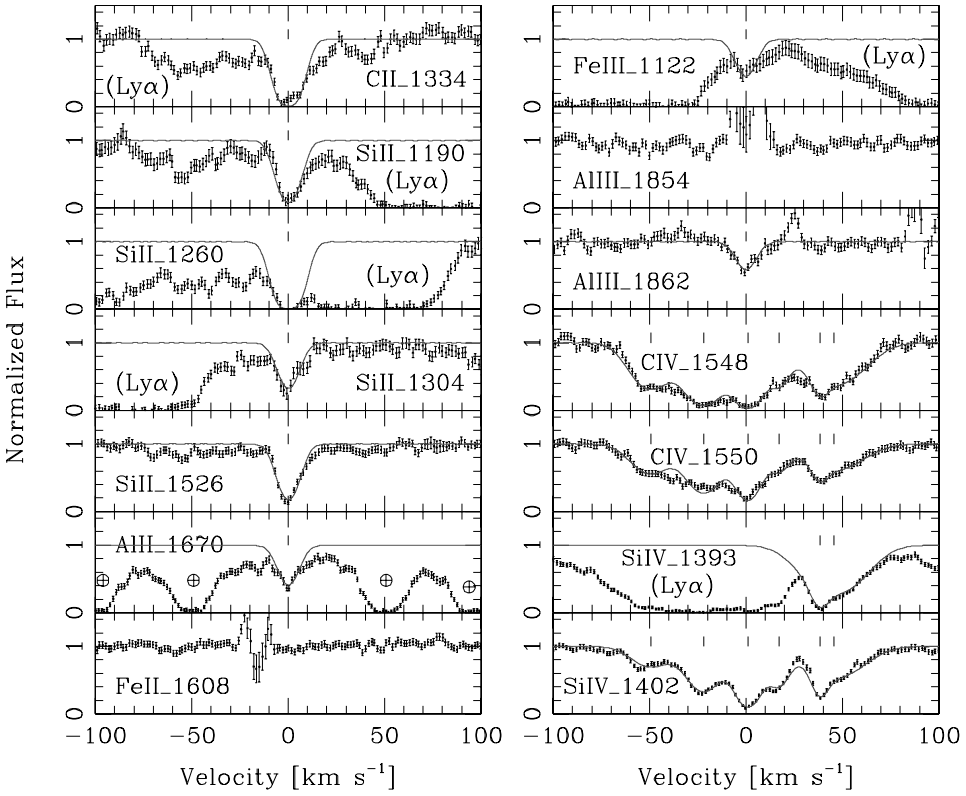

Figure 25. Same as in Fig. 5 for the sub-DLA towards PSS J2155+1358. The zero velocity is fixed at $z = 3.565\,272$. The vertical bars mark the positions of the fitted velocity components (see Table 12).

the H I column density range of the sub-DLA systems. For this purpose we have collected all the DLA and sub-DLA systems found in the literature for which measurements of the Al^+ and/or Al^{2+} column densities exist and were performed on high-resolution spectra obtained at the 8–10 m class telescopes. Most of them were derived from the HIRES/Keck spectra. We have then considered only the systems that show similarities in their Al^{2+} and low-ionization species line profiles, since it is only in this case that the neutral and ionized clouds might be physically related. Finally, we have adopted the values given by Vladilo et al. (2001) for the few cases of Al^+ column density measurements that they have revisited due to previously unquoted saturations or contaminations by telluric lines. The results and the references for the adopted sample of both DLAs and sub-DLAs found in the literature and analysed in this paper are given in Table 15. This table contains the Spearman test correlation coefficients, r, the probabilities of null hypothesis (of no correlation), α, the slopes and the intercepts obtained for the linear regressions of log $N(Si^+)$ versus log $N(Fe^+)$, log $N(Al^+)$ versus log $N(Si^+)$, log $N(Al^+)$ versus log $N(Fe^+)$ and log $N(Al^{2+})/N(Al^+)$ versus log $N(H^0)$.

We confirm the existence of the log $N(Si^+)$ versus log $N(Fe^+)$, log $N(Al^+)$ versus log $N(Si^+)$, and log $N(Al^+)$ versus log $N(Fe^+)$ correlations found by Vladilo et al. (2001) in the DLA systems (see Table 15). These correlations are also satisfied by the sub-DLA systems. We then used the Si^+ (in priority, because the correlation with Al^+ has lower slope and intercept errors) or Fe^+ column densities as a proxy for $N(Al^+)$, when no $N(Al^+)$ measurement was available in the DLA or sub-DLA systems. In four sub-DLAs and several DLAs we took advantage of these correlations Si^+ versus Al^+ and Fe^+ versus Al^+ to indirectly estimate $N(Al^+)$ in order to increase the number of log $N(Al^{2+})/N(Al^+)$ ratio measurements.

Table 12. Component structure of the $z_{abs} = 3.565$ sub-DLA system towards PSS J2155+1358.

No	z_{abs}	v^*_{rel} km s^{-1}	$b(\sigma_b)$ km s^{-1}	Ion	log $N(\sigma_{\log N})$ cm^{-2}
Low- and intermediate-ion transitions					
1	3.565 272	0	$5.9_{(0.9)}$	Si II	$13.66_{(0.04)}$
				C II	$14.34_{(0.12)}$
				Al II	$12.16_{(0.12)}$
				Fe III	<13.81
				Al III	$12.71_{(0.09)}$
High-ion transitions					
1	3.564 519	−49	$12.5_{(2.6)}$	Si IV	$12.95_{(0.07)}$
				C IV	$13.54_{(0.07)}$
2	3.564 939	−22	$10.8_{(1.1)}$	Si IV	$13.38_{(0.03)}$
				C IV	$13.83_{(0.17)}$
3	3.565 289	+1	$7.4_{(1.2)}$	Si IV	$13.57_{(0.04)}$
				C IV	$13.84_{(0.06)}$
4	3.565 531	+17	$5.5_{(0.9)}$	Si IV	$13.02_{(0.04)}$
				C IV	$13.15_{(0.10)}$
5	3.565 859	+39	$3.7_{(1.1)}$	Si IV	$12.97_{(0.08)}$
				C IV	$13.01_{(0.15)}$
6	3.565 966	+46	$18.8_{(1.0)}$	Si IV	$13.36_{(0.03)}$
				C IV	$13.64_{(0.04)}$

*Velocity relative to $z = 3.565\,272$.

Fig. 30 shows the Al^{2+}/Al^+ column density ratios versus H^0 column densities both for the DLA (open symbols) and sub-DLA (filled

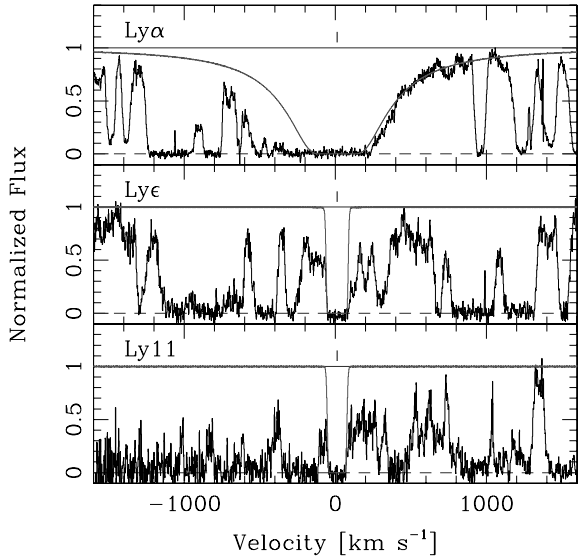

Figure 26. Normalized UVES spectrum of PSS J2155+1358 showing the sub-DLA Lyα, Lyϵ and Ly11 profiles with the Voigt profile fits. The zero velocity is fixed at $z = 4.212\,229$. The vertical bar corresponds to the velocity centroid used for the best fit, $z = 4.212\,442$. The measured H I column density is log N(H I)=19.61 ± 0.10.

Table 13. Component structure of the $z_{\rm abs} = 4.212$ sub-DLA system towards PSS J2155+1358.

No	$z_{\rm abs}$	$v^*_{\rm rel}$ (km s^{-1})	$b(\sigma_b)$ (km s^{-1})	Ion	log $N(\sigma_{\log N})$ (cm^{-2})
Low-ion transitions					
1	4.212 229	0	$6.8_{(0.5)}$	Si II	$13.01_{(0.04)}$
				O I	$14.26_{(0.05)}$
				C II	$13.70_{(0.07)}$
				Al II	$11.62_{(0.16)}$
				Fe II	$12.76_{(0.20)}$
2	4.212 628	+23	$6.3_{(0.6)}$	Si II	$12.88_{(0.04)}$
				O I	$14.13_{(0.05)}$
				C II	$13.59_{(0.05)}$
				Al II	$11.62_{(0.17)}$
				Fe II	$12.43_{(0.30)}$
High-ion transitions					
1	4.212 394	+10	$22.5_{(6.7)}$	Si IV	$12.87_{(0.10)}$
2	4.212 925	+40	$7.9_{(4.9)}$	Si IV	$12.05_{(0.25)}$

*Velocity relative to $z = 4.212\,229$.

symbols) systems. We confirm the log $N(Al^{2+})/N(Al^{+})$ versus log $N(H^0)$ anticorrelation for the enlarged sample of DLA systems (30 objects instead of the 17 used by Vladilo et al. 2001) at the probability of null hypothesis of 5.7×10^{-5} (correlation coefficient of $r = -0.67$; see Table 15). However, we show that at a lower H I column density regime, this correlation is no longer valid. The sub-DLA systems have Al^{2+}/Al^{+} ratios that are similar to those of the DLAs and not higher, as shown in Fig. 30 with five measured values and seven upper limits (filled symbols). Only one system at $z_{\rm abs} = 3.565$ towards PSS J2155+1358 with log N(H I)=19.37 ± 0.15 is really in agreement with the extrapolation of the DLA correlation to lower H I column densities (filled square in the upper left-hand corner in Fig. 30).

This implies that the neutral hydrogen column density is *not* a reliable indicator of the ionization state of the gas in absorption-line systems as suggested by Vladilo et al. (2001), since it does not scale with the Al^{2+}/Al^{+} column density ratio, which is to a first approximation an indicator of the ionization level in the gas. In contrast, Fig. 30 shows that since the sub-DLA systems, despite their lower H I column densities, span approximately the same range of the Al^{2+}/Al^{+} column density ratio values as the DLA systems, they are likely to be affected by ionization corrections on average at the

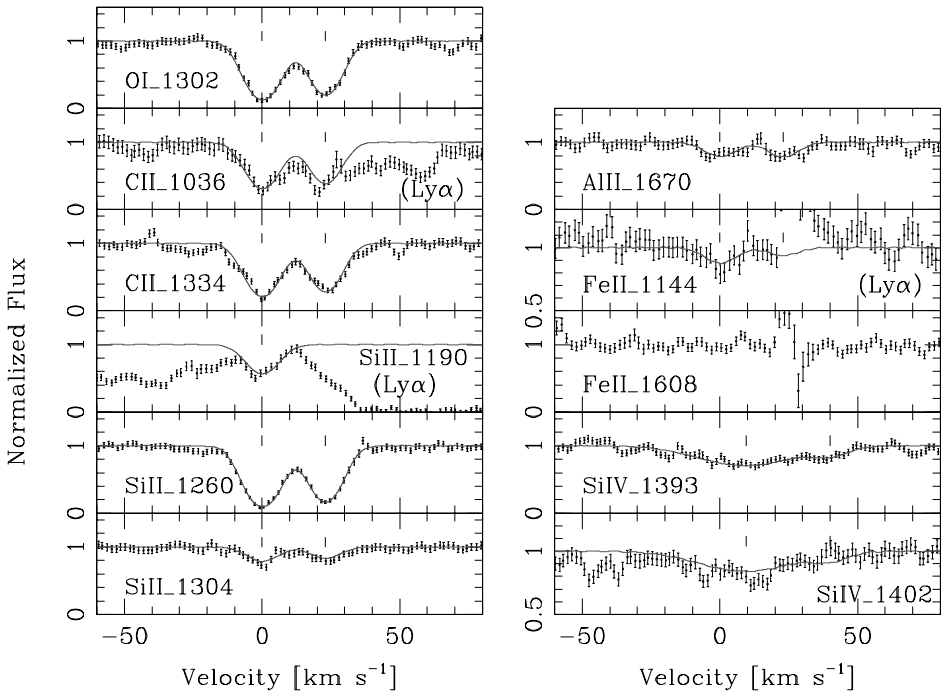

Figure 27. Same as in Fig. 5 for the sub-DLA towards PSS J2155+1358. The zero velocity is fixed at $z = 4.212\,229$. The vertical bars mark the positions of the fitted velocity components (see Table 13).

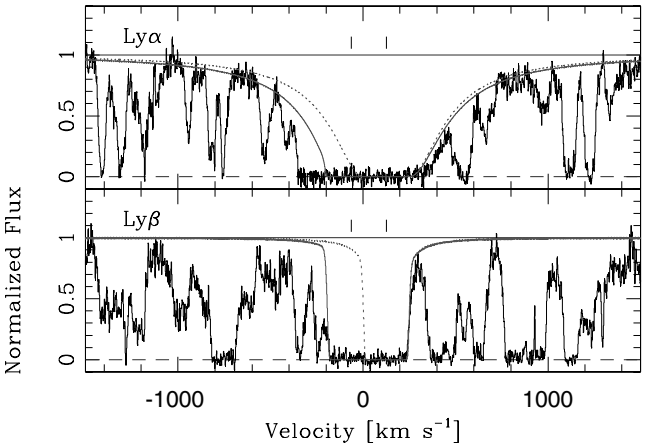

Figure 28. Normalized UVES spectrum of PSS J2344+0342, showing the sub-DLA Lyα profile with the Voigt profile fit. The zero velocity is fixed at $z = 3.882\,639$. The vertical bars correspond from right to left to the velocity centroids $z = 3.884\,697$ and $3.881\,604$ used for the best fit, belonging to the sub-DLA system and an additional absorber, respectively. The dotted line corresponds to the fit with the sub-DLA only. The measured H I column density of the sub-DLA is log N(H I)=19.50 ± 0.10.

same level as the DLAs and not higher. However, we cannot claim that all of the absorption-line systems with H I column densities between 10^{19} and 2×10^{20} cm^{-2} (the sub-DLA H I column density definition) satisfy the same trend, as already shown by the example of the sub-DLA system at $z_{\rm abs} = 3.565$ towards PSS J2155+1358. We can rather interpret the present data as showing an increasing dispersion in the log $N(Al^{2+})/N(Al^{+})$ ratios with lower H^0 column densities. The plotted dashed line in Fig. 30 with the slope of the log $N(Al^{2+})/N(Al^{+})$ versus log $N(H^0)$ anticorrelation observed in DLAs can be considered as an *upper band limit* of this increasing dispersion trend. If this trend is further confirmed by additional measurements, this would suggest that at high $N(H^0) > 2 \times 10^{20}$ cm^{-2} only low ionization effects are expected, while at lower $N(H^0)$ between 10^{19} and 2×10^{20} cm^{-2} one can find systems affected by low and high ionization corrections.

4.2 Photoionization models

To investigate the ionization corrections in our sub-DLAs, we have used the CLOUDY software package (version 94.00, Ferland 1997), and we have computed photoionization models assuming ionization equilibrium. In the models we have adopted a plane-parallel geometry for the gas cloud, the solar abundance pattern, and two different ionizing spectra, since the major uncertainty in determining the ionization effects in absorption-line systems is the unknown shape of the ionizing spectrum. The two most likely origins for ionizing UV photons are external background sources and internal stellar sources – it is reasonable to expect some star formation in these systems. For the external ionizing source, we adopted the Haardt–Madau (hereafter HM) ionizing UV spectrum from background quasars with contributions from galaxies (Haardt & Madau 1996; Madau, Haardt & Rees 1999). For the stellar ionizing source, we adopted the spectrum of a local ionization which we consider to be a composite stellar spectrum plus a power law (hereafter SSP; see D'Odorico & Petitjean 2001). In the former case the ionizing photons have a harder spectrum.

With each of these two ionizing spectra, we computed a series of CLOUDY models for each sub-DLA system in our sample by varying the H I column density of the plane-parallel 'cloud', the metallicity and the redshift according to the system considered, and by varying the volume density of hydrogen, $n_{\rm H}$, through the variation of the ionization parameter, U, defined by

$$U \equiv \frac{\Phi_{912}}{cn_{\rm H}} = \frac{4\pi J_{912}}{hcn_{\rm H}} = 2 \times 10^{-5} \frac{J_{912}/10^{-21.5}}{n_{\rm H}/{\rm cm}^{-3}},$$

where Φ_{912} is the surface flux of ionizing photons with $h\nu >$ 1 Ryd, and J_{912} is the intensity of the incident radiation at 1 Ryd. In practice, we varied log U from −6 to 0, and obtained the theoretical column density predictions for all of the observed ions as a function of the ionization parameter.

We then determined the ionization state of a given sub-DLA system by measuring adjacent ions of elements (e.g. Al^{2+}/Al^{+}, Fe^{2+}/Fe^{+}). Indeed, the value of the ionization parameter, U, at which the observed column density ratio of adjacent ions matches the predicted ratio, corresponds to the ionization parameter of the system studied. Therefore, the more numerous the measurements of column density ratios of adjacent ions of different elements, the more accurate is the determination of the ionization state of a system, all the more so since the reliability of the derived photoionization models depends not only on the assumed hypothesis, but also on the

Table 14. Component structure of the $z_{\rm abs} = 3.882$ sub-DLA system towards PSS J2344+0342.

No	$z_{\rm abs}$	$v^*_{\rm rel}$ km s^{-1}	$b(\sigma_b)$ km s^{-1}	Ion	log $N(\sigma_{\log N})$ cm^{-2}
Low-ion transitions					
1	3.880 511	−131	$8.7_{(2.0)}$	Si II	$12.91_{(0.11)}$
				C II	$13.55_{(0.06)}$
				Al II	$11.28_{(0.15)}$
2	3.880 811	−112	$5.6_{(1.3)}$	Si II	$12.87_{(0.10)}$
				C II	$13.48_{(0.06)}$
				Al II	$11.68_{(0.25)}$
3	3.881 785	−52	$7.4_{(1.1)}$	Si II	$13.08_{(0.05)}$
				C II	$13.79_{(0.06)}$
				Al II	$11.92_{(0.09)}$
4	3.882 032	−37	$6.5_{(1.9)}$	Si II	$12.63_{(0.07)}$
				C II	$13.35_{(0.14)}$
5	3.882 392	−15	$4.2_{(3.3)}$	C II	$12.88_{(0.15)}$
6	3.882 639	0	$6.4_{(1.1)}$	Si II	$12.95_{(0.10)}$
				C II	$13.59_{(0.04)}$
				Al II	$11.59_{(0.15)}$
7	3.883 733	+67	$25.6_{(2.8)}$	C II	$13.91_{(0.04)}$
8	3.884 153	+93	$7.1_{(3.4)}$	C II	$12.87_{(0.32)}$
9	3.884 580	+119	$10.5_{(0.9)}$	Si II	$13.45_{(0.04)}$
				C II	$14.12_{(0.04)}$
				Al II	$11.92_{(0.09)}$
10	3.885 067	+149	$12.1_{(1.2)}$	Si II	$13.35_{(0.05)}$
				C II	$14.09_{(0.03)}$
				Al II	$12.16_{(0.06)}$
11	3.885 412	+170	$3.5_{(2.0)}$	C II	$13.02_{(0.09)}$
High-ion transitions					
1	3.883 235	+37	$20.0_{(5.7)}$	C IV	$13.15_{(0.10)}$
2	3.883 706	+66	$11.8_{(2.8)}$	Si IV	$12.91_{(0.07)}$
				C IV	$13.50_{(0.04)}$
3	3.884 165	+94	$10.7_{(1.4)}$	Si IV	$13.00_{(0.04)}$
				C IV	$13.40_{(0.05)}$
4	3.884 840	+135	$18.8_{(3.9)}$	Si IV	$13.28_{(0.10)}$
				C IV	$13.79_{(0.04)}$
5	3.885 314	+164	$7.7_{(1.4)}$	Si IV	$12.81_{(0.06)}$
				C IV	$13.35_{(0.06)}$

*Velocity relative to $z = 3.882\,639$.

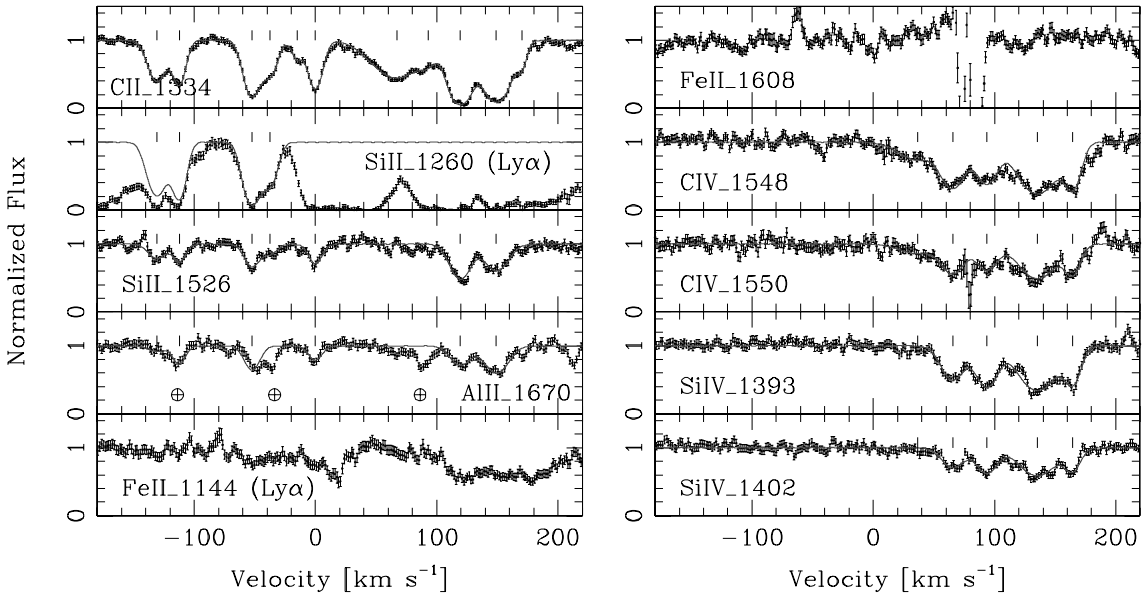

Figure 29. Same as in Fig. 5 for the sub-DLA towards PSS J2344+0342. The zero velocity is fixed at $z = 3.882\,639$. The vertical bars mark the positions of the fitted velocity components (see Table 14).

Table 15. Spearman's tests and linear regressions.

Correlations for the whole sample of both the DLA and sub-DLA systems	No of systems	r	α	Slope	Intercept
log $N(Si^+)$ versus log $N(Fe^+)$	39	0.95	3.2×10^{-20}	1.04 ± 0.04	-0.10 ± 0.58
log $N(Al^+)$ versus log $N(Si^+)$	19	0.92	3.4×10^{-08}	0.97 ± 0.08	-0.97 ± 1.19
log $N(Al^+)$ versus log $N(Fe^+)$	17	0.82	4.9×10^{-05}	0.89 ± 0.13	0.58 ± 1.83
log $N(Al^{2+})/N(Al^+)$ versus log $N(H^0)$*	30	−0.67	5.7×10^{-05}	-0.59 ± 0.13	11.49 ± 2.84

*Computed for the sample of DLAs only.
References: this paper; Dessauges-Zavadsky et al. (2001a); Lopez et al. (1999, 2002); Lu et al. (1995, 1996b); Prochaska & Wolfe (1996, 1997, 1999); Prochaska et al. (2001b); Péroux et al. (2002b).

accuracy of the input atomic data for the CLOUDY code (e.g. dielectric recombination coefficients).

Following the ionization analysis of Prochaska et al. (2002), we have further computed models giving the predicted abundance of low-ion X_i over H^0 and Fe^+ relative to the intrinsic abundance of these two elements,

$$\left[X_i/H^0\right] = \log\left[N(X_i)/N(H^0)\right] - \log(X/H)_\odot,$$

$$\left[X_i/Fe^+\right] = \log\left[N(X_i)/N(Fe^+)\right] - \log(X/Fe)_\odot,$$

as a function of the ionization parameter, U. Departures of $[X_i/H^0]$ and $[X_i/Fe^+]$ from zero indicate that ionization corrections have to be added to the observed absolute and relative elemental abundances, respectively. When the corrections to be applied are negative (positive), this implies that the measured [X/H] or [X/Fe] are underestimated (overestimated). The main advantage of these models compared with the models giving the predicted X_i column densities as a function of U is that they allow a direct quantification of the effects of photoionization on the absolute and relative abundances.

4.3 Results: ionization corrections

In the sample of the 12 sub-DLA systems and one borderline case between the DLA and sub-DLA systems studied here, the H I column densities range from log $N(H\,I)$=19.32 to 20.30 cm^{-2}, and the metallicities are spread over 1.5 dex (from [Fe/H] <−2.40 to [Fe/H]=−0.79). This large range of input parameters for the CLOUDY models allows us to highlight some general trends. Indeed, the computed CLOUDY models specific to each sub-DLA system in our sample show that for a given ionization parameter, U, the derived $[X_i/H^0]$ and $[X_i/Fe^+]$ ionization corrections (as defined in Section 4.2) increase with lower H I column densities of systems for all low-ions X_i and for both the HM or SSP ionizing spectra, while no particular trend is observed with the metallicity of the systems. In addition, we note that the ionization corrections are on average more important in the models with an SSP radiation field than with an HM spectrum for all of the systems studied. We show in Figs 31 and 32 the CLOUDY models for two sub-DLA systems, one at $z_{abs} = 2.557$ towards Q1223+1753 with a very low H I column density log $N(H\,I)$=19.32 ± 0.15 and a high [Fe/H]=−0.84 ± 0.15, and the second one at $z_{abs} = 3.142$ towards PSS J2155+1358 with a high H I column density log $N(H\,I)$=19.94 ± 0.10 and a low [Fe/H]= −2.21 ± 0.21, respectively. They illustrate these general trends.

Once we have computed the CLOUDY models, the determination of the ionization state is crucially dependent on the measurements of column density ratios of adjacent ions of elements, and thus on the detections of intermediate-ion transitions. In the sample of 13 systems studied, we were able to constrain the ionization parameter,

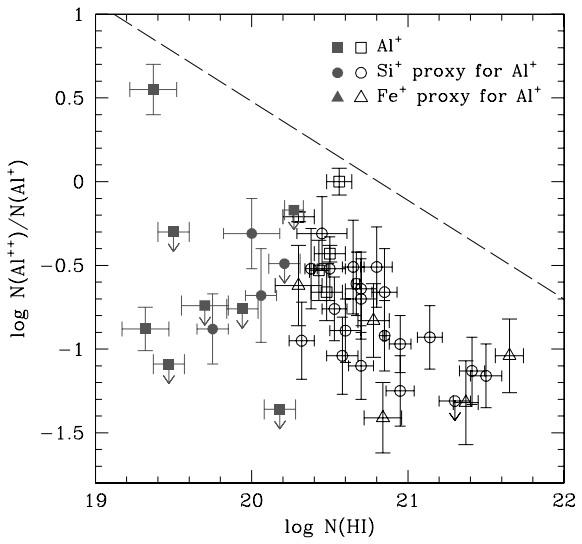

Figure 30. Al^{2+}/Al^{+} column density ratios versus H I column densities in sub-DLAs (filled symbols) and DLAs (open symbols) for all the systems found in the literature and studied in this paper. The squares correspond to the data points obtained with the Al^{+} column density measurements, while the circles and the triangles correspond to the data points computed from the Si^{+} and Fe^{+} column density measurements, respectively, according to the deduced linear regression parameters given in Table 15. The dashed line represents a possible upper band limit of an increasing dispersion in the log $N(Al^{2+})/N(Al^{+})$ ratios with lower H I column densities. The slope of this upper band limit is equal to the slope of the observed log $N(Al^{2+})/N(Al^{+})$ versus log $N(H^{0})$ anticorrelation in DLAs.

U, for 10 systems. However, we obtained $N(Al^{2+})/N(Al^{+})$ and/or $N(Fe^{2+})/N(Fe^{+})$ measurements for only four systems, while for the six remaining systems we derived only $N(Al^{2+})/N(Al^{+})$ and/or $N(Fe^{2+})/N(Fe^{+})$ upper limits. The analysis of the ionization state of our sub-DLA systems is thus severely limited by the fact that (i) we do not have a measurement of a column density ratio of adjacent ions of an element for all of the sub-DLAs, and (ii) for the majority of sub-DLAs we have only a measurement of the Al^{2+}/Al^{+} ratio or even only an upper limit, and as has already been pointed out by Petitjean, Rauch & Carswell (1994), D'Odorico & Petitjean (2001) and Vladilo et al. (2001), the Al^{2+}/Al^{+} ratio is not a very reliable indicator of the ionization parameter. Indeed, the recombination coefficient of Al^{+} is probably overestimated (Nussbaumer & Storey 1986), and in this case the predicted Al^{2+}/Al^{+} ratio in the CLOUDY models is underestimated. This prevents us from obtaining a very accurate determination of the ionization parameter in our sub-DLA systems. In addition, with our set of data, we are not able to constrain the nature of the radiation field, since we cannot clearly differentiate which of the HM or SSP ionizing spectrum best represents the observations.

In this context we choose to extract from our analysis general conclusions on the ionization corrections in the sub-DLA systems studied, rather than a discussion on individual systems which is limited by the partial information we have. Several important general remarks can be inferred from our study. First, as can be observed in Figs 31 and 32, the ionization corrections to apply to absolute and relative abundances are different from ion to ion. Indeed, in the case of C^{+}, O^{0}, S^{+} or Cr^{+}, for example, the ionization corrections $[X_i/Fe^{+}]$ increase smoothly with the ionization parameter, U, and remain relatively small for all of the U values, while for the Si^{+}, Al^{+} and Zn^{+} ions they already become important at relatively low U values. Similarly, for the metallicities, the $[X_i/H^{0}]$ corrections are not significant for Fe^{+} up to high U values, while they are much higher for Zn^{+} at high U values. Secondly, for nine systems out of 10 for which we were able to constrain the ionization parameter the ionization corrections are lower than 0.2 dex for all of the elements except Al II and Zn II (in some cases, mainly if we assume that the SSP radiation field is the dominant ionizing source in our systems) down to H I column densities of log $N(H\,I)$=19.3 cm^{-2} (see Figs 31 and 32). In the case of Al^{+} and Zn^{+} the ionization corrections may be overestimated, since the Al^{+} and Zn^{+} recombination coefficients and ionization cross-sections are rather uncertain (see Nussbaumer & Storey 1986; Howk, Savage & Fabian 1999, respectively). Only in the sub-DLA system at $z_{abs} = 3.565$ towards PSS J2155+1358 are the ionization corrections important (filled square in the upper left-hand corner in Fig. 30). For three sub-DLAs in our sample we could not constrain the ionization parameter, U.

5 OVERVIEW OF THE CHEMICAL ABUNDANCES IN SUB-DLAS

The constructed sample of 12 sub-DLA systems and one borderline case between the DLA and sub-DLA systems, and the homogeneous chemical abundance analysis of each system presented in this paper result in the first sub-DLA chemical abundance data base ideal for the study of a number of important issues. Indeed, 16 different ions of low-, intermediate- and high-ionization and 11 different elements – O, C, Si, N, S, Mg, Al, Fe, Ni, Zn and Cr – have been detected in the 13 systems studied, showing a variety of elements as diverse as that observed in the DLAs. Tables 16(a) and (b) present a summary of the column density measurements of the low-ion transitions and the intermediate-/high-ion transitions, respectively, obtained in the 13 systems analysed. These column densities were derived by summing the column densities of all of the detected velocity components in each ion as given in Tables 2–14 . The cases in which we provide only lower limits correspond to the cases where the observed metal lines are saturated, and the cases in which we provide only upper limits correspond to cases where the observed metal lines are blended with Lyα forest absorption lines. 4σ upper limits were derived in the cases where the metal lines are not detected and are identified by an asterisk.

In Table 17 we provide a summary of the absolute abundance measurements of the 12 sub-DLA systems and one borderline case between the DLA and sub-DLA systems, defined with respect to the solar meteoritic abundances from Grevesse & Sauval (1998). No ionization correction has been adopted since, as was shown in Section 4 for all of the systems studied for which we were able to constrain the ionization parameter (10 systems out of 13) except one at $z_{abs} = 3.565$ towards PSS J2155+1358, the ionization corrections are almost negligible, being at the level of the errors. Indeed, they are lower than 0.2 dex for all of the elements except Al II and Zn II (in some cases, but are probably overestimated because the Al^{+} and Zn^{+} recombination coefficients are very uncertain) down to H I column densities of log $N(H\,I)$=19.3 cm^{-2}.

Fig. 33 shows the distribution of iron and silicon absolute abundances, [Fe/H] and [Si/H], as a function of redshift and H I column density for the 12 sub-DLAs in our sample. The studied sub-DLAs span a range of redshift from 1.8 to 4.3 and of [Fe/H] metallicities from -0.79 to <-2.40, which is very similar to that observed in DLAs. We observe a trend of increasing metallicity with redshift, but no correlation between metallicities and H I column densities is visible. An overall discussion on the chemical abundances of

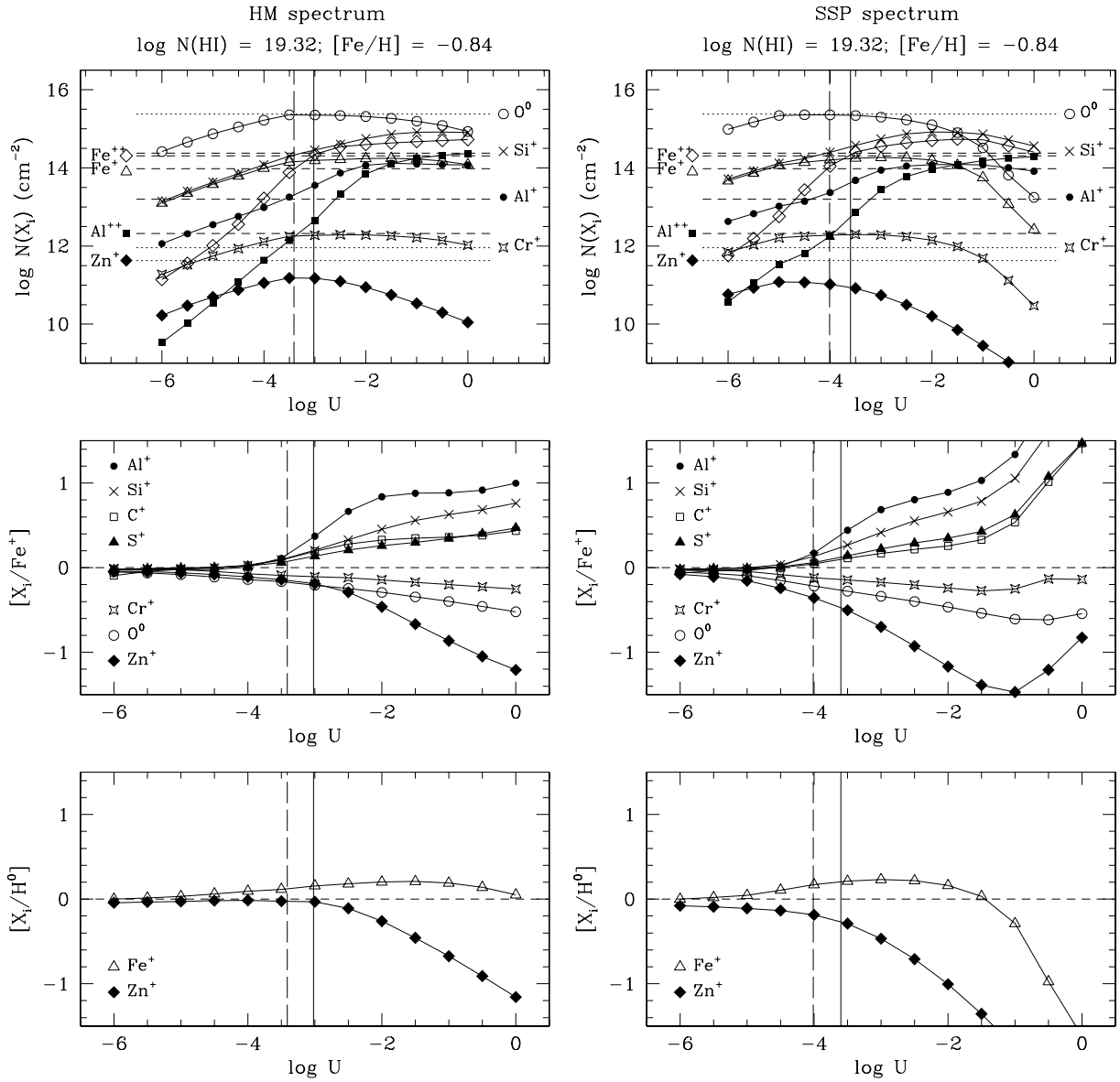

Figure 31. Photoionization models computed with the CLOUDY software package for the sub-DLA at $z_{\rm abs} = 2.557$ towards Q1223+1753. This system is characterized by a relatively high metallicity [Fe/H]=−0.84 ± 0.15 and has one of the lowest H I column density [log N(H I)=19.32 ± 0.15] among the sub-DLA systems in our sample. On the left-hand side, the models are the result obtained with the Haardt–Madau UV ionizing source, and on the right-hand side, a stellar ionizing source is assumed. In all panels the vertical lines indicate the observational constraint on U obtained from the Al^{2+}/Al^{+} (solid lines) and Fe^{2+}/Fe^{+} (long-dashed lines) ratios. The top panels show the predicted ionic column densities, $N(X_i)$, as a function of the ionization parameter, U. The horizontal dashed lines correspond to the observed column density values and the horizontal dotted lines correspond to the observed column density upper limits. The middle and bottom panels show the predicted abundance of low-ion X_i over Fe^{+} and H^0 relative to the intrinsic abundance of these two elements, as defined in Section 4.2, versus U, respectively. Departures of [X_i/Fe] and [X_i/H] indicate that ionization corrections have to be added to/subtracted from the observed relative and absolute abundances, respectively.

sub-DLAs, and a detailed comparison of the chemical, kinematic and clustering properties between the sub-DLAs and DLAs is given in Paper II.

The lower H I column densities of the sub-DLA systems relative to the DLA systems give us the opportunity to have access to some elements for which absorption lines are usually saturated in DLAs, but prevent us from measuring abundances of some other elements where the lines are already weak in DLAs. As examples of the former case, one can quote carbon and oxygen. Indeed, C is almost not accessible in DLAs, since the C II λλ1036,1334 lines are heavily saturated. Only very few tentative measurements have been obtained (Lopez et al. 1999, 2002; Levshakov et al. 2002; Songaila & Cowie 2002). The O abundance is also very difficult to measure in DLAs, since the most commonly detected O I line at $\lambda_{\rm rest}$ = 1302 Å is saturated and other O I lines are located in the Lyα forest. In contrast, in the sub-DLA systems one can more easily measure the abundances of these two important elements – we obtained four O and six C abundance measurements – which may provide insight into the understanding of the nature and the chemical evolution history of these systems (see Paper II). On the other hand, the useful Zn abundance used as an indicator of the dust depletion in DLAs is very hard to measure in sub-DLAs given the weakness of the Zn II lines.

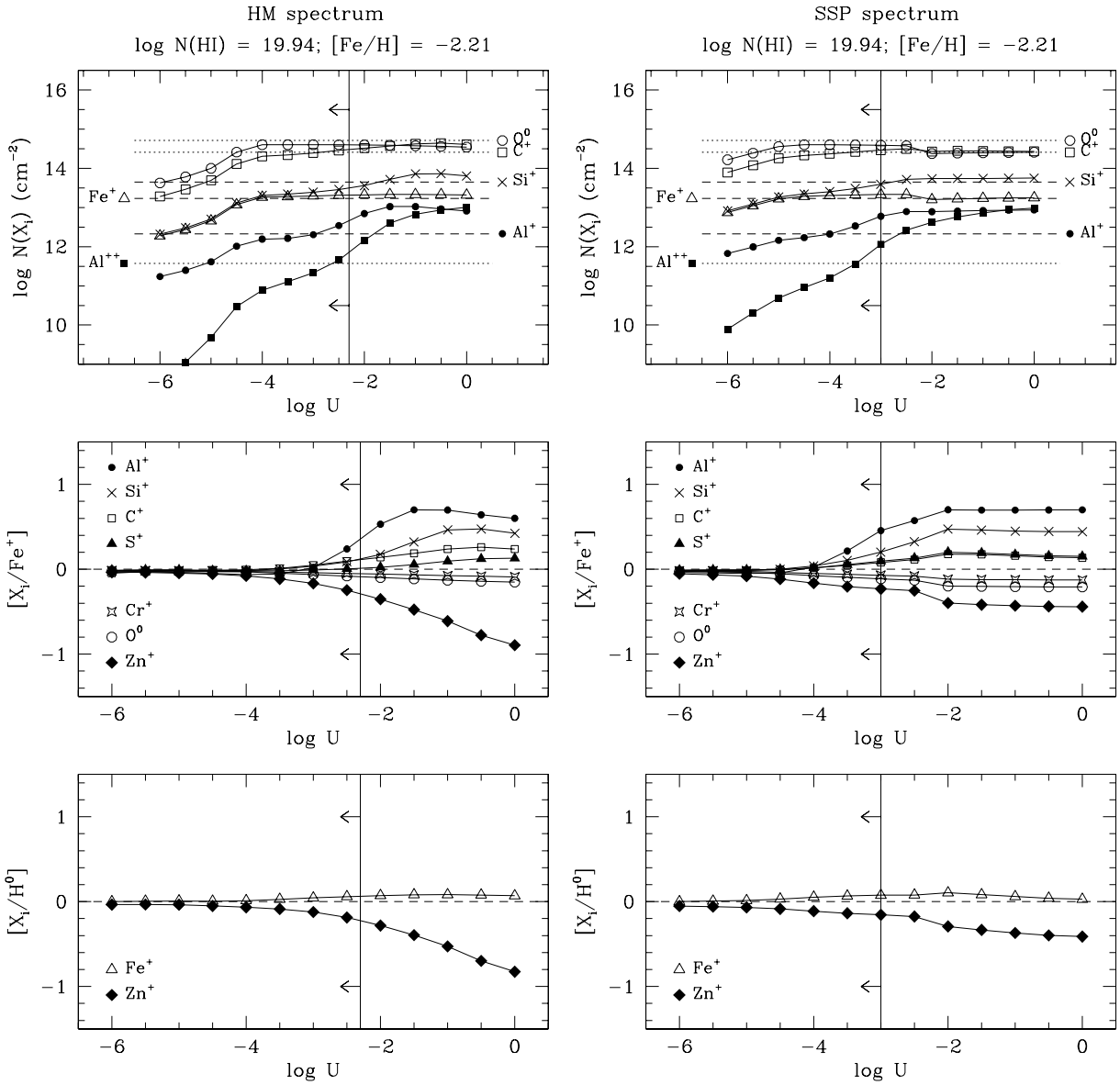

Figure 32. Same as in Fig. 31 for the sub-DLA at $z_{\rm abs} = 3.142$ towards PSS J2155+1358. This system is characterized by a low metallicity [Fe/H]=−2.21 ± 0.21 and has one of the highest H I column densities [log N(H I)=19.94 ± 0.10] among the sub-DLA systems in our sample. In all panels the vertical line indicates the observational constraint on U obtained from the Al^{2+}/Al^{+} upper limit.

While numerous Zn abundance measurements exist in DLAs, we obtained only two Zn measurements in our sample of sub-DLAs.

6 CONCLUSION

The findings by Péroux et al. (2003a) that the 'sub-DLA' systems with H I column densities between $10^{19} < N(\rm H\,I) < 2 \times 10^{20}$ cm^{-2} contain a large fraction of the neutral hydrogen gas mass, especially at $z > 3.5$, have motivated us to investigate systematically quasar spectra in the ESO UVES-VLT archives searching for these absorbers. We have obtained the following results.

(i) Out of 22 high-resolution quasar spectra available to us in 2001 July in the ESO UVES-VLT archives and suitable for the construction of a sample of sub-DLA systems, reduced and analysed with an identical approach, we have built the first sample of 12 sub-DLA systems in the redshift interval $z = 1.8$–4.3. These systems were identified in the quasar spectra both via an automated selection algorithm and visual criteria, such as the presence of damping wings in the Lyα absorption line. 10 of them constitute a sample that we believe to be homogeneous and unbiased.

(ii) The detailed metal-line analysis of each of the 12 sub-DLA systems and one borderline case between the DLA and sub-DLA systems resulted in the column density measurements of 16 ions of low, intermediate and high ionization: O I, C II, C IV, Si II, Si IV, N I, S II, Mg I, Mg II, Al II, Al III, Fe II, Fe III, Ni II, Zn II and Cr II. The detection of adjacent ions of the same element, Fe^{2+}/Fe^{+} and Al^{2+}/Al^{+}, allowed us to estimate the ionization parameters in 10 systems. Using the CLOUDY software package, we computed photoionization models and found that for all of the 10 systems except one at $z_{\rm abs} = 3.565$ towards PSS J2155+1358, the ionization corrections are almost negligible, being at the level of the errors. Indeed, they are lower than 0.2 dex for all of the elements except Al II and

Table 16. (a) Low-ion transition column density summary.

Name	z_{abs}	log N(H I)	log N(O I)	log N(C II)	log N(Si II)	log N(N I)	log N(S II)	log N(Mg II)	log N(Al II)	log N(Fe II)	log N(Ni II)	log N(Zn II)	log N(Cr II)
Q1101−264[a].....	1.838	$19.50_{(0.05)}$	$14.55_{(0.09)}$	$15.06_{(0.07)}$	$14.00_{(0.01)}$	...	$13.66_{(0.11)}$	$14.07_{(0.03)}$	$12.85_{(0.06)}$	$13.51_{(0.02)}$	...	<11.39*	<12.04*
Q1223+1753.....	2.557	$19.32_{(0.15)}$	<15.38	...	$14.38_{(0.02)}$	...	...	...	$13.20_{(0.03)}$	$13.98_{(0.03)}$	...	<11.63*	<11.96*
Q1409+095.....	2.668	$19.75_{(0.10)}$	$15.31_{(0.11)}$	>16.09	$14.13_{(0.03)}$	<13.49	$13.54_{(0.06)}$	...	...	$14.02_{(0.13)}$	...	<11.34*	$12.49_{(0.15)}$
Q1444+014.....	2.087	$20.18_{(0.10)}$	>16.08	>16.30	$14.83_{(0.02)}$	...	...	...	$13.42_{(0.03)}$	$14.41_{(0.03)}$	...	...	...
Q1451+123.....	2.255	$20.30_{(0.15)}$	...	...	>15.46	...	...	...	...	$14.33_{(0.07)}$	<13.53	$11.85_{(0.11)}$	$12.88_{(0.14)}$
Q1451+123.....	3.171	$19.70_{(0.15)}$	<14.80	$14.30_{(0.20)}$	$13.64_{(0.03)}$	...	...	...	$12.31_{(0.03)}$	$13.33_{(0.06)}$	...	<12.01*	<12.65*
Q1511+090.....	2.088	$19.47_{(0.10)}$	<15.30	...	$14.05_{(0.10)}$	...	...	...	$12.93_{(0.14)}$	$13.26_{(0.03)}$	...	...	...
Q2059−360.....	2.507	$20.21_{(0.10)}$	$15.54_{(0.21)}$	$14.87_{(0.19)}$	$13.73_{(0.11)}$	$12.66_{(0.18)}$	...	...	...	$13.47_{(0.03)}$	...	<11.54*	<12.19*
Q2116−358.....	1.996	$20.06_{(0.10)}$	>16.68	...	$15.33_{(0.12)}$	...	<14.95	...	>13.94	$14.77_{(0.09)}$	$13.57_{(0.06)}$	$12.29_{(0.09)}$	$12.92_{(0.13)}$
PSS J2155+1358.....	3.142	$19.94_{(0.10)}$	<14.71	<14.41	$13.65_{(0.07)}$	...	...	...	$12.33_{(0.10)}$	$13.23_{(0.19)}$	...	...	...
PSS J2155+1358.....	3.565	$19.37_{(0.15)}$	...	$14.34_{(0.12)}$	$13.66_{(0.04)}$	...	...	...	$12.16_{(0.12)}$	<12.47*	...	...	...
PSS J2155+1358.....	4.212	$19.61_{(0.10)}$	$14.50_{(0.05)}$	$13.95_{(0.06)}$	$13.25_{(0.04)}$	...	...	...	$11.92_{(0.17)}$	$12.93_{(0.23)}$	...	...	...
PSS J2344+0342[b]...	3.882	$19.50_{(0.10)}$	...	$14.74_{(0.05)}$	$13.96_{(0.06)}$	...	...	...	$12.62_{(0.11)}$	<13.02*	...	...	...

[a]The Mg II column density is also measured in this sub-DLA: log N(Mg II) = 11.89 ± 0.02.
[b]If components 1–6 do not belong to the sub-DLA (see Section 3.11), then: log N(C II) = 14.55 ± 0.04, log N(Si II) = 13.70 ± 0.04 and log N (Al II) = 12.36 ± 0.07.

(b) Intermediate- and high-ion transition column density summary.

Name	z_{abs}	log N(H I)	log N(Al III)	log N(Fe III)	log N(C IV)	log N(Si IV)
Q1101−264.....	1.838	$19.50_{(0.05)}$	$12.34_{(0.04)}$	...	$14.22_{(0.04)}$	$13.84_{(0.05)}$
Q1223+1753.....	2.557	$19.32_{(0.15)}$	$12.32_{(0.13)}$	$14.31_{(0.13)}$	$14.44_{(0.04)}$	$13.99_{(0.02)}$
Q1409+095.....	2.668	$19.75_{(0.10)}$	$11.89_{(0.05)}$	$13.17_{(0.12)}$	...	...
Q1444+014.....	2.087	$20.18_{(0.10)}$	<12.06*	<13.90*	$13.22_{(0.05)}$	$12.94_{(0.04)}$
Q1451+123.....	2.255	$20.30_{(0.15)}$	$12.70_{(0.05)}$	...	...	...
Q1451+123.....	3.171	$19.70_{(0.15)}$	<11.57*	...	$13.48_{(0.13)}$	...
Q1511+090.....	2.088	$19.47_{(0.10)}$	<11.84*	<13.75*	...	...
Q2059−360.....	2.507	$20.21_{(0.10)}$	<11.89*	...	...	...
Q2116−358.....	1.996	$20.06_{(0.10)}$	$13.25_{(0.09)}$	<14.60	>15.28	$14.38_{(0.02)}$
PSS J2155+1358.....	3.142	$19.94_{(0.10)}$	<11.57	...	...	...
PSS J2155+1358.....	3.565	$19.37_{(0.15)}$	$12.71_{(0.09)}$	<13.81	$14.38_{(0.10)}$	$14.05_{(0.04)}$
PSS J2155+1358.....	4.212	$19.61_{(0.10)}$	...	...	...	$12.93_{(0.12)}$
PSS J2344+0342.....	3.882	$19.50_{(0.10)}$	<12.32*	...	$14.19_{(0.05)}$	$13.64_{(0.07)}$

*4σ upper limit (corresponding to non-detections).

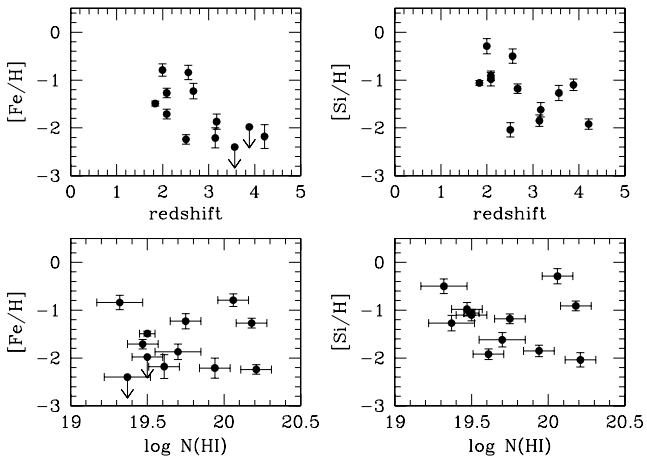

Figure 33. The four plots show the distribution of the abundances of Fe and Si as a function of redshift and H I column density, to illustrate the values sampled by the 12 sub-DLA systems in our sample. The overall abundances are presented in Table 17.

Zn II (in some cases, but probably overestimated because the Al^+ and Zn^+ recombination coefficients are very uncertain) down to H I column densities of log N(H I)=19.3 cm^{-2}.

(iii) We have obtained the first sub-DLA chemical abundance data base, which contains the abundance measurements of 11 different elements: O, C, Si, N, S, Mg, Al, Fe, Ni, Zn and Cr. The lower H I column densities of sub-DLAs allowed us, in particular, to easily measure the O and C abundances, the O I and C II lines being usually saturated in DLAs. We obtained O abundance measurements in four systems and C in six systems.

The constructed homogeneous and unbiased sample of the sub-DLA systems and the obtained sub-DLA chemical abundance data base are ideal for the analysis of a number of important issues related both to the neutral gas mass and the metal content evolution in the Universe. These issues are discussed in Paper II of this series, where we also present a detailed study of the sub-DLA kinematic, chemical and clustering properties, and their comparison with the properties of the well-studied DLA systems. We plan to extend the current sample of sub-DLA systems in order to increase the statistical weight of the obtained results both from the newly accessible data in the ESO UVES archives and from observations of pre-selected high-redshift quasars, since it is at high redshift $z > 3.5$ that the sub-DLAs are expected to contain a large fraction of the neutral hydrogen gas mass (Péroux et al. 2002a).

ACKNOWLEDGMENTS

This paper is based on ESO public data released from 2001 July obtained with UVES at the VLT Kueyen telescope, Paranal, Chile. We are very grateful to Paolo Molaro and Miriam Centurión for providing us with the reduced and normalized spectrum of the quasar Q0000−2620. We particularly thank Miriam Centurión for her help in the computation of photoionization models. We express our gratitude to the ESO staff in charge of the VLT archive for their efficient work to the benefit of the community. We thank an anonymous referee for helpful comments. MD-Z is supported by the Swiss National Funds and CP is funded by a European Marie Curie Fellowship.

Table 17. Absolute abundance summary.

Name	z_{abs}	log N(H I)	[O/H]	[C/H]	[Si/H]	[N/H]	[S/H]	[Mg/H]	[Al/H]	[Fe/H]	[Ni/H]	[Zn/H]	[Cr/H]
Q1101−264.....	1.838	$19.50_{(0.05)}$	$-1.78_{(0.12)}$	$-0.96_{(0.10)}$	$-1.06_{(0.05)}$	...	$-1.04_{(0.13)}$	$-1.01_{(0.06)}$	$-1.14_{(0.08)}$	$-1.49_{(0.05)}$	...	$<-0.78^*$	$<-1.15^*$
Q1223+1753.....	2.557	$19.32_{(0.15)}$	<-0.77	...	$-0.50_{(0.15)}$	...	...	...	$-0.61_{(0.15)}$	$-0.84_{(0.15)}$	...	$<-0.36^*$	$<-1.05^*$
Q1409+095.....	2.668	$19.75_{(0.10)}$	$-1.27_{(0.16)}$	>-0.18	$-1.18_{(0.10)}$	<-2.18	$-1.41_{(0.13)}$	...	...	$-1.23_{(0.16)}$	...	$<-1.08^*$	$-0.95_{(0.18)}$
Q1444+014.....	2.087	$20.18_{(0.10)}$	>-0.93	>-0.40	$-0.91_{(0.10)}$	...	...	...	$-1.25_{(0.10)}$	$-1.27_{(0.10)}$	...	...	...
Q1451+123.....	2.255	$20.30_{(0.15)}$	...	...	>-0.40	...	...	...	...	$-1.47_{(0.17)}$	<-1.02	$-1.12_{(0.19)}$	$-1.11_{(0.20)}$
Q1451+123.....	3.171	$19.70_{(0.15)}$	<-1.73	$-1.92_{(0.26)}$	$-1.62_{(0.15)}$	...	...	...	$-1.88_{(0.15)}$	$-1.87_{(0.16)}$	...	$<-0.36^*$	$<-0.74^*$
Q1511+090.....	2.088	$19.47_{(0.10)}$	<-1.00	...	$-0.98_{(0.14)}$	...	...	...	$-1.03_{(0.17)}$	$-1.71_{(0.10)}$	...	...	...
Q2059−360.....	2.507	$20.21_{(0.10)}$	$-1.50_{(0.24)}$	$-1.86_{(0.22)}$	$-2.04_{(0.15)}$	$-3.47_{(0.21)}$	...	...	...	$-2.24_{(0.10)}$	...	$<-1.34^*$	$<-1.71^*$
Q2116−358.....	1.996	$20.06_{(0.10)}$	>-0.21	...	$-0.29_{(0.16)}$	...	<-0.31	...	>-0.61	$-0.79_{(0.13)}$	$-0.74_{(0.12)}$	$-0.44_{(0.14)}$	$-0.83_{(0.16)}$
PSS J2155+1358....	3.142	$19.94_{(0.10)}$	<-2.06	<-2.05	$-1.85_{(0.12)}$	...	...	...	$-2.10_{(0.14)}$	$-2.21_{(0.21)}$	...	...	...
PSS J2155+1358[c]...	3.565	$19.37_{(0.15)}$	...	$-1.55_{(0.20)}$	$-1.27_{(0.16)}$	...	...	...	$-1.70_{(0.19)}$	$<-2.40^*$	...	...	...
PSS J2155+1358....	4.212	$19.61_{(0.10)}$	$-1.94_{(0.13)}$	$-2.18_{(0.13)}$	$-1.92_{(0.11)}$	...	...	...	$-2.18_{(0.20)}$	$-2.18_{(0.25)}$	...	...	...
PSS J2344+0342....	3.882	$19.50_{(0.10)}$	...	$-1.28_{(0.13)}$	$-1.10_{(0.12)}$	...	...	...	$-1.37_{(0.15)}$	$<-1.98^*$	...	...	...

*4σ upper limit (corresponding to non-detections).
[c]This system is very likely to be affected by high ionization corrections (see Section 4).
Abundances relative to the solar values of Grevesse & Sauval (1998).

REFERENCES

Adam G., 1985, A&AS, 61, 225
Ballester P., Modigliani A., Boitquin O., Cristiani S., Hanuschik R., Kaufer A., Wolf S., 2000, Messenger, 101, 31
Bechtold J., 1994, ApJS, 91, 1
Calura F., Matteucci F., Vladilo G., 2003, MNRAS, 340, 59
Carswell R.F., Morton D.C., Smith M.G., Stockton A.N., Turnshek D.A., Weymann R.J., 1984, ApJ, 278, 486
Cen R., Ostriker J.P., 1999, ApJ, 519, L109
Cen R., Ostriker J.P., Prochaska J.X., Wolfe A.M., 2003, ApJ, accepted (astro-ph/0203524)
Centurión M., Bonifacio P., Molaro P., Vladilo G., 2000, ApJ, 536, 540
Dessauges-Zavadsky M., D'Odorico S., McMahon R.G., Molaro P., Ledoux C., Péroux C., Storrie-Lombardi L.J., 2001a, A&A, 370, 426
Dessauges-Zavadsky M., D'Odorico S., McMahon R.G., Péroux C., 2001b, in Ferlet R., Lemoine M., Desert J.-M., Raban B., eds, XVIIth IAP Colloquium, Gaseous Matter in Galaxies and Intergalactic Space. Frontier Group, Paris, p. 327
Dessauges-Zavadsky M., Prochaska J.X., D'Odorico S., 2002, A&A, 391, 801
D'Odorico V., Petitjean P., 2001, A&A, 370, 729
D'Odorico S., Cristiani S., Dekker H., Hill V., Kaufer A., Kim T.S., Primas F., 2000, in Bergeron J., ed., Proc. SPIE 4005, Discoveries and Research Prospects from 8- to 10-Meter-Class Telescopes. Int. Soc. Opt. Eng., Bellingham, WA, p. 121
Ellison S.L., Ryan S.G., Prochaska J.X., 2001, MNRAS, 326, 628
Ferland G.J., 1997, Hazy, a brief introduction to CLOUDY 94.00. Univ. Kentucky, Dept. Phys. Astron. internal report
Foltz C.B., Chaffee F.H., Jr, Hewett P.C., MacAlpine G.M., Turnshek D.A., Weymann R.J., Anderson S.F., 1987, AJ, 94, 1423
Fontana A., Ballester P., 1995, Messenger, 80, 37
Grevesse N., Sauval A.J., 1998, Space Sci. Rev., 85, 161
Haardt F., Madau P., 1996, ApJ, 461, 20
Haehnelt M.G., Steinmetz M., Rauch M., 1998, ApJ, 495, 647
Hazard C., Morton D.C., McMahon R.G., Sargent W.L.W., Terlevich R., 1986, MNRAS, 223, 87
Hewett P.C., Foltz C.B., Chaffee F.H., Francis P.J., Weymann R.J., Morris S.L., Anderson S.F., MacAlpine G.M., 1991, AJ, 101, 1121
Howk J.C., Sembach K.R., 1999, ApJ, 523, L141
Howk J.C., Savage B.D., Fabian D., 1999, ApJ, 525, 253
Izotov Y.I., Thuan T.X., 1999, ApJ, 511, 639
Izotov Y.I., Schaerer D., Charbonnel C., 2001, ApJ, 549, 878
Jimenez R., Bowen D.V., Matteucci F., 1999, ApJ, 514, L83
Kim T.-S., Cristiani S., D'Odorico S., 2001, A&A, 373, 757
Kim T.-S., Cristiani S., D'Odorico S., 2002, A&A, 383, 747
Lanzetta K.M., Wolfe A.M., Turnshek D.A., 1987, ApJ, 322, 739
Lanzetta K.M., McMahon R.G., Wolfe A.M., Turnshek D.A., Hazard, C, Lu L., 1991, ApJS, 77, 1
Ledoux C., Petitjean P., Bergeron J., Wampler J., Srianand R., 1998, A&A, 337, 51
Levshakov S.A., Dessauges-Zavadsky M., D'Odorico S., Molaro P., 2002, ApJ, 565, 696
Levshakov S.A., Agafonova I.I., D'Odorico S., Wolfe A.M., Dessauges-Zavadsky M., 2003, ApJ, 582, 596
Lopez S., Reimers D., Rauch M., Sargent W.L.W., Smette A., 1999, ApJ, 513, 598
Lopez S., Reimers D., D'Odorico S., Prochaska J.X., 2002, A&A, 385, 778
Lu L., Wolfe A.M., Turnshek D.A., Lanzetta K.M., 1993, ApJS, 84, 1
Lu L., Savage B.D., Tripp T.M., Meyer D.M., 1995, ApJ, 447, 597
Lu L., Sargent W.L.W., Womble D.S., Barlow T.A., 1996a, ApJ, 457, L1
Lu L., Sargent W.L.W., Barlow T.A., Churchill C.W., Vogt S.S., 1996b, ApJS, 107, 475
Madau P., Haardt F., Rees M.J., 1999, ApJ, 514, 648
Matteucci F., Molaro P., Vladilo G., 1997, A&A, 321, 45
Møller P., Jakobsen P., Perryman M.A.C., 1994, A&A, 287, 719
Nussbaumer H., Storey P.J., 1986, A&AS, 64, 545
Pei Y.C., Fall S.M., 1995, ApJ, 454, 69
Pei Y.C., Fall S.M., Hauser M.G., 1999, ApJ, 522, 604
Péroux C., Storrie-Lombardi L.J., McMahon R.G., Irwin M., Hook I.M., 2001, AJ, 121, 1799
Péroux C., Irwin M., McMahon R.G., Storrie-Lombardi L.J., 2002a, Fusco-Femiano R., Matteucci F., eds, ASP Conf. Proc. 253, Chemical Enrichment of Intracluster and Intergalactic Medium. Astron. Soc. Pac, San Francisco, p. 501
Péroux C., Petitjean P., Aracil B., Srianand R., 2002b, New Astron., 7, 577
Péroux C., McMahon R.G., Storrie-Lombardi L.J., Irwin M., 2003a, MNRAS, submitted (astro-ph/0107045)
Péroux C., Dessauges-Zavadsky M., D'Odorico S., Kim T.-S., McMahon R.G., 2003b, MNRAS, 345, 480, (Paper II)
Petitjean P., Rauch M., Carswell R.F., 1994, A&A, 291, 29
Petitjean P., Srianand R., Ledoux C., 2000, A&A, 364, L26
Pettini M., Smith L.J., Hunstead R.W., King D.L., 1994, ApJ, 426, 79
Pettini M., Ellison S.L., Steidel C.C., Bowen D.V., 1999, ApJ, 510, 576
Pettini M., Ellison S.L., Bergeron J., Petitjean P., 2002, A&A, 391, 21
Prochaska J.X., Wolfe A.M., 1996, ApJ, 470, 403
Prochaska J.X., Wolfe A.M., 1997, ApJ, 474, 140
Prochaska J.X., Wolfe A.M., 1998, ApJ, 507, 113
Prochaska J.X., Wolfe A.M., 1999, ApJS, 121, 369
Prochaska J.X., Wolfe A.M., 2000, ApJ, 533, L5
Prochaska J.X., Wolfe A.M., 2002, ApJ, 566, 68
Prochaska J.X., Gawiser E., Wolfe A.M., 2001a, ApJ, 552, 99
Prochaska J.X., Wolfe A.M., Tytler D., Burles S.M., Cooke J., Gawiser E., Kirkman D., O'Meara J.M., Storrie-Lombardi L.J., 2001b, ApJS, 137, 21
Prochaska J.X., Howk J.C., O'Meara J.M., Tytler D., Wolfe A.M., Kirkman D., Lubin D., Suzuki N., 2002, ApJ, 571, 693
Sargent W.L.W., Steidel C.C., Boksenberg A., 1988, ApJS, 68, 539
Savaglio S., 2000, IAUS, 204, 24
Songaila A, Cowie L.L., 2002, AJ, 123, 2183
Storrie-Lombardi L.J., Wolfe A.M., 2000, ApJ, 543, 552
Storrie-Lombardi L.J., Irwin M.J., McMahon R.G., Hook I.M., 2001, MNRAS, 322, 933
Viegas S.M., 1995, MNRAS, 276, 268
Vladilo G., Bonifacio P., Centurión M., Molaro P., 2000, ApJ, 543, 24
Vladilo G., Centurión M., Bonifacio P., Howk J.C., 2001, ApJ, 557, 1007
Wampler E.J., Bergeron J., Petitjean P., 1993, A&A, 273, 15
Warren S.J., Hewett P.C., Osmer P.S., 1991, ApJS, 76, 23
Warren S.J., Møller P., Fall S.M., Jakobsen P., 2001, MNRAS, 326, 759
Wolfe A.M., Turnshek D.A., Smith H.E., Cohen R.D., 1986, ApJS, 61, 249
Wolfe A.M., Lanzetta K.M., Foltz C.B., Chaffee F.H., 1995, ApJ, 454, 698

This paper has been typeset from a TEX/LATEX file prepared by the author.